TU Delft

Delft University of Technology

Solid phase crystallisation of hydrogenated amorphous silicon deposited by ETPCVD on glass

Westra, Joke

DOI
10.4233/uuid:6b40384c-c139-4b7a-8080-fe883aa95628

Publication date
2018

Document Version
Final published version

Citation (APA)
Westra, J. (2018). *Solid phase crystallisation of hydrogenated amorphous silicon deposited by ETPCVD on glass*. [Dissertation (TU Delft), Delft University of Technology]. https://doi.org/10.4233/uuid:6b40384c-c139-4b7a-8080-fe883aa95628

Important note
To cite this publication, please use the final published version (if applicable).
Please check the document version above.

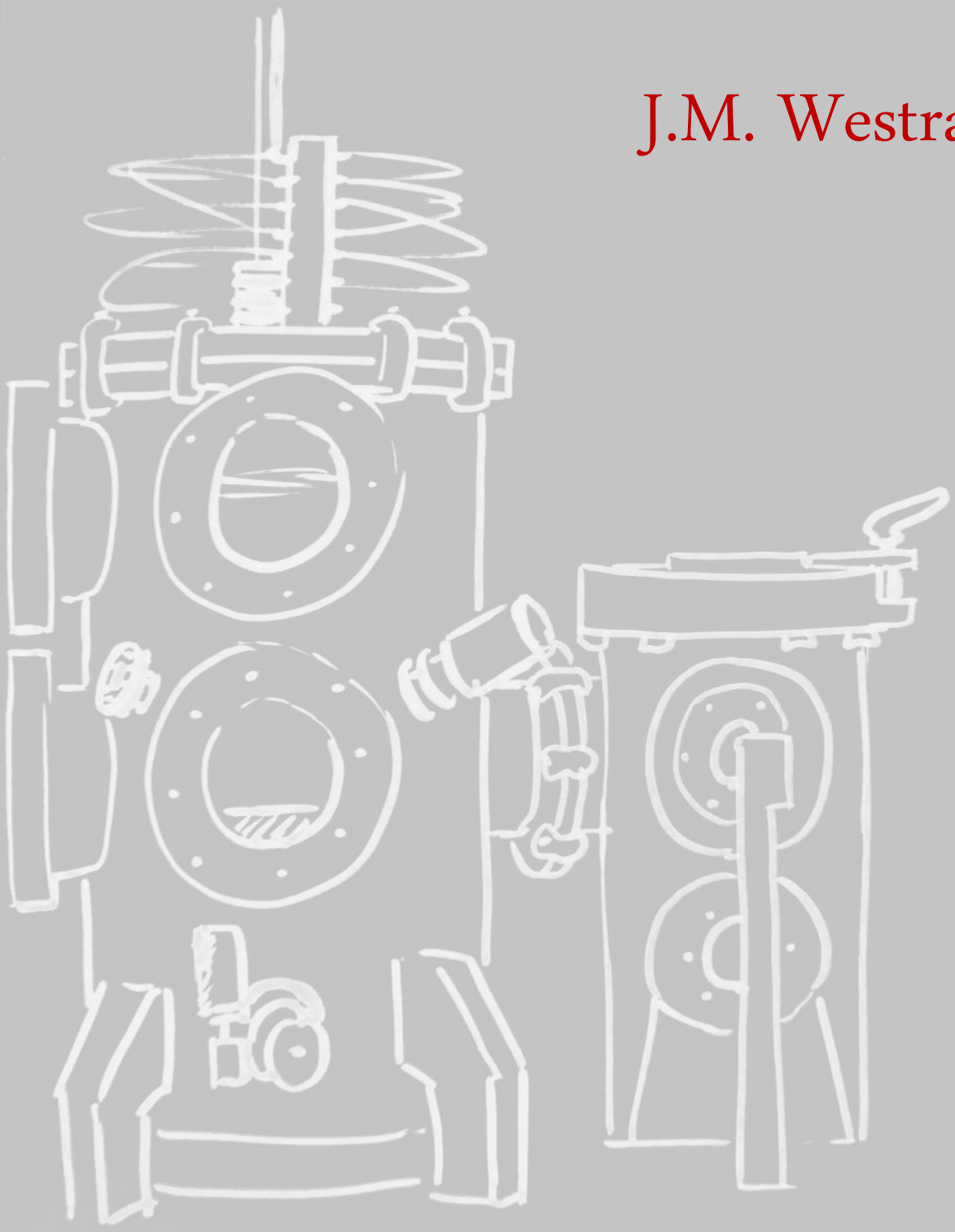
Copyright
Other than for strictly personal use, it is not permitted to download, forward or distribute the text or part of it, without the consent of the author(s) and/or copyright holder(s), unless the work is under an open content license such as Creative Commons.

Takedown policy
Please contact us and provide details if you believe this document breaches copyrights.
We will remove access to the work immediately and investigate your claim.

This work is downloaded from Delft University of Technology.
For technical reasons the number of authors shown on this cover page is limited to a maximum of 10.

SOLID PHASE CRYSTALLISATION OF HYDROGENATED AMORPHOUS SILICON DEPOSITED BY ETPCVD ON GLASS

J.M. Westra



SOLID PHASE CRYSTALLISATION OF HYDROGENATED AMORPHOUS SILICON DEPOSITED BY ETPCVD ON GLASS

Proefschrift

ter verkrijging van de graad van doctor
aan de Technische Universiteit Delft,
op gezag van de Rector Magnificus
Prof. dr. ir. T. H. J. J. van der Hagen,
voorzitter van het College van Promoties,
in het openbaar te verdedigen
op dinsdag 18 december 2018 om 10 uur
door

Joke Margriet WESTRA

Master of Science in Materials Science & Engineering,
Technische Universiteit Delft, Nederland
geboren te Hoorn, Nederland

Dit proefschrift is goedgekeurd door de promotoren.

Samenstelling promotiecommissie bestaat uit:

Rector Magnificus	voorzitter
Prof.dr. M. Zeman	Technische Universiteit Delft, promotor
Dr. R.A.C.M.M. van Swaaij	Technische Universiteit Delft, copromotor

Onafhankelijke leden:

Prof.dr. R. Ross	Technische Universiteit Delft
Prof.dr.ir. S. van der Zwaag	Technische Universiteit Delft
Prof.dr. R. Schlatmann	Helmholtz Zentrum Berlin, Duitsland
Dr. A. J. Böttger	Technische Universiteit Delft
Dr. S. W. H. Eijt	Technische Universiteit Delft

ISBN: 978-94-028-1321-0

Acknowledgements:

This research was financially supported by the Dutch agency Senter-Novem under EOS-LT program (project number: EOSLT06028).

Contents

Samenvatting **vii**

Summary **xi**

1 Introduction **1**

1.1 Silicon for solar cells 3

1.1.1 Mono- and multi-crystalline silicon 3

1.1.2 Polycrystalline silicon 5

1.1.3 Amorphous silicon 6

1.2 Thermodynamics and kinetics of crystallisation 8

1.2.1 Thermodynamics of phase-transformation 8

1.2.2 Nucleation 11

1.3 Solid phase crystallisation for silicon solar cells 13

1.4 Scope and outline of this dissertation 14

1.5 Contribution to the field 16

2 Experimental procedures and details **19**

2.1 Deposition of a-Si:H 19

2.1.1 Plasma Enhanced Chemical Vapour Deposition . 19

2.1.2 Expanding Thermal Plasma CVD 21
2.2 Structural film characterisation 22
2.2.1 Fourier Transform Infrared Spectroscopy 22
2.2.2 Raman Spectroscopy 25
2.2.3 X-ray diffraction 27
2.3 Opto-electrical film characterisation 32
2.3.1 Optical transmission and reflection 32
2.3.2 Dark IV and activation energy 34
2.3.3 Hall effect 35

3 Comparison of FTIR and RS for the characterisation of a-Si:H 39

3.1 Introduction 39
3.2 Experimental 41
3.3 Results of a-Si:H characterisation 44
3.3.1 Si-H modes detected by RS and FTIR 44
3.3.2 Positions of Raman shift and absorption frequencies of Si-H_x related features 49
3.4 Discussion on characterization of a-Si:H 51
3.5 Conclusions 54

4 Deposition of B doped a-Si(:H) films by ETPCVD 55

4.1 Introduction 55
4.2 Experimental details 56
4.2.1 Deposition techniques 56
4.2.2 Sample preparation and characterisation techniques 57
4.3 Results 60

4.4 Discussion 65
4.5 Conclusion 69

5 Formation of poly-Si on glass observed by in-situ XRD 71
5.1 Introduction 71
5.2 Experimental details 72
5.3 Results 75
5.4 Discussion 79
5.5 Conclusion 82

6 Influence of B doping and *R on the crystallisation of a-Si:H 83**
6.1 Introduction to Solid Phase Crystallisation of doped a-Si:H 84
6.2 Experimental details 85
6.3 Results 88
6.4 Discussion 91
6.5 Conclusion 97

7 Conclusions 99

Bibliography 117

Acknowledgements 119

About the author 123

Publications 125

Samenvatting

De opwekking van elektriciteit met behulp van duurzame energiebronnen begint een integraal onderdeel van de elektrische energie mix te worden. Het wordt voorzien dat een aanzienlijk deel van deze elektrische energie geleverd zal worden door fotovoltaische (Eng: Photovoltaic; PV) zonnecellen die licht direct omzetten in elektriciteit. Om fotovoltaïsche energie op grote schaal praktisch en esthetisch in onze maatschappij te integreren, zal het een onderdeel moeten worden van onze gebouwen. Voor het implementeren van PV op grote schaal heeft het gebruik van non-toxische en niet-schaarse materialen en productietechnieken de voorkeur [1]. Door deze eigenschappen geniet silicium de voorkeur voor gebruik in zonnecellen, ook al zijn voor de zuivering en dotering toxische materialen nodig [2].

Dit proefschrift is onderdeel van een onderzoek naar het ontwikkelen van zonnecellen gebaseerd op dunne lagen van kristallijn silicium die worden verkregen door het kristalleren van dunne lagen van amorf silicium. Deze lagen van kristallijn silicium moeten een dikte hebben van ongeveer 10 μm om voldoende licht door de zonnecel te laten absorberen [3]. Deze dikte vraagt om hoge groeisnelheden bij het vormen van de lagen. De siliciumlagen die in dit proefschrift gepresenteerd worden, zijn in eerste instantie amorf van structuur en bevatten waterstof (a-Si:H). De lagen zijn gegroeid door middel van

twee technieken: *Expanding Thermal Plasma Chemical Vapour Deposition* (ETPCVD) en *Plasma Enhanced Chemical Vapour Deposition* (PECVD).

Het is belangrijk om de atomaire configuratie van a-Si:H te kennen bij het bestuderen van het kristallisatie proces. Deze kan namelijk van grote invloed zijn op dit proces. Voor het kristalliseren is het herpositioneren van de Si atomen noodzakelijk. Ook zullen waterstofatomen uit de laag moeten diffunderen omdat de oplosbaarheid van waterstof in de kristalstructuur veel lager is dan in de amorfe structuur [4]. Daarom is kennis van de 'amorfe' structuur van de lagen, voorafgaand aan de kristallisatie, essentieel. De microstructuur en de waterstofconfiguratie van de gegroeide lagen zijn bestudeerd met Raman Spectroscopie (RS). *Fourier Transform Infrared* (FTIR) spectroscopie wordt veelvuldig toegepast om de Si-H_x *wagging*- en *stretching*-modes te meten en daarmee de microstructuurparameter R^* te bepalen. Deze *stretching* modes zijn ook meetbaar met RS. In tegenstelling tot FTIR, is het mogelijk om substraatonafhankelijke metingen te maken met RS. In Hoofdstuk 3 van dit proefschrift worden de metingen van waterstof en de waterstofconfiguraties door RS vergeleken met die door FTIR. Door de verschillen in *collection depth* van de RS-signalen is het nauwkeurig bepalen van de c_{H} niet mogelijk voor deze lagen. Het golfgetal van de *wagging mode* is goed te bepalen met de RS-metingen met de groene laser, maar minder goed met de rode laser. De Si-H_x gerelateerde kenmerken in de RS spectra kunnen gebruikt worden om de piekposities van de *low stretching mode* (ω_{LSM}), de *high stretching mode* (ω_{HSM}) en de microstructuurparameter R^* te bepalen. De gevoeligheid voor de *low stretching mode* en *high stretching mode* verschilt tussen FTIR en RS, daarom moeten de R^* en ω geschaald worden wanneer metingen met elkaar vergeleken worden.

Voordat de silicium kristallaag in zonnecellen toegepast kan worden, moet deze gedoteerd worden. Dit kan na de kristallisatie van de laag, maar de doteringselementen kunnen ook meegegroeid worden met de laag. Het voordeel van het meegroeien van het doteringselement is dat er een processstap minder nodig is. Doteringselementen kunnen

de kristallisatie van de a-Si:H lagen beïnvloeden [5]. Daarom zijn zowel intrinsieke als borium gedoteerde lagen tijdens het kristalliseren bestudeerd met in-situ röntgendiffractie.

De eerste borium gedoteerde a-Si:H lagen gegroeid door middel van ETPCVD worden gepresenteerd in Hoofdstuk 4. De lagen zijn vergeleken met a-Si:H lagen gegroeid met PECVD. De B-gedoteerde ETPCVD-gegroeide a-Si:H lagen hebben een B-gehalte van ongeveer 8.5×10^{15} cm^{-2} bij een gasverhouding van B_2H_6-op-SiH_4 van 8×10^{-4} en een groeitemperatuur van 325 °C. Dit gehalte is vergelijkbaar met lagen die met PECVD gegroeid zijn bij vergelijkbare gasverhouding en temperatuur. Het B-gehalte neemt toe bij het verhogen van de B_2H_6-op-SiH_4 verhouding bij beide technieken. Voor ETPCVD gegroeide lagen is het B-gehalte onafhankelijk van de groeitemperatuur, maar bij PECVD gegroeide lagen neemt het B-gehalte toe wanneer de groeitemperatuur afneemt. Na kristallisatie van de lagen is het doteringsrendement ongeveer 40%. Voor a-Si:H lagen gegroeid met ETPCVD bij een temperatuur van 350 °C is de bandgap, E_g, zowel afhankelijk van het B-gehalte als van het H-gehalte en de configuratie (R^*). Hoewel er aanvullend onderzoek naar de invloed van het H-gehalte noodzakelijk is, is de invloed ervan op het kristallisatie proces aangetoond door middel van de microstructuurparameter R^*.

In de hoofstukken 5 en 6 staan de resultaten van de in-situ röntgendiffractie metingen van de kristallisatie van ETPCVD gegroeide a-Si:H-lagen. Verwarmen naar 500 °C leidt niet tot kristallisatie. Lagen verwarmd naar 600 °C gedurende twee uur bevatten nog a-Si:H materiaal. Het waterstofgehalte en de atomaire configuratie in de lagen beïnvloedt aantoonbaar het kristalliseren; een toename in R^* reduceert de kristallisatiesnelheid. Het blijkt dat lagen binnen een half uur kristalliseren bij temperaturen van 650 °C en hoger. In RS metingen van deze lagen zijn geen a-Si:H kenmerken gedetecteerd.

Zowel de R^* als het B-gehalte beïnvloeden de vaste stof kristallisatie (Eng: *solid phase crystallisation*) van a-Si:H. In Hoofd-

stuk 6 wordt aangetoond dat de B-dotering de tijd waarna kristallisatie waarneembaar is (de zogenaamde initiatietijd) reduceert. Daarnaast laten de resultaten in dit hoofdstuk zien dat ook de tijd tot volledige kristallisatie (de kristallisatietijd) korter wordt. Na analyse van de röntgendiffractieresultaten concluderen we dat B de groeisnelheid van de kristallen bevordert, maar dat het effect op de nucleatie van kristallen beperkt is. De mate waarin B-dotering de groeisnelheid van de kristallen bevordert wordt bepaald door de gasverhouding B_2H_6-op-SiH_4. Dit geldt zowel voor de ETPCVD als de PECVD gegroeide lagen. Bij de intrinsieke PECVD en ETPCVD lagen wordt een toename in initiatietijd tot kristallisatie geobserveerd bij een toename in R^* [6]. De invloed van R^* op de kristallisatie is geobserveerd voor B-gedoteerde a-Si:H lagen gegroeid met zowel ETPCVD als PECVD.

Summary

Generation of electricity using renewable energy sources is becoming an integral part of the electrical energy mix. A substantial fraction of the electrical energy is foreseen to be generated by photovoltaic (PV) solar cells that directly convert light into electricity. Large scale application of building integrated PV is envisaged to aid the integration of renewable energy in our society, both from a practical and an aesthetic point of view. For implementation of large-scale PV preferably abundant and non-toxic materials are required as well as production processes for making the solar cells in large quantities [1]. For this purpose silicon is the most preferred element, because of its properties for application in solar cells and because of its abundance, despite the fact that refining and doping of Si are dependant on toxic materials [2].

This dissertation is part of a study into the development of thin film crystalline silicon solar cells. Such solar cells require a thickness of the crystalline silicon layer of approximately 10 μm to ensure sufficient light absorption [3]. The deposition of films with such a thickness requires high deposition rates. For the work presented in this thesis hydrogenated amorphous silicon (a-Si:H) films have been deposited by Expanding Thermal Plasma Chemical Vapour Deposition (ETPCVD),

with which high deposition rates have been demonstrated, and Plasma Enhanced Chemical Vapour Deposition (PECVD).

In order to study the crystallisation of a-Si:H it is important to know about the atomic configuration of the material as this can strongly influence the crystallisation process. In the case of crystallisation of a-Si:H, not only a reconfiguration of the Si atoms is needed. The solubility of hydrogen atoms in c-Si is much lower than in a-Si:H [4] and for this reason hydrogen atoms must diffuse out of the film during annealing. Therefore information on the structure of the amorphous films prior to crystallisation is essential. In this thesis the silicon microstructure and the hydrogen bonding configuration of as-deposited films are studied using Raman Spectroscopy (RS). Fourier Transform Infrared (FTIR) spectroscopy is frequently used to detect the Si-H_x wagging and stretching modes to determine the microstructure parameter R^* of a-Si:H films. These stretching modes can also be detected by RS. In contrast to FTIR, RS can make substrate independent measurements. In Chapter 3 of this dissertation the detection of hydrogen and hydrogen bonding configurations by RS is compared to the detection by FTIR. The RS measurements of the Si-H_x related features can be used to evaluate the peak positions of the low stretching mode (ω_{LSM}), and high stretching mode (ω_{HSM}), as well as the microstructure parameter R^*. The sensitivity to the low and high stretching modes is not the same for the FTIR and RS measurements and therefore the R^* and ω need to be scaled for comparison.

For thin film polycrystalline Si to be used for solar cell applications, they must be doped. This can be achieved by doping after crystallisation, but also by crystallising films which already contain the dopant atoms. The main benefit of in-situ doping of the a-Si:H film during deposition is a reduction in processing steps. As dopants can influence the crystallisation process for a-Si films [5], the crystallisation of intrinsic and boron-doped films is studied by in-situ x-ray diffraction during the crystallisation process.

The first boron doped a-Si:H films deposited by ETPCVD are presented in this work in Chapter 4. The films are compared to B-doped a-Si:H films deposited by PECVD. The B-doped ETPCVD deposited a-Si:H films have a B content of approximately 8.5×10^{15} cm^{-2} for a B_2H_6-to-SiH_4 gas-flow ratio of 8×10^{-4} deposited at 325 °C. This B content is similar to films deposited by PECVD with a similar B_2H_6-to-SiH_4 ratio and deposition temperature. The B content increases with increasing B_2H_6-to-SiH_4 ratio for both deposition techniques. The B content is independent of the deposition temperature for ETPCVD films but increases with decreasing deposition temperature for PECVD films. Crystallisation of the films leads to a doping efficiency of approximately 40%. For the a-Si:H ETPCVD films deposited at 350 °C it is shown that the E_g depends both on the B concentration as well as the H content and configuration (R^*). Although additional research into the influence of the H content is required, the influence is evident from the microstructure parameter R^*.

In Chapters 5 and 6 the crystallisaton of ETPCVD a-Si:H is studied by using in-situ x-ray diffraction (XRD). We observed that after annealing at temperatures of 650 °C and higher the crystallinity saturates within half an hour. In these films no a-Si:H contribution is detected by RS. Annealing at 500 °C does not induce any crystallization at all. Films annealed at 600 °C for two hours still contain an a-Si:H fraction. The hydrogen content and bonding configuration in the films are shown to influence the crystallization process, specifically an increase in R^* decreases the crystallisation rate.

Both the R^* and the B concentration influence the solid phase crystallisation of a-Si:H. In Chapter 6 we show that B doping reduces the onset of crystallization of a-Si:H and the crystallization time. From the analysis of the XRD results we conclude that B enhances the grain growth rate of the B-doped a-Si:H films, but that the effect of B on the nucleation rate is limited. The extent of the enhanced grain growth rate due to B doping is controlled by the B_2H_6-to-SiH_4 gas-flow ratio, for both PECVD deposited films and ETPCVD deposited films. For both intrinsic PECVD and ETPCVD samples increasing R^* increases

the onset time to crystallization [6]. The influence of R^* is also present in the crystallisation process of the B-doped a-Si:H films deposited by ETPCVD and PECVD.

Chapter 1

Introduction

On 22 April 2017 the UK National Grid reported that Britain did not use coal to generate electricity for a full day. This was the first time since the 1880s, the start of the Industrial Revolution, that this has occurred [7]. On 30 April 2017 66% of consumed electricity in Germany was produced by renewables only [8]. These reports are examples of the metamorphoses that energy production has undergone in the past twenty years and is undergoing today. The combined energy production by hydroelectricity plants, wind turbines, and photovoltaic (PV) solar cells (devices that directly convert light into electricity) has increased from approximately 29.0 million tonnes of oil equivalent (MTOE) ($\sim$ 1212.9 PJ) in 1996 to 64.1 MTOE ($\sim$ 2683.0 PJ) [9] in 2015, as shown in figure 1.1. This indicates that the utilisation of renewable energy is no longer an academic discussion. Electricity harvested using the above-mentioned renewable energy sources has become an integral part of electrical energy mix. Sustainable electrical energy generation, transport, and balancing are immediate concerns of the energy markets, legislation offices, home owners, and the operators of electricity distribution and transmission grids as it strongly influences energy prices and alters the energy distribution paths. From

a balance perspective urban generation of electricity from sunlight is particularly interesting as the electrical energy consumption profiles of office buildings match the electricity production of solar cells during a day rather well [10]. This issue is a challenge for the distribution grid operators as the grid was not designed for energy transport in lateral directions.

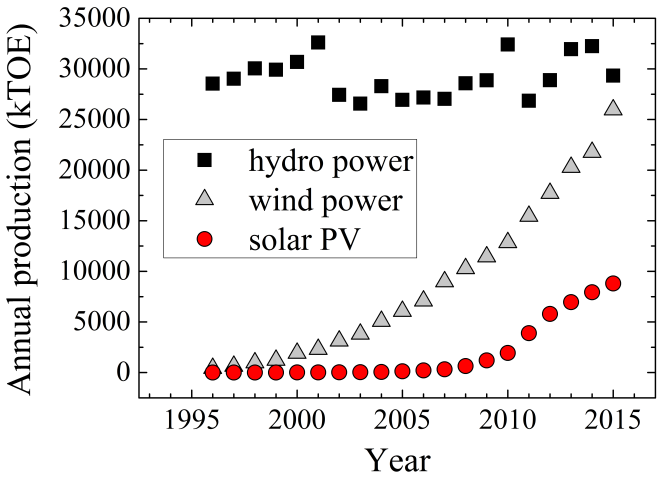


Figure 1.1. Annual electricity production in thousand tonnes of oil equivalent (kTOE) in the European Union (28 countries) since 1996, according to Eurostat [9].

Urban applications of PV modules fuel the research efforts into building integrated PV. PV modules can replace conventional building materials in parts of a building's outer shell such as the roof covering or façades [11, 12]. Technology based on thin-film solar cells has been of particular interest for solar cell glazing products. In PV industry the term 'thin film' is often used to simple distinguish between cells with absorber layers thinner than approximately 20 μm with traditional wafer based technologies having a thickness well in excess of 100 μm. Thin film PV technology allows for light weight, flexible and even semitransparent solar panels, allowing more freedom of form. Solar

cells can be integrated in fenestration products (e.g. windows), façades, or roofs and provide various aesthetic options for building envelopes [13]. Application of PV technology in building materials could be a strong aid in the acceptance of this technology in our society, both from a practical and an aesthetic point of view. Large scale application of PV technology does require a reasonable abundance of, preferably, non-toxic materials for the implementation [1]. Silicon is the most preferred element for usage as PV absorber layer, because of its suitable properties for application in solar cells and abundance, despite the fact that refining and doping of this material are dependant on toxic materials [2].

1.1 Silicon for solar cells

On 25 April 1954 Bell Labs demonstrated the first practical silicon solar cell, made by Chapin, Fuller and Pearson [14, 15]. This design was subsequently improved and exceeded the 10% efficiency mark within 18 months. Since that time the efficiency of solar cells based on crystalline silicon (c-Si) has steadily increased to the level of 26.6% demonstrated by Kaneka Corporation [16]. These research efforts have resulted in a large Si-based PV industry. In fact, the majority of PV panels installed in the world are modules based on c-Si wafers [17]. The Si solar cell technologies can be categorised by the material used for the absorbed and/or by the device design. For silicon the absorber categories are single crystalline, multi-crystalline, thin-film crystalline and thin-film amorphous [18]. These categories are based on the atomic structure of the silicon used in the PV cells and the thickness of the absorber layer. These forms of silicon are explained in this section.

1.1.1 Mono- and multi-crystalline silicon

In crystalline silicon the atoms are arranged in a regular lattice; all silicon atoms are bonded to four neighbouring atoms in a diamond cubic lattice (see figure 1.2) with fixed bond length of 5.43 Å and angle

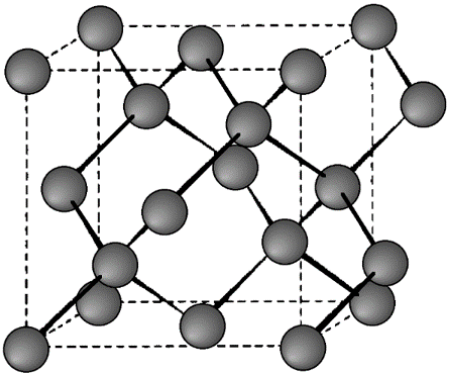


Figure 1.2. Diamond cubic crystal structure, the unit cell is indicated by the dashed cube [19].

of 109 °. The atomic structure of crystalline silicon is diamond cubic (see figure 1.2). For solar-cell application the crystalline silicon is cut into wafers. Mono-crystalline silicon wafers consist of a single crystal. Multi-crystalline silicon wafers consist of more than one crystal. These crystals have dimensions in the order of 1 mm to 10 cm [20], which exceeds the wafer thickness, thus appearing to be a single crystal. Mono-crystalline solar cells, also referred to as single crystalline solar cells, are based on Si wafers, typically cut from a single crystal ingot and often grown using the Czochralski process. Multi-crystalline cells use wafers cut from cast Si.

Crystalline Si is a PV material: the absorption of photons by Si can result in the excitation of electrons, creating electron-hole pairs. This process is known as the photovoltaic effect. PV device structures, based on one or more pn-junctions, allow for the separation and collection of the charge carriers. In PV devices, PV material is used as the absorption layer. The thickness of this layer is a compromise between the absorption of light and the effective collection of the charge carriers. In 70 μm of monocrystalline silicon 90% of the light spectrum between 280 and 1100 nm is absorbed [21, 22]. Not all energy absorbed by the solar cell will be delivered to the external circuit, as part of the energy is lost. Two main energy loss mechanisms are non-absorption and ther-

malisation. Light with a wavelength beyond 1127 nm is not absorbed, as the energy of these photons is insufficient to create an electron-hole pair in crystalline Si (bandgap of 1.1 eV). Thermalisation occurs when photons with energies higher than the bandgap are absorbed. The excess energy of the excited electron is lost in interactions with the silicon lattice, leading to a higher temperature. Another energy loss mechanism for silicon-based solar cells is the recombination of electrons and holes. For single crystal Si solar cells the diffusion length of the minority carriers is typically 100-300 μm [23, 24]. The main difference between single and multi-crystalline Si is the presence of grain boundaries (in the multi-crystalline Si), which can act as recombination sites for the charge carriers, this decreases the carrier lifetime and thus the diffusion length.

1.1.2 Polycrystalline silicon

Polycrystalline silicon (poly-Si) consist of multiple crystals with typical grain size of < 1 mm. In literature, multicrystalline silicon is sometimes considered as a type of poly-Si, with crystalline grains typically as large or larger than the thickness of a wafer. For this reason multicrystalline silicon is often compared to mono-crystalline silicon, but taking into account the effect of grain boundaries.

Thin poly-Si films can be made in several ways. Thin films can be sliced from Si cast ingot, or cast as ribbons. A different production method is epitaxial growth of poly-Si (from vapour or solid a-Si(:H)) on a crystalline substrate, such as a monocrystalline silicon wafer. After the film is grown it can be separated from the wafer. Another method is crystallising a-Si(:H) films. This can be done by methods such as laser induced crystallisation (LIC) [25], solid phase crystallisation (SPC), and rapid thermal annealing (RTA). In the latter method crystallisation is induced at temperatures above 700 °C, using lamps as heat source [26]. SPC uses temperatures around 600 °C and it can take up to 20 hours of furnace annealing before the film is completely crystallized [27]. Using SPC, metals such as aluminium can be included to lower the crystallisa-

tion temperature and time. This is metal induced crystallisation (MIC) [28].

As mentioned previously grain boundaries can act as recombination sites. As poly-Si has small grains, grain boundaries present one of the most important challenges for the application of poly-Si in solar cells. Investigation over the past five decades has led to a detailed understanding of the precise influence of various kinds of grain boundaries on the electronic properties of crystalline silicon. In general the crystallographic orientation of neighbouring grains determines the local properties. Grain boundaries with a strong lattice mismatch cause electron-hole pair recombination, while grain boundaries with matching lattices, such as twin boundaries, have a much smaller influence. In addition crystallographic defects, such as lattice distortions within a grain, can also act as recombination centres [29]. Ideally PV material is free from grain boundaries and inter-grain crystallographic defects.

1.1.3 Amorphous silicon

As discussed in Section 1.1.1, atoms in crystalline silicon are arranged in a regular lattice. In amorphous silicon the interatomic distance and in particular the bond angles show variations, leading to some degree of disorder of the atomic lattice. Also so-called 'dangling bonds' occur, where one of the Si bonding electrons is not bonded to a neighbouring atom. Amorphous silicon [30, 31] typically contains a defect density of 10^{19} to 10^{21} cm^{-3}. Incorporation of hydrogen can reduce the large densities of electronically active dangling-bond defects from 10^{19} cm^{-3} in pure a-Si to 10^{15} cm^{-3} in a-Si:H [32]. Mostly the influence of hydrogen in reducing the defect density is explained by assuming that atomic hydrogen forms a bond to replace the missing neighbouring atom this defect [33].

Research by Smets [34], Roca [35] and Schropp [36] shows that a-Si(:H) material can be produced through a wide range of methods and exhibiting different atomic structures. Currently two models

or model groups are used to describe the structure of a-Si:H: the continuous random network (CRN), and the anisotropic disordered network (ADN). The CRN models are the most simple: they are based on a random distribution of the Si-Si and Si-H bonds in the a-Si:H network. Street [33] uses the covalent bond based CRN model to explain a-Si:H properties such as doping and defect passivation. In contrast to models based on CRN, ADN models for a-Si:H include anisotropic features such as nanovoids and specific mono- and dihydride (MH and DH) configurations [37]. Smets et al. [38] proposed an ADN model based on divacancy configurations within the Si-Si network.

A-Si:H can be made by chemical vapour deposition (CVD), commonly using silane (SiH_4) as the precursor gas. Hydrogen is incorporated during the deposition process. The most common deposition method in research and industry is Plasma Enhanced CVD (PECVD), which will be discussed in more detail in section 2.1.1. In the deposition process hydrogen is of great influence as has been shown by Kessels et al. [39]. The growth conditions of the film determine the material structure and the hydrogen concentration in the film. Hydrogen is also included in a variety of models describing the growth of a-Si:H for multiple deposition techniques. Hydrogen is important in both the thermodynamic approach [40, 41, 42], and in kinetic growth models which include surface processes [43, 44]. The focus of this thesis is the formation of thin film poly-Si on glass by solid phase crystallisation of a-Si:H. As the absorption of crystalline Si is much lower than of a-Si:H, solar cell applications require thicker films to ensure sufficient light can be absorbed. The production of such films requires high deposition rates. Expanding Thermal Plasma CVD (ETPCVD) allows for a-Si:H deposition with growth rates up to 10 nm/s [39], as will be discussed in section 2.1.2. The a-Si:H films discussed in this thesis are made ETPCVD, or by PECVD for comparison.

1.2 Thermodynamics and kinetics of crystallisation

In order to understand the transformation of a-Si and a-Si:H to a polycrystalline material, several concepts about thermodynamics and kinetics are discussed in this section. First, the classical description of the thermodynamics of solid phase transformation will be given. Next the difference between homogeneous and heterogeneous nucleation will be explained and related to nucleation in a-Si(:H).

1.2.1 Thermodynamics of phase-transformation

Phase transformation occurs because the initial phase of the material is unstable relative to the final state [45]. This stability of the material is quantified by the Gibbs free energy (G) of a system, as is defined by equation:

$$G = H - TS \tag{1.1}$$

where H is the enthalpy, T the absolute temperature and S the entropy of the system [45]. The enthalpy is a measure of the heat content of the system and is given by the classic thermodynamics equation:

$$H = E + PV \tag{1.2}$$

where P is the pressure, V is the volume and E is the internal energy of the system. The internal energy can be divided into potential and kinetic energy of the atoms which make up the system [45].

In mathematical terms an equilibrium can be described by:

$$\mathrm{d}G = 0 \tag{1.3}$$

According to the definition in Ref. [45] a system is said to be in (stable) equilibrium when it is in the most stable state, i.e. it shows no desire to change ad infinitum. Other configurations than the most stable one are often possible and typically associated with their own local minimum in free energy. A local minimum is called a metastable equilibrium. Figure 1.3 shows a variation of the Gibbs free energy in which configuration 'A' has the lowest free energy and therefore is a stable equilibrium and configuration 'B' is a metastable equilibrium. A criterion for any phase transformation is

$$\Delta G = G_A - G_B < 0 \tag{1.4}$$

where G_B and G_A are the initial and final state, respectively.

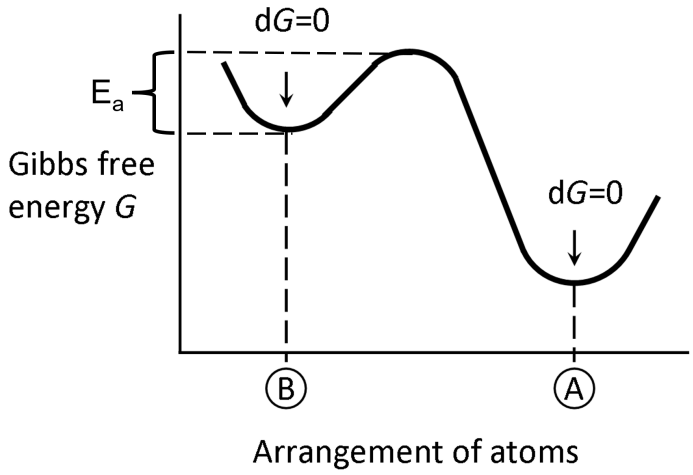


Figure 1.3. Gibbs free energy for two arrangements of atoms. Configuration 'A' has the lowest free energy, making this arrangement the stable equilibrium. Configuration 'B' is a metastable equilibrium. [45]

In this representation, the B state concurs with the a-Si:H phase. A transformation does not need to go directly to the stable equilibrium state but can pass through a whole series of intermediate metastable

states. Figure 1.4 shows the relative free energy of amorphous to crystalline Si described by Spinella et al. [5]. The relation between the difference in free energy of unrelaxed a-Si and diamond cubic crystalline Si, indicates another metastable phase: relaxed a-Si. Many different a-Si:H and a-Si materials have been reported. The state of the a-Si(:H) material is dependent on the deposition technique and deposition conditions. For a transformation from configuration B to A to occur, the activation energy of transition between configurations has to be overcome. The concept of solid phase crystallisation is that the material does not have to take liquid form to allow the atoms to reconfigure to a crystalline phase. Figure 1.4 shows that there is a free energy difference between a-Si and crystalline Si which might drive a phase transition, if the material kinetics allow it. Olson and Roth [46] and Spinella et al. [5] investigated the solid phase crystallisation of a-Si and found that at temperatures of around 600 °C the Si atoms have sufficient mobility for this phase transition, both for grain growth and nucleation.

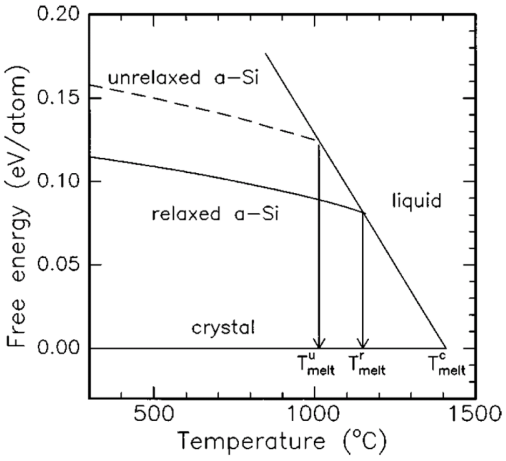


Figure 1.4. Free energy difference of relaxed and unrelaxed a-Si with respect to crystalline Si [5].

1.2.2 Nucleation

The initiation of a phase change, such as the formation of a solid crystal typically from a liquid in a small region, is called nucleation. In this work *nucleation* will refer specifically to the formation of Si crystals from a-Si(:H) material. Nucleation is initiated by rapid local fluctuations on a molecular scale in the metastable state, a-Si(:H). There are two ways nucleation occurs: homogeneous and heterogeneous nucleation. Homogeneous nucleation is not influenced in any way by pre-existing solids or surfaces. When a foreign substrate or foreign particles are involved, one speaks of heterogeneous nucleation.

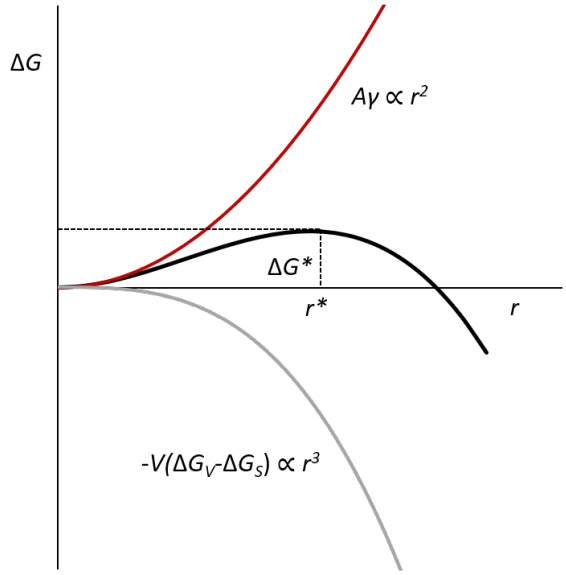


Figure 1.5. Free energy change associated with homogeneous nucleation of a sphere of radius r, where V is the volume, G_{v} is the free energy and G_{s} misfit strain energy both per unit volume, A is the interface area, γ is the interfacial energy per unit area. [45]

Homogeneous nucleation

In classical thermodynamics homogeneous nucleation in solids is associated with the free energy change of three contributions:

- The creation of a volume (V) of the stable phase (c-Si) will cause an energy *reduction* of $V \times G_{\mathrm{v}}$, where G_{v} is the free energy per unit volume.
- The creation of an interface area (A) will give a free energy *increase* of $A\gamma$, where γ is the interfacial energy per unit area, assuming that the interface between the parent and child phase is isotropic.
- As stated in Ref. [45] the transformed volume will in general not fit perfectly into the space that was originally occupied by the solid parent phase. This gives rise to a misfit strain energy ΔG_{s}, per unit of volume. The resulting positive term of free energy ΔG_{s} is proportional to the volume of the inclusion (V).

The total change in the Gibbs free energy, ΔG, is the sum of the three contributions discussed above and becomes:

$$\Delta G = -V\Delta G_{\mathrm{V}} + A\gamma + V\Delta G_{\mathrm{s}} \tag{1.5}$$

In this equation the second term $A\gamma$ is proportional to r^2, with r the radius of the nucleus that has been crystallized. The other two terms are proportional to r^3. When examining figure 1.5 it becomes apparent that amorphisation will lead to an energy reduction when the clusters are smaller than the critical cluster size, r^*. Similarly an increase of the cluster beyond the r^* reduces the energy. So for clusters with radii larger than r^* the *nuclei* tend to grow, for smaller clusters the *nuclei* shrink [47].

Heterogeneous nucleation

Heterogeneous nucleation occurs at preferential sites at which the effective surface energy is lower, lowering the free energy barrier to form a

more stable phase. Foreign particles can induce a local energy benefit, while the nucleation process remains quite similar to the homogeneous process. As described in subsection 1.1.3, the structure of a-Si:H can vary depending on the deposition method and settings. Based on studies of the a-Si:H nanostructure [38, 37, 48, 49] the possible presence of preferential sites within the a-Si:H matrix should be considered as a possible trigger to the nucleation process of a-Si:H. Surfaces can also act as preferential sites, as they promote nucleation because of interfacial tensions. These influence $A\gamma$ and $V\Delta G_{\mathrm{s}}$ in equation 1.5.

1.3 Solid phase crystallisation for silicon solar cells

In the early 90'ies Tanaka et al. [50] and Matsuyama et al. [51] introduced solid-phase crystallisation (SPC) as a method to fabricate thin-film polycrystalline silicon for solar cells. Brendel and Scholten [52] calculated that single-junction c-Si thin film solar cells (1 to 3 μm) could result in efficiencies of 17% when appropriate light trapping is applied. The company *CSG Solar* made modules using SPC produced thin film solar cells on glass [53]. After crystallisation of the $n^+/p/p^+$ stack both rapid thermal annealing (RTA) and plasma hydrogenation were used to improve the intergrain quality and electrical passivation of defects [54, 55, 56], and they demonstrated modules with a 10.5% efficiency [57]. These promising results prompted the scientific community to further investigate the possibilities of SPC for PV on glass. The crystallisation of hydrogen-free a-Si films deposited by e-beam was investigated by the Helmholtz Zentrum Berlin [58]. Aluminium induced crystallisation (AIC) also caught the attention of the community, because of the enhanced crystallisation rate compared to SPC and in-situ doping of the Si films by Al. This metal induced crystallisation was already reported in the late 70'ies. Nast et al. [28, 59] proposed to use this effect to produce thin-film crystalline silicon for solar cells.

Parallel to the development of thin film crystalline silicon solar cells using SPC, the concept of a-Si/c-Si heterojunction solar cells was introduced by Tanaka et al. [50]. They envisioned an a-Si/c-Si heterojunction with intrinsic thin-layer (p/i/n) solar cells design: HIT (Heterojunction with Intrinsic Thin-layer). Their design, using a 10 μm thick poly-Si layer created by SPC of CVD deposited phosphorous-doped a-Si, resulted in a cell with an 6.3% conversion efficiency [51]. The version of this solar cell design based on an a-Si:H(p^+) emitter on a $\sim$100 μm thick c-Si(n) wafer has resulted in an efficiency of 24.7% [60]. The Interdigitated Back Contacted (IBC) structured HIT cell even resulted in a 26.6% efficiency [61].

IMEC combined the AIC with a heterojunction design. A solar cell with an 8.5% efficiency was realised using a heterojunction a-Si/poly-Si design with light trapping texturing and hydrogen passivation by remote plasma [62]. They made use of a so-called seed layer using AIC followed by the epitaxial growth of poly-Si using CVD at temperatures beyond 1100 °C [62].

A serious competitor for SPC is liquid phase crystallisation (LPC). LPC can be achieved both through electron beam crystallisation (e-beam) or laser induced crystallisation (LIC). Efforts by Dore et al. [63], Haschke et al. [64], and Amkreutz et al. [65] have increased the efficiency of silicon heterojunction solar cells on glass to above 14% [66]. Although LPC is currently a promising route to thin film silicon solar cells on glass, the efficiency record for thin film silicon PV modules on glass is still held by CSG Solar using SPC [67].

1.4 Scope and outline of this dissertation

This dissertation is part of a study into the development of thin film poly-crystalline silicon based HIT solar cells with light trapping features. Thin film poly-Si solar cells would require a thickness of approximately 10 μm to ensure sufficient light absorption [3]. The deposition

of films with such a thickness requires high deposition rates, in this case Expanding Thermal Plasma Chemical Vapour Deposition (ETPCVD). This dissertation will discuss the crystallisation of a-Si:H films deposited by ETPCVD.

Different from the crystallisation process of a molten material, the mobility of atoms during the solid-phase crystallisation process is limited. For this reason the configuration of atoms prior to the crystallisation process can strongly influence the onset and time required for crystallisation. In the case of a-Si:H, not only a reconfiguration of the Si atoms is needed. The solubility of hydrogen atoms in c-Si is much lower than in a-Si:H [4] and for this reason hydrogen atoms must diffuse out of the film during annealing. Therefore information on the structure of the amorphous films prior to crystallisation is essential. In this thesis the silicon microstructure and the hydrogen bonding configuration of as-deposited films are studied, and in particular their influence on the crystallisation process.

For thin film polycrystalline Si to be used for solar cell applications, they must be doped. This can be achieved by doping after crystallisation, but also by crystallising films which already contain the dopant atoms. The main benefit of in-situ doping of the a-Si:H film is a reduction in processing steps. Until this work, no doped a-Si:H films were produced using ETPCVD. This dissertation will discuss the deposition of boron doped a-Si:H films by ETPCVD. As dopants can influence the crystallisation process for a-Si films [5], th crystallisation of intrinsic and boron-doped films is studied by in-situ x-ray diffraction during the crystallisation process.

In order to characterize the structure of a-Si:H by Raman spectroscopy (RS) in addition to Fourier transform infrared spectroscopy (FTIR) a comparison is made between the Si-H_x related modes detected by both techniques. This is presented in chapter 3. Chapter 3 shows the relation between the microstructure parameter R^* determined from RS and FTIR. Chapter 4 presents the first boron doped a-Si:H films produced by ETPCVD. The boron content and the doping efficiency of these films is compared to those produced by PECVD. To study the crystallisation we have opted to measure x-ray diffraction of the

a-Si:H films during annealing, thereby observing the phase transition from amorphous to crystalline silicon. Chapter 5 discusses these results and the influence of the microstructure and hydrogen content from the a-Si:H films on the crystallisation process. In chapter 6 both the influence of the microstructure and boron doping on the crystallisation of a-Si:H are presented. The influence of boron on both the nucleation rate and the grain growth rate is discussed.

1.5 Contribution to the field

The focus of this work is the solid phase crystallisation of a-Si:H on glass for solar cell applications. In this work three main topics are discussed: the evaluation of the microstructure parameter of hydrogenated amorphous silicon (R^*) by Raman spectroscopy, the deposition of boron doped a-Si:H layers by ETPCVD, and the crystallisation of intrinsic and B-doped a-Si:H layers on glass deposited by ETPCVD. The work described in this thesis has contributed to the research field with the following new results:

- Fourier Transform Infrared Spectroscopy is frequently used to detect the Si-H_x stretching modes to determine the microstructure parameter R^* of a-Si:H films. The stretching modes can also be detected by Raman Spectroscopy. In contrast to FTIR, Raman Spectroscopy can make substrate independent, contactless measurements. This work demonstrates the relation between the R^* determined from both measurement techniques.

- The first boron doped a-Si:H films deposited by Expanding Thermal Plasma CVD are presented in this work. The films are compared to B-doped a-Si:H films deposited by PECVD. The B content increases with increasing B_2H_6-to-SiH_4 ratio for both deposition techniques. The B content is independent of the deposition temperature for ETPCVD films but decreases with increasing deposition temperature for PECVD films.

- The crystallisation of a-Si:H films deposited by Expanding Thermal Plasma CVD by solid-phase crystallisation is studied in-situ using x-ray diffraction. The hydrogen content and bonding configuration in the films is shown to influence the crystallization process, specifically an increase in R^* decreases the crystallisation rate.

- Both the influence of R^* and the boron content on the solid phase crystallisation of a-Si:H are studied in this work. B is shown to enhance the grain growth rate of the a-Si:H films, but the effect of the B content on the nucleation rate is limited. The extent of the enhanced grain growth rate due to B doping is controlled by the B_2H_6-to-SiH_4 gas flow ratio, for both PECVD deposited films and ETPCVD deposited films.

Chapter 2

Experimental procedures and details

In this chapter the experimental methods are described. First the deposition methods are explained and then the measurement techniques used to characterise the material structure of the produced thin films are discussed. The last part of the chapter explains how the opto-electronic properties of the films are determined.

2.1 Deposition of a-Si:H

2.1.1 Plasma Enhanced Chemical Vapour Deposition

An approach to produce a-Si:H is through chemical vapour deposition (CVD). In CVD the deposition compounds are brought in contact with a substrate while in a vaporized state and condense on the substrate surface. Often a plasma is used to enhance the chemical reaction rates

of the precursor gas: Plasma Enhanced Chemical Vapour Deposition (PECVD). For the deposition of Si films, silane (SiH_4) is a common precursor gas. For laboratory and industrial deposition of a-Si:H radio-frequency plasma enhanded CVD (rf PECVD) is common and will be used in this thesis. This method uses an 13.56 MHz rf signal to generate a plasma discharge between two electrodes. This plasma ionizes the precursor gasses in the deposition chamber, such as SiH_4, H_2, and B_2H_6 for doped films. This results in silicon containing radicals (Si_xH_y), hydrogen radicals, molecules, and ions in the gas. Of the different species the SiH_3 radical is the dominant precursor for a-Si:H growth [68]. The radicals reach the substrate by diffusion and form a film on the substrate surface.

The PECVD films discussed in this work are made in a parallel plate rf PECVD setup as is shown in figure 2.1. The rf electrode has an area of 12 cm × 12 cm and on the grounded electrode substrates with a maximum size of 10 cm × 10 cm can be placed. The distance between the electrodes is 10 mm for depositions of intrinsic a-Si:H and 11 mm for doped a-Si:H. P-type doped films were made in chambers designated for p-type depositions. The substrate is placed top down between the electrodes and is in direct contact with the plasma. The substrate is preheated using an electric heater.

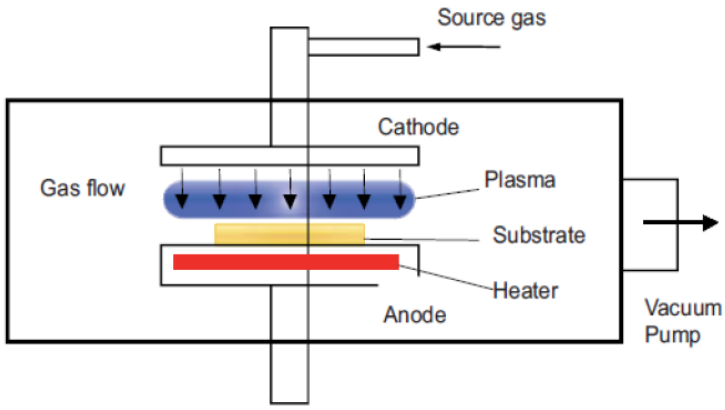


Figure 2.1. A schematic of a parallel plate rf PECVD reactor.

2.1.2 Expanding Thermal Plasma CVD

Most depositions reported in this work were carried out in the main deposition reactor of the Cascaded Arc Solar Cell Apparatus Delft Eindhoven (CASCADE), at Delft University of Technology (TUD). The main chamber holds the expanding thermal plasma CVD (ETPCVD) reactor. This method, developed at Eindhoven University of Technology (TU/e), was developed with the aim to deposit various materials at high growth rates [69, 70, 71]. With this technique a-Si:H films can be grown at deposition rates up to 11 nm/s [72]. ETPCVD is a remote plasma technique so the substrate is not in direct contact with the region where the plasma is created. ETPCVD allows for deposition of a-Si:H within a broad range of micro-structures [73], due to the independent manipulation of plasma and substrate conditions.

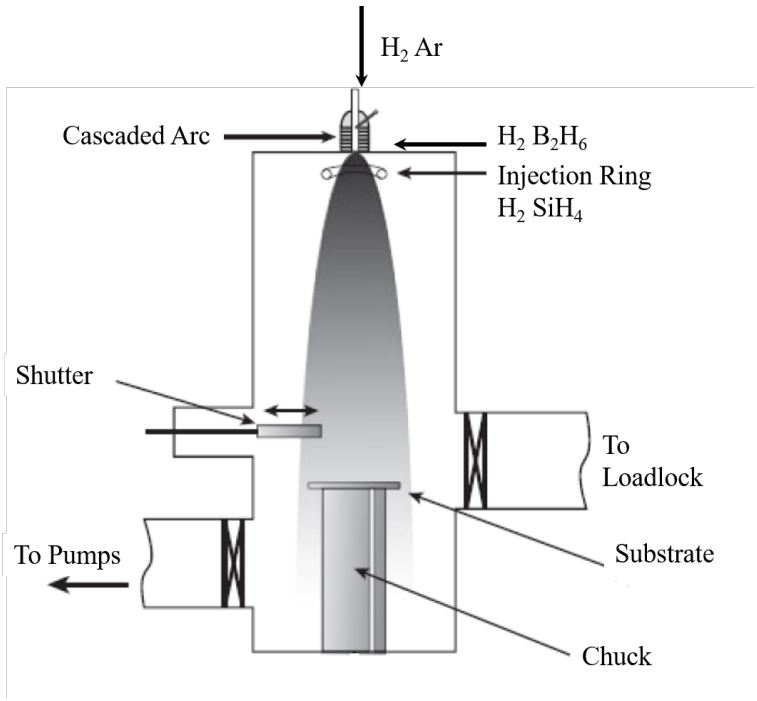


Figure 2.2. A schematic of the ETPCVD reactor.

A schematic representation of the ETPCVD reactor can be seen in figure 2.2. At the top of this reactor is the cascaded arc source. In the arc a DC Ar-H_2 plasma is created from Ar and H_2 gasses between the cathode tips and the anode plate. The current in the arc is 40 A. The plasma travels in a narrow channel (2.5 mm in diameter) at a pressure of approximately 45×10^3 Pa and expands supersonically into the deposition chamber. The pressure in the deposition chamber is typically around 20 Pa. At the end of the nozzle H_2 is injected, while for B-doped films B_2H_6 is added to the H_2 flow. Approximately 4.5 centimetres below the end of the nozzle an injection ring injects SiH_4. The gases injected via the nozzle and the injection ring are dissociated and sometimes ionized by the expanding plasma [39]. The substrate is placed approximately 40 cm below the nozzle, face up, on a temperature controlled substrate holder.

All intrinsic films have been deposited prior to the connection of the B_2H_6 gas lines to the setup.

2.2 Structural film characterisation

2.2.1 Fourier Transform Infrared Spectroscopy

Fourier Transform InfraRed spectroscopy (FTIR), measures the wavelength dependent absorption in the infrared wavelength range. When the frequency of the infrared radiation matches the resonant frequency of the bond or group that vibrates in the material a fraction of the light is absorbed. One restriction is that only vibrations with a transition dipole moment are infrared active. A list of Si-H, Si-H_2 and Si-H_3 is shown in table 2.1, the stretching and wagging modes are used to characterise a-Si:H [74].

The hydrogen bonding in a-Si:H is investigated by infrared absorption measurements using a Thermo Electron Nicolet 5700 Fourier Transform Infrared Spectroscope. Measurements were made in the range of 400 to 6000 cm^{-1}.

The FTIR measurements were made on films deposited on lowly doped c-Si wafers. The raw FTIR spectra were corrected for absorption in the c-Si wafer by measuring the spectrum of the bare wafer. The interference fringes were fitted, characterizing the spectra of the samples in the non-absorbing spectrum range. The parameters for the fitting of the interference fringes are the film thickness and the refractive index in the infrared (n_∞). The absorption peaks are fitted by multiple gaussian interpolations representing the absorption bands related to the material structure. An example of the analysis of the stretching modes (SM) is shown in figure 2.3.

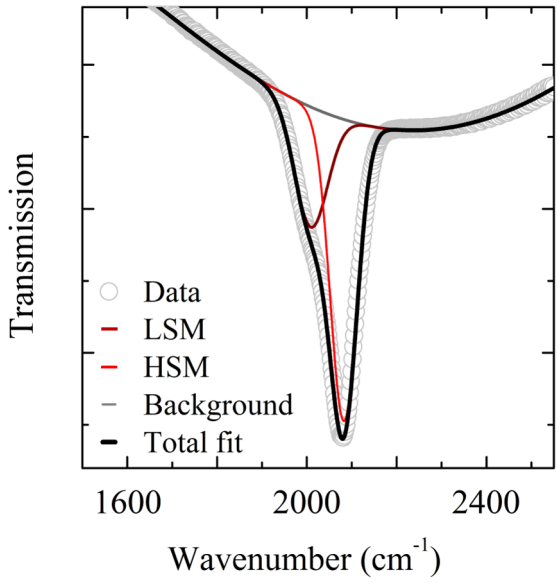


Figure 2.3. Example of a typical FTIR measurement of the stretching modes, showing both the background and the two fitted gaussians.

The wagging mode of all hydrogen in the film contributes to the absorption peak at $\omega \approx 630$ cm^{-1} [75, 74]. Two stretching modes are present in the spectra. The low stretching mode (LSM) is found at $\omega \approx 2000$ cm^{-1} and the high stretching mode (HSM) at $\omega \approx 2100$ cm^{-1} [75, 74]. The

areas of the absorption peaks are used to calculate the density of corresponding chemical bonds N_x through the corresponding proportionality constant A_x, according to 2.1.

$$N_x = A_x I_x = A_x \int \frac{\alpha(\omega)}{\omega} \mathrm{d}\omega \tag{2.1}$$

In here, $\alpha(\omega)$ is the absorption coefficient and I_x is the integrated absorption of the specific peak. The proportionality constants used in this work are $A_{630} = 2.1 \cdot 10^{19}$ cm^{-2} and $A_{\mathrm{LSM}} = A_{\mathrm{HSM}} = 9.1 \cdot 10^{19}$ cm^{-2} [73, 38]. The atomic hydrogen concentration c_{H} of the films can be determined by the hydrogen and silicon densities N_{Si} and N_{H} as follows [76]:

$$c_{\mathrm{H}} = \frac{N_{\mathrm{H}}}{N_{\mathrm{Si}} + N_{\mathrm{H}}} \tag{2.2}$$

where $N_{\mathrm{Si}} + N_{\mathrm{H}}$ is assumed to be around $5.3 \cdot 10^{22}$ cm^{-3} [76].
The microstructure paramater R^* is defined as follows

$$R^* = \frac{I_{\mathrm{HSM}}}{I_{\mathrm{LSM}} + I_{\mathrm{HSM}}} \tag{2.3}$$

Where I is the integrated intensity as defined in equation 2.1. Films of a-Si:H suitable for solar cell application typically have an $R^* < 0.1$. It has been demonstrated in literature that such layers have a high material density and low defect density, leading to a high photo-response (defined as the ratio between the photo-conductivity and dark conductivity) [73, 38]. Films with higher R^* are commonly observed to have low material density and high defect density, resulting in a low photo-response.

In this work the R^* will also be evaluated using Raman spectroscopy, see Chapter 3. In this case the I_{LSM} and I_{HSM} are the integrated intensities of the counts measured for the specific Raman shift.

Table 2.1. Si-H vibrations for Si-H, Si-H_2, and Si-H_3 as described by Luckovsky et al. [75]. The table shows the character of the vibrational mode, the activity (ir for infra red absorption, R for Raman scattering), and the estimated frequency.

Structural group	Mode	Activity	Est. frequency
Si-H	Stretch	ir, R	2000
	Bend	ir	650
Si-H_2	Stretch	ir, R	2100
	Bend-scissors	ir, R	900
	Wag	ir, R	850
	Twist	R	820
	Rock	ir, R	650
Si-H_3	Stretch	ir, R	2150
	Degenerate deformation	ir, R	900
	Symmetric deformation	ir, R	850
	Wag, Rock	ir, R	630

2.2.2 Raman Spectroscopy

Raman spectroscopy (RS) measures the Raman effect [77], which is a shift in the wavelength of light (photons) that occurs when a photon scatters inelasticly with atoms or molecules. Specifically the energy difference measured by the Raman effect is equal to the difference of vibrational and rotation energy-levels in molecules or the specific allowed phonon energies in crystals [78]. In amorphous materials the spectral features observed in the spectra of crystals are broadened. For vibrations to be Raman active a change in polarisability of the transition is required. RS is often used as a complementary technique to FTIR, as RS can detect the vibrations of the Si-Si bonds (phonons) in the a-Si:H. For amorphous silicon the active phonons are the transverse optical (TO) mode[1] at approximately 480 cm^{-1}, the longitudinal optic (LO) mode at 400 cm^{-1}, the longitudinal acoustic (LA) mode at 300 cm^{-1}, and the transverse acoustic (TA) mode at around 130 cm^{-1} [79]. The disorder of the amorphous structure can be characterised by the

[1]For crystalline Si the TO mode is at 520 cm^{-1}.

width Γ_{TO} of the TO peak and its frequency shift ω_{TO}. Γ_{TO} increases roughly linearly with the increase in distortion and ω_{TO} is related to the Si-Si bond length [80, 81]. The higher the shift towards smaller frequencies the longer the average bond length. A decrease in ω_{TO} indicates a higher disorder in the amorphous silicon. Some hydrogen vibrations are also Raman active and visible in Raman spectra[75]. Table 2.1 shows a list of Si-H_x vibrational modes. Both the LSM and HSM of the Si-H_x bonds can be detected [82] as well as the wagging and rocking mode at approximately 630 cm^{-1} [79].

The volume of material that is probed in a measurement is dependent on the focus of the laser and the wavelength dependent absorption coefficient, α_λ of laser light by the film [83]. The actual sensitivity for detection also depends on the probability of the Raman effect under influence of the applied laser, the cross section σ_R, which can be wavelength dependent [83].

RS spectra of the films were measured using a Renishaw In Via RS using a 514 nm Ar laser and an 633 nm HeNe laser. The spectra are measured from 180 to 800 and from 1700 to 2400 cm^{-1} and have a resolution of 2 cm^{-1}. The laser focus is set manually. The two ranges are measured consecutively.

The evaluation of the RS spectra is split into two parts, the 250 to 850 cm^{-1} range and the 1700 to 2400 cm^{-1} range. The first range is fitted with six gaussians and a constant baseline, see figure 2.4 (a). The baseline is set to the lowest point of the spectrum. The gaussians are related to the four Si phonon modes, TA, LA, LO and TO, and the hydrogen related 630 cm^{-1} mode.

The second range is fitted using a second degree polynomial for the background signal and two gaussians, see figure 2.4 (b). In analogy to FTIR detection of the Si-H_x, the integrated intensities of the RS spectra I_{LSM} and I_{HSM} are used to determine the RS R^* (or R^*_{RS}), through equation 2.3. Futher details about the detection of Si-H_x related features in the RS spectra can be found in chapter 3.

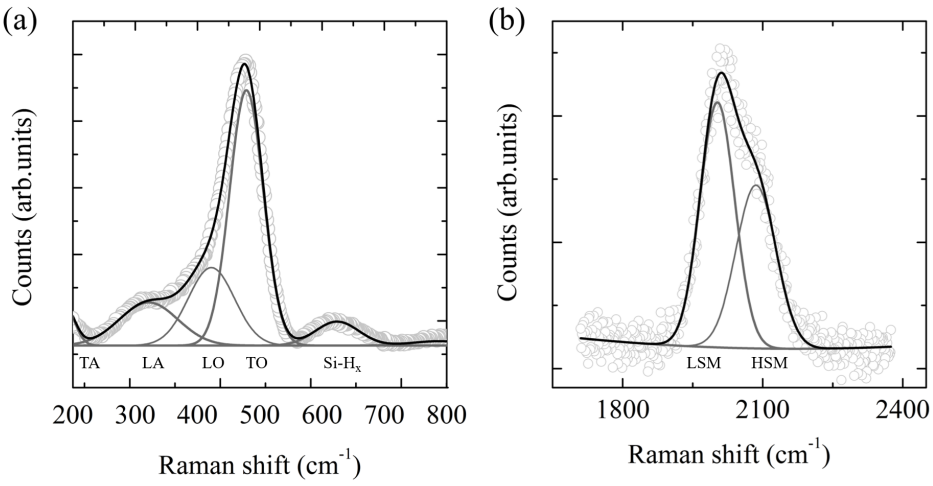


Figure 2.4. Example of fitting RS measurement with (a) six gaussians and a constant baseline and (b) with two gaussians and a polynomial background.

2.2.3 X-ray diffraction

X-ray diffraction (XRD) occurs when an incident beam of X-rays scatters on the atomic planes of a crystalline material and the X-rays interfere with each other while leaving the crystal, see figure 2.5. This interference can be measured and the average spacing between layers or rows of atoms (d) can be determined from the interference pattern by Bragg's law [84], equation 2.4.

The constructive interference of the scattered X-rays is strongest for angles of θ that satisfy Bragg's law:

$$\lambda = 2d \sin\theta \tag{2.4}$$

where λ is the wavelength of incident light.

The red lines in figure 2.6 show the XRD pattern of a polycrystalline silicon reference powder. The peaks in the pattern are labelled using Miller indices [86]. The Miller indices indicate the family of lattice planes by three integers: h, k, and l. The peak due to the diffraction from the $\{111\}$ planes is strongest in the pattern of crystalline Si.

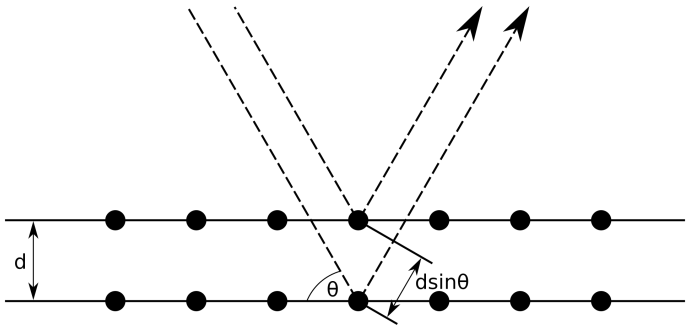


Figure 2.5. Schematic of the geometrical requirements of Bragg's law. Light scattered from the atom planes produce an angle dependent interference pattern [85].

For chapters 5 and 6 of this thesis XRD is used to monitor the development of the crystalline fraction upon annealing by measuring c-Si related peaks. Two measurement types are used: ex-situ and in-situ. Ex-situ measurements are used to evaluate the crystalline material. The blue line in figure 2.6 shows the pattern from a crystallized Si film on a glass substrate. The positions of the peaks indicate that the sample contains crystalline silicon. The ratio between the intensity of the lines matches that of the reference powder. This means that no preferential grain orientation is observed for this sample. In-situ XRD is used to monitor the phase transformation from a-Si:H into poly-Si. Both types of XRD measurements were carried out in Anton Paar high-temperature chamber HTK 1200 setups (see figure 2.7(a)). The actual setup and chamber conditions are specific to the experiments and details can be found in the relevant chapters. In all cases the XRD patterns were collected by an automatic powder diffractometer in symmetric geometry, using Copper Kα characteristic radiation (λ = 0.154 nm). The irradiated area of the samples was 10 mm $\times$ 10 mm. The in-situ XRD patterns were measured from 26 to 31° (2θ), where the strongest silicon line of {111} planes is located. A typical measurement is shown in figure 2.7(b). Ex-situ measurements were made over a range of 15 to 65° (2θ), these patterns include the three strongest silicon lines, {111} {220} and {311}.

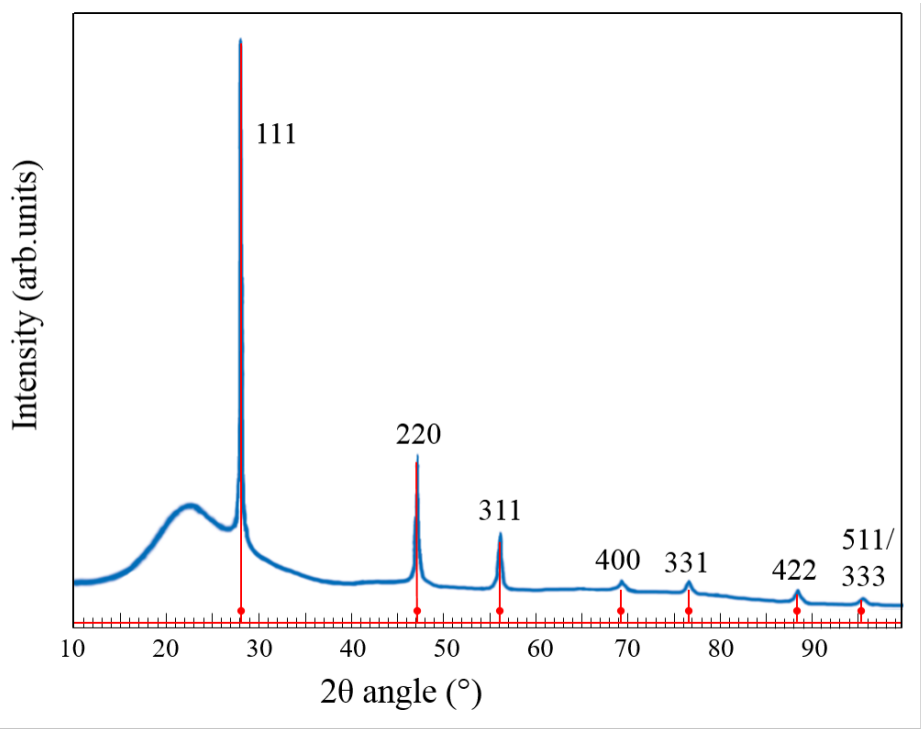


Figure 2.6. Complete XRD pattern for polycrystalline silicon reference powder (red line), red dots indicating the expected line positions [87] and polycrystalline silicon on glass (blue line) showing both the signal from the silicon and the glass background. The polycrystalline example sample was deposited at substrate temperature of $400\ ^{\circ}\mathrm{C}$ and was annealed at $600\ ^{\circ}\mathrm{C}$ for 8 hours.

The XRD patterns were preliminary processed using an Xpert HighScore plus software package (background determination and subtraction, removal of the Kα_2 component). In order to obtain the basic parameters of the lines (2θ peak position, intensity, full width half maximum (FWHM) and integrated intensity), diffraction line profiles were then approximated by a Pearson VII function using a least square procedure.

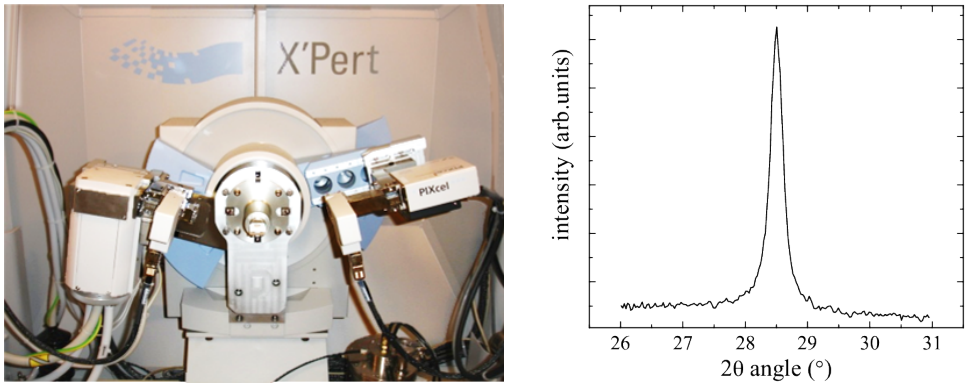


Figure 2.7. Example of (a) the Anton Paar high-temperature chamber HTK 1200 (b) an XRD pattern showing the {111} line of silicon as measured during the annealing procedure.

As a measure for crystallization, the crystalline fraction, χ, was determined by normalizing the integrated intensity of the {111} line during crystallization with respect to the average integrated intensity of the {111} line of the film after saturation of crystallisation occurred. This fully crystallized film will be referred to as the material with crystalline fraction χ=1, see figure 2.8.

In the S-shaped crystallization curves (see chapters 5 and 6) we distinguish two separate parts: (i) the time until the onset of crystallization, and (ii) the curve from the onset of crystallization until crystallization saturation (full crystallisation). The time to full crystallization is affected by the onset or retardation time and the slopes of the crystallization curves. In order to quantify these aspects the measured crystalline fractions are fitted using the Avrami, Johnson and Mehl (AJM)

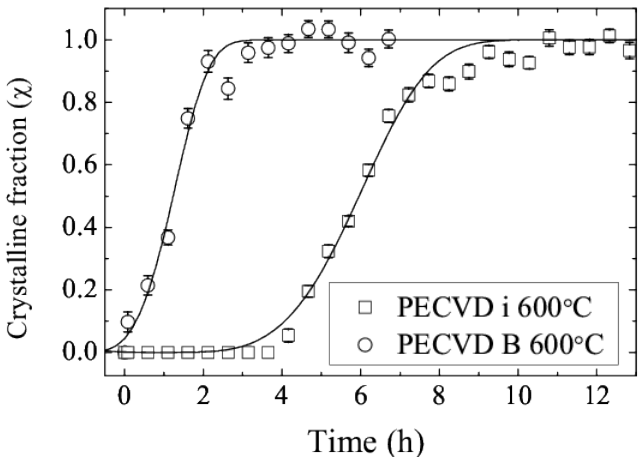


Figure 2.8. The results of the in-situ XRD measurements of the {111} diffraction line for two ETPCVD deposited samples. The markers show the crystalline fraction χ as a function of annealing time. The lines show the AJM model fitted to the χ(t).

model [88, 89, 90, 91]. Avrami, Johnson and Mehl [88, 89, 90, 91] used a phenomenological approach to develop an expression for the crystalline fraction as a function of annealing time. The AJM description can be applied to many different nucleation processes. In fact the same equations can be constructed from a classical model for nucleation of a solid from a liquid or gas phase [33]. The basic assumption of this model is that no nucleation or growth occurs during the retardation or effective lag time, θ, and that any misfit strain is negligible. According to the AJM model, θ is related to the minimum detectable grain size or crystalline material volume and is therefore dependent on the detection limit of the measurement technique. In the model, the nucleation rate is defined as the increase of grain density per unit time and is assumed to reach steady-state value (I_s in $\mathrm{cm}^{-2}\ \mathrm{s}^{-1}$) when $t = \theta$ [91]. The grain growth rate, ν_g, is assumed to be time independent. With this assumption the crystallized volume fraction, χ, as function of annealing time can be expressed as:

$$\chi(t) = 1-\exp(-(\tfrac{t-\theta}{\tau_c})^4) \tag{2.5}$$

In here τ_c is the crystallization time, defined as:

$$\tau_c = (3/\pi d I_s {\nu_g}^3)^{\frac{1}{4}} \tag{2.6}$$

with d the film thickness. The grain growth rate ν_g is directly related to the jump rate of atoms at the surface of a grain [92, 47]. I_s and the ν_g are typically described by Arrhenius type equations [91]. However, often ν_g is simplified with a single Arrhenius equation with an associated activation energy of SPC ($E_{a,SPC}$) [93]. In a similar fashion an Arrhenius equation is often used to evaluate the activation energy of the onset time to nucleation, θ.

An estimation of the crystallite size was calculated using a procedure that is based on a Voigt function analysis of the widths of diffraction lines (FWHM and integral width $\beta = \text{area}/I_0$) proposed by Langford [94], where I_0 is defined as the peak height.

2.3 Opto-electrical film characterisation

2.3.1 Optical transmission and reflection

Light incident on a thin film of material can be reflected, transmitted, or absorbed. The absorption (A) is determined according to $A = 1-R-T$, where (R) is the reflection and (T) the transmission. The optical properties of a-Si:H layers are determined from a measurement of the reflection and transmission as a function of wavelength. For the extraction of the optical properties from the measurements a model is used [95], taking into account the optical properties of the substrate glass. In essence, the model uses the interference fringes that can be observed in the reflection and transmission spectra.

The complex refractive index, $\tilde{n} = n + ik$, of the film can be determined. The real part n is the refractive index, and the imaginary part k is the extinction coefficient. The extinction coefficient is related to the absorption coefficient α by:

$$k = \frac{\alpha\lambda}{4\pi} \tag{2.7}$$

The optical bandgap is determined from the optical constants according to Klazes method [96]. The optical bandgap is determined by extrapolation $[\alpha(E)n(E)E]^{1/(1+p+q)}$ versus the photon energy E to $\alpha(E) = 0$, for $\alpha \geq 10^3$ cm^{-1}:

$$(\alpha(E)n(E)E)^{1/(1+p+q)} = B_g \cdot (E - E_g) \tag{2.8}$$

where $\alpha(E)$ is the absorption coefficient, $n(E)$ the refractive index, p and q are the constants related to the shape of the band edges and B_g is a prefactor. Klazes et al. [96] proposed that the density-of-states distribution near the band edges can be assumed to be linear ($p = q = 1$), resulting in the following equation for the Klazes, or cubic gap E_g:

$$(\alpha(E)n(E)E)^{1/(3)} = B_g \cdot (E - E_g) \tag{2.9}$$

In this work the cubic (or Klazes) bandgap is determined.

The transmission and reflection (RT) of the films on glass substrates are measured using a Theiss RT setup. The setup consists of a 50 W halogen lamp, a monochromator and filters. The Theiss software model is used to calculate the absorption. The input for the model is the reflected light and the transmitted light which are measured directly by separate photodiodes. The model takes into account the optical properties of the Corning Eagle 2000 glass substrate and determines the film thickness from the interference fringes. The wavelength range of 375 nm to 1060 nm is measured and the complex refractive index and the cubic bandgap are determined.

2.3.2 Dark IV and activation energy

The conductivity of a material is defined by the mobility and concentration of free charge carriers in the material according to:

$$\sigma = e(\mu_e n + \mu_h p), \tag{2.10}$$

where μ_e is the electron mobility, μ_h is the hole mobility and n and p are the electron and hole concentration, respectively. At thermal equilibrium the charge carrier densities in the material can be expressed as:

$$n_0 = N_c e^{(E_F - E_c)/kT} \tag{2.11}$$

$$p_0 = N_v e^{(E_v - E_F)/kT} \tag{2.12}$$

Where N_c and N_v are the effective density of states in the conduction and the valence band, which in turn are dependent on the temperature $N \propto T^{3/2}$.

For p-type material the electron concentration is negligible, so equation 2.10 can be simplified to

$$\sigma = e\mu_h p \tag{2.13}$$

By increasing the temperature, the effective density of states at the band edges increases while the exponential portion of the equation decreases. The activation energy of the dark conductivity, E_a, is determined from the temperature dependence of the dark conductivity according to:

$$\sigma_{\mathrm{D}}(T) = \sigma_0 \exp \frac{-E_a}{kT} \tag{2.14}$$

with E_a the activation energy, k Boltzmann's constant, and T the temperature.

Samples are prepared by depositing two coplanar aluminium electrodes on the a-Si:H films and annealing them at 130 °C to ensure good contact. The contact deposition is done using e-beam evaporation in a Provac PRO500S metal evaporator. Using a Keithley 617 electometer, a voltage (V) of usually 10 V is applied to the contacts and the current (I) is measured. The dark conductivity is determined by:

$$\sigma_{\text{D}} = \frac{I}{V} \cdot \frac{d}{tL} \tag{2.15}$$

where d is the gap between the contacts (0.5 mm), L is the length of the contacts (20 mm), and t is the film thickness. During the measurement, the temperature is controlled by a temptronics Thermo-Chuck. The current measurement starts at 130 °C and is cooled down to 60 °C in steps of 5 °C.

2.3.3 Hall effect

The Hall effect occurs when a conductor or semiconductor is placed in a magnetic field and current (I) is flowing through the material perpendicular to the magnetic field. The Lorentz force, F_L, induced on a charge particle by the magnetic field is:

$$F_L = qvB \tag{2.16}$$

where q is the charge on the particle, v is the velocity and B the strength of the magnetic field.

The electron velocity of the current flowing through to the material is:

$$\upsilon = \frac{I}{nAq} \quad , \tag{2.17}$$

where n is the electron density, A is the cross-sectional area of the film and q is the elementary charge. When the external magnetic field is

applied perpendicular to the direction of current flow, the Lorentz force on the electrons will become:

$$F_L = \frac{IB}{nA} \tag{2.18}$$

This results in a separation of positive and negative charge carriers. The separation induces an electric field perpendicular to the direction of current flow, which generates the potential difference in the material, the Hall voltage (the electric field is assumed to be homogeneous).

$$V_H = w\epsilon \tag{2.19}$$

In this equation w is the width of the sample and ϵ is the electric field strength, which is:

$$\epsilon = \frac{IB}{qnA} \tag{2.20}$$

Applying equation 2.20 to equation 2.19 gives:

$$V_H = \frac{IB}{qnd} \tag{2.21}$$

where d is the film thickness.

The sheet resistance is determined from the measured voltage difference between the four outer positions of the samples and depends on the overall Hall voltage according to:

$$R_s = \frac{IB}{q|V_H|} \tag{2.22}$$

The resistivity of the films, assuming that the doping concentration is much larger than the intrinsic carrier concentration, is:

$$\rho = \frac{1}{qp\mu} \tag{2.23}$$

where p is the doping level for p-doped material and μ the carrier mobility.

The measurement of the Hall effect is done using the Van Der Pauw method. This method allows us to calculate the carrier concentration and mobility in the poly-Si. The setup used for these measurements is the Ecopia Hall Effect Measurement System HMS-5000, the system software was used to calculate the film properties. The samples were cut in to squares and contacted at the corners. The complete measurement and calculations were executed four times for each sample, values shown in this thesis are the average of these four measurements.

Chapter 3

Comparison of FTIR and RS for the characterisation of a-Si:H

3.1 Introduction

Hydrogen bonding configurations in hydrogenated amorphous silicon (a-Si:H) are directly related to the Si-Si network structure (voids, divacancies, multivacancies) [38, 73, 97]. Presence of hydrogen influences the electrical properties of the material, in particular the defect density. Amorphous silicon (a-Si; i.e., material that does not contain hydrogen) [30, 31] typically has a defect density of 10^{19} to 10^{21} cm^{-3}. Incorporation of hydrogen reduces this large density of electronically active dangling-bond defects from 10^{19} cm^{-3} in a-Si to 10^{15} cm^{-3} in a-Si:H [32, 33]. Hydrogen is usually incorporated during the deposition process when SiH_4 is used as the precursor gas for film growth. In the deposition process of a-Si:H hydrogen is of great influence to the material structure as is shown by Kessels et al. [39]. The growth conditions of the film determine the material structure and

the hydrogen concentration in the film. Hydrogen is important in both the thermodynamic approach of film growth [40, 41, 42] and in kinetic growth models including surface processes [43, 44].

Annealing a-Si:H layers at temperatures around 600 °C alters the Si-Si structure due to hydrogen effusion and crystallisation [98]. This makes identification of the a-Si:H structures a requisite for crystallisation studies discussed discussed in Chapters 5 and 6. The solubility of H in c-Si is in the order of 10^{16} cm^{-3} while up to 25% H can be present in a-Si:H [4, 99] and therefore full crystallisation requires effusion of H. In turn, the H effusion characteristics of a-Si:H are very dependent on the microstructure of the material.

The atomic hydrogen content (c_{H}) and the manner in which hydrogen is incorporated in a-Si:H can be evaluated by Fourier transform infrared spectroscopy (FTIR) [100, 101, 34]. FTIR measures the absorption of infrared light by the a-Si:H film. Typically the Si-H$_{(x)}$ wagging modes, as well as the Si-H$_{(x)}$ stretching modes are used to determine the c_{H}. The configuration of the H atoms within the Si structure, a.o. the presence of clustered hydrogen, is derived from the Si-H$_{(x)}$ stretching modes. R^*, the microstructure factor [102], is a figure of merit for the atomic configurations in the bulk of the film. For R^* values > 0.5 (for c_{H} of 14%) a-Si:H films have been described as void dominated [73]. The presence of clustered hydrogen is important for the H effusion process [4]. Unfortunately, FTIR measurements can only be carried out on films deposited on IR-transparent substrates, such as c-Si wafers. The substrate on which the film is grown can influence the a-Si:H growth process as well as the kinetics of the solid phase crystallisation (SPC), and therefore it is desirable to measure a film that is deposited on the same substrate as is used for the SPC process.

Cardona [82] and Volodina and Koshelev [103] were able to detect the low and high stretching modes 2000 cm^{-1} and 2100 cm^{-1} using Raman Spectroscopy (RS). RS allows for substrate independent measurements of the a-Si:H films. Additional advantages of RS include

the laser dependent collection depth. Using different wavelengths for RS measurement, the depth to which the film is probed can be controlled. In this manner inhomogeneities in the growth direction can be evaluated. In order to use RS for studying the hydrogen configurations in a-Si:H films, a comparison must be made between RS and FTIR results. Another reason to compare RS with FTIR for a-Si:H characterisation is that the complete evaluation of Si films by RS would simplify the characterisation process of a-Si:H, μ-Si, and poly-Si. Being a fast and contactless measurement, RS can be used to make surface scans, allowing identification of crystals as well as characterising the a-Si:H material.

This chapter will evaluate if the detection of the Si-H_x modes by RS is sufficient to determine the a-Si:H structure similar to the characterisation by FTIR. First the measurement techniques, set ups and procedures are presented in section 3.2. Section 3.3 shows a comparison of the Si-H_x modes measured by RS to those determined by FTIR. Finally, the comparison of the results from both techniques is discussed.

3.2 Experimental

Samples

The samples are deposited on Corning glass and c-Si wafer substrates simultaneously by ETPCVD. This deposition technique is explained in section 2.1.2. The gas flows during the depositions are 570 sccm of Ar, 340 sccm H_2, and 230 sccm SiH_4. The arc current is set to 40 A, the arc pressure ranged from 40 - 49 kPa, the chamber pressure varied from 17 - 30 Pa and the substrate temperature range is 200 to 375 °C. The film thickness varies between 300 and 1000 nm. The samples are characterised using FTIR and RS. The details of the analysis of the FTIR and RS spectra are described in sections 2.2.1 and 2.2.2, respectively. The measurement principles and the measurement setups are explained in this section.

Fourier Transform InfraRed Spectroscopy

FTIR measures the wavelength dependent absorption in the infrared part of the electromagnetic spectrum. This absorption is the result of excitation of overtones or harmonic vibrations in a material. The frequency ν of the absorbed radiation is given by the Bohr frequency condition:

$$\Delta E = h\nu \tag{3.1}$$

Where ΔE is difference between the energy states of a bond or group that vibrates within the material, and h is Planck's constant. Only vibrations with a transition dipole moment which is infrared active can be detected by FTIR. It is common practise to present the measured spectra as a function of the vacuum wavenumber, ω, expressed in reciprocal centimetres (cm^{-1}), as ω is the inverse of the wavelength (λ):

$$\omega = \frac{\nu}{c} = \frac{1}{\lambda} \tag{3.2}$$

The FTIR measurements are made on a-Si:H films deposited on c-Si wafer as explained in section 2.2.1. The FTIR spectra are measured with the Thermo Electron Nicolet 5700 Fourier Transform Infrared Spectroscope. The absorption bands in a-Si:H related to the resonant frequencies of the Si-H bending, wagging and stretching modes are measured with this setup. The wagging mode of all the bonded hydrogen in the film contributes to the absorption peak at $\omega \approx 630$ cm^{-1} [75]. Two stretching modes are present in the spectra. The low stretching mode (LSM) is found at $\omega \approx 2000$ cm^{-1} and the high stretching mode (HSM) at $\omega \approx 2100$ cm^{-1} [75]. These absorptions can be used to evaluate the hydrogen content c_{H}, and microstructure parameter R^* as is explained in section 2.2.1.

Raman Spectroscopy

In RS a shift in wavelength of light (photons) is measured after interaction with the material, this is called the Raman shift or the wave shift (ω). Raman shifts occurs when a photon scatters inelastically with lattice atoms or molecules [78]. The shift in wavelength corresponds to the energy difference between two resonant states of the material and is independent of the absolute energy of the photon. For vibrations to be Raman active a change in polarisability of the transition is required. The Raman active phonons in a-Si:H related to the Si-Si bonds are the transverse optical (TO) mode, detected at approximately 480 cm^{-1} Raman shift, the longitudinal optic (LO) mode at 400 cm^{-1}, the longitudinal acoustic (LA) mode at 300 cm^{-1}, and the transverse acoustic (TA) mode at around 130 cm^{-1} [79]. Several Si-H_x related vibrations are also visible in Raman spectrum of a-Si:H [75]. Both the LSM and HSM of the Si-H_x bonds can be detected [82] as well as the wagging and the rocking mode which are observed at approximately 630 cm^{-1} [79].

Raman spectra were measured with a Renishaw inVia Raman microscope using a 514 nm Ar laser and a 633 nm HeNe laser. The volume probed by RS is dependent on laser, spot size and the wavelength dependent absorption coefficient, α_λ, of the film [83]. The actual sensitivity of RS also depends on the cross section for the Raman scattering process σ_R, which in turn can be wavelength dependent [83]. Brodsky et al. observed that for Si-H_x related scattering there was little difference for lasers with phonon energies from 1.8-2.5 eV (689-496 nm), for the TO peak some difference has been observed [100]. The polarization ratios reported are $\rho = 0.2$ for the Si-H_x and $\rho = 0.55$ for the TO peak [104, 100]). The laser (or wavelength) dependent Raman collection depth (RCD) is directly related to the wavelength dependent absorption of the film. The collection depth can be estimated through [105]:

$$RCD = \frac{1}{2 \cdot \alpha_\lambda} \tag{3.3}$$

The α_λ of a-Si:H is approximately $1.2{\cdot}10^5$ cm^{-1} for $\lambda = 514$ nm and $2{\cdot}10^4$ cm^{-1} for $\lambda = 633$ nm [106]. These values result in a RCD of around 40 nm for green laser light ($\lambda = 514$ nm) and 250 nm for red laser light ($\lambda = 633$ nm). It should be noted that the returning (shifted) laser light will have a different wavelength from the light entering the film, making equation 3.3 a rough estimate of the RCD.

3.3 Results of a-Si:H characterisation

The results of the a-Si:H characterisation are presented in this section. As explained in section 3.2, FTIR and RS do not (necessarily) evaluate the same film volume of each a-Si:H sample, as the collection depth is dependent on the laser wavelength. For this reason the results of this section are depicted per technique and laser, rather than a direct comparison of the integrated intensities of the respective modes. This section first shows the hydrogen content, c_{H}, calculated from FTIR data as explained in section 2.2.1. The intensities of the stretching and wagging modes (I_{LSM}, I_{HSM} and I_{630}) determined from RS and FTIR spectra, as explained in sections 2.2.2 and 2.2.1 are compared. Next the RS shifts (ω) of the Si-H$_s$ RS modes are presented and compared to the FTIR wavenumbers (ω) of the Si-H absorptions.

3.3.1 Si-H modes detected by RS and FTIR

Figure 3.1 shows the results of the FTIR and RS detection of the Si-H rocking, wagging, and stretching modes in the ETPCVD deposited films. The first two plots evaluate the c_{H} from the stretching modes $c_{\mathrm{H,\,LSM}}$, $c_{\mathrm{H,\,HSM}}$ as a function of the $c_{\mathrm{H,\,630}}$, as determined by FTIR. No clear relation between the $c_{\mathrm{H,\,LSM}}$ and the $c_{\mathrm{H,\,630}}$ is observed in figure 3.1 (a). On the other hand, the $c_{\mathrm{H,\,HSM}}$ increases with $c_{\mathrm{H,\,630}}$ for the same samples (figure 3.1 (b)). For $c_{\mathrm{H,\,630}}$ values up to 17% this relation is linear. For values above 17% the $c_{\mathrm{H,\,HSM}}$ still increases with $c_{\mathrm{H,\,630}}$ although the relation is no longer linear.

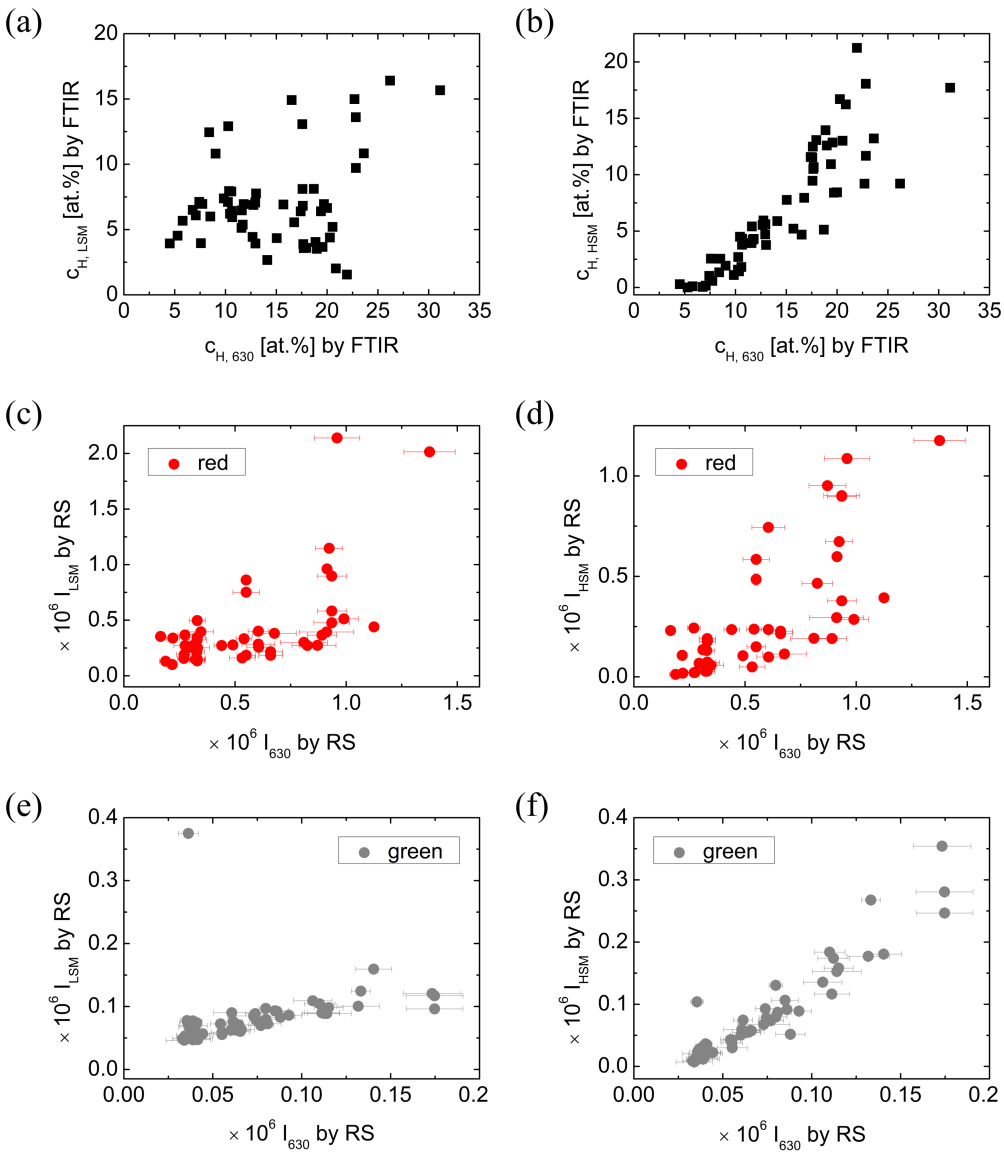


Figure 3.1. (a) The $c_{\mathrm{H,\,LSM}}$ and (b) the $c_{\mathrm{H,\,HSM}}$ as a function of $c_{\mathrm{H,\,630}}$, determined from the integrated intensities of the respective absorptions (FTIR) in the ETPCVD films deposited on c-Si wafer (the error bars are hidden in the markers). (c) Graphs of the I_{LSM} and (d) the I_{HSM} as a function of I_{630} of ETPCVD filmps deposited on glass. The integrated intensities are determined from the red laser RS spectra and (e), (f) from the green laser RS spectra.

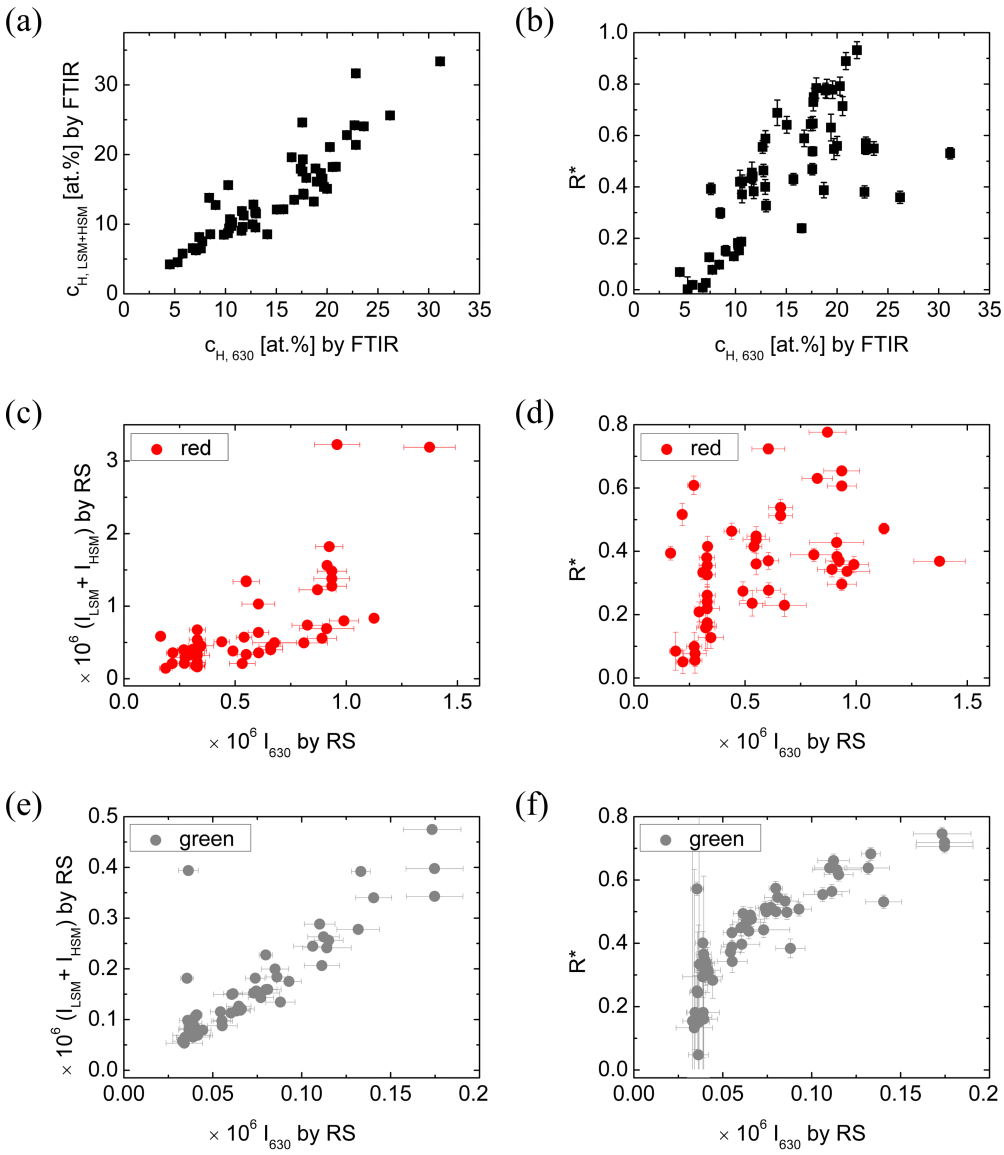


Figure 3.2. (a) The $c_{\mathrm{H,\ LSM+HSM}}$ and (b) the R^* results determined from the stretching modes in the FTIR spectra, as a function of $c_{\mathrm{H,\ 630}}$ of the ETPCVD films on c-Si. The red laser RS results of (c) $I_{\mathrm{LSM}} + I_{\mathrm{HSM}}$ and (d) R^*, as a function of the red laser RS I_{630} and (e) the green laser RS $I_{\mathrm{LSM}} + I_{\mathrm{HSM}}$ and (f) R^* as a function of the green laser RS I_{630}. RS is measured on ETPCVD films deposited on glass.

The RS measurements of the stretching modes, using the red laser, show some increase of the I_{LSM} and the I_{HSM} with I_{630} (figure 3.1 (c, d)). The green laser RS measurements (figure 3.1 (e, f)) show a strong linear relation between both the I_{LSM} and the I_{HSM} with the I_{630}.

Figure 3.2 shows the low and high stretching modes of the ETPCVD deposited samples in two ways. First, graphs 3.2 (a), (c) and (e) show the superposition of the stretching modes, with respect to the I_{630} or $c_{\mathrm{H,630}}$, for FTIR and RS measurements respectively. Second, graphs 3.2 (b), (d) and (f) show the R^*, calculated according to equation 2.3, with respect to the I_{630} or $c_{\mathrm{H,630}}$. The values determined from the FTIR measurements (figure 3.2 (a, b)) serve as a reference for the comparison. Figure 3.2 (a) shows that the c_{H} from the stretching modes is similar to the $c_{\mathrm{H,630}}$ determined from the $I_{\mathrm{LSM+HSM}}$ rocking, wagging mode. All graphs in figure 3.2 show an increase of both the combined stretching modes ($I_{\mathrm{LSM}} + I_{\mathrm{HSM}}$) and R^* with increasing I_{630} or $c_{\mathrm{H,630}}$. The stretching modes and the R^* determined with the red laser increase with I_{630} although no clear relation is visible (3.2 (c) and (d)). The green laser $I_{\mathrm{LSM}} + I_{\mathrm{HSM}}$ shows a linear increase with respect to the I_{630} (3.2 (e)). This is similar to the relation observed by FTIR ((3.2 (a)). The R^* determined from the green laser measurements increases with increasing I_{630}. The relation appears to be linear for I_{630} values above 0.04×10^6. The graphs in figure 3.2 show that the red and green laser measurements of R^* and I_{630} do not match the FTIR R^*, $c_{\mathrm{H,630}}$ relation.

For the R^* evaluation, the samples are presented by the $c_{\mathrm{H,\,630}}$ values of the films deposited on c-Si. Figure 3.3 shows the direct comparison of the R^* determined by (i) FTIR, (ii) RS using the green laser, and (iii) RS using the red laser. The values of R^* determined by FTIR show a larger variation than the R^*_{RS} values do. The R^*_{RS} is determined using equation 2.3, by simply replacing the I_{LSM} and I_{HSM} from FTIR by those measured by RS. The R^*_{RS} can be linearly scaled to (ap-

proximately) match the R^* values calculated from FTIR measurements using the following equation:

$$R^* = R_0^* + A \times R_{RS}^* \tag{3.4}$$

For both lasers the scaling factors have been determined, the results are shown in table 3.1. The resulting linear relations are depicted in figure 3.3 (b). The grey line shows the results for the green laser, the red line shows the results for the red laser. The R^*_{RSred} and R^*_{RSgreen} show a similar increase with increasing R^*_{FTIR}.

Table 3.1. Overview of parameter values for the R^* equation (3.4) for green and red laser RS measurements.

	R_0^*	A
RS green	0.220 ± 0.031	0.524 ± 0.051
RS red	0.208 ± 0.071	0.444 ± 0.114

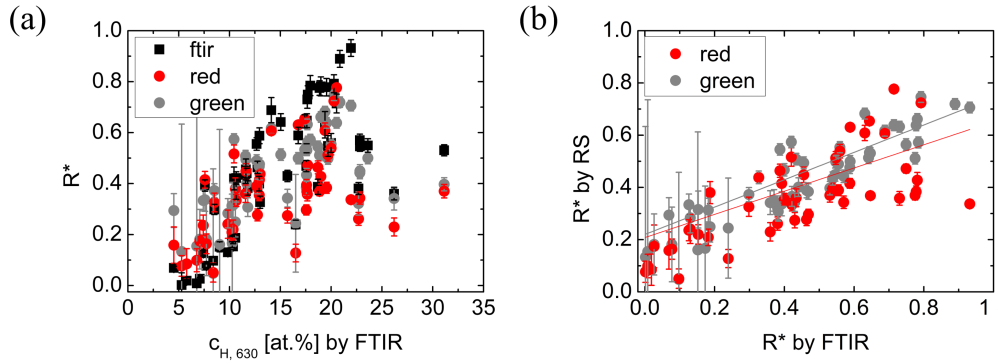


Figure 3.3. (a) The R^* measured by FTIR and RS as a function of the $c_{\mathrm{H,\,630}}$ determined by FTIR. (b) The relation between the R^* determined from RS measurements and the R^* from FTIR, the red line indicates the linear fit of the red laser RS data, the grey line of the green laser RS data.

3.3.2 Positions of Raman shift and absorption frequencies of Si-H$_x$ related features

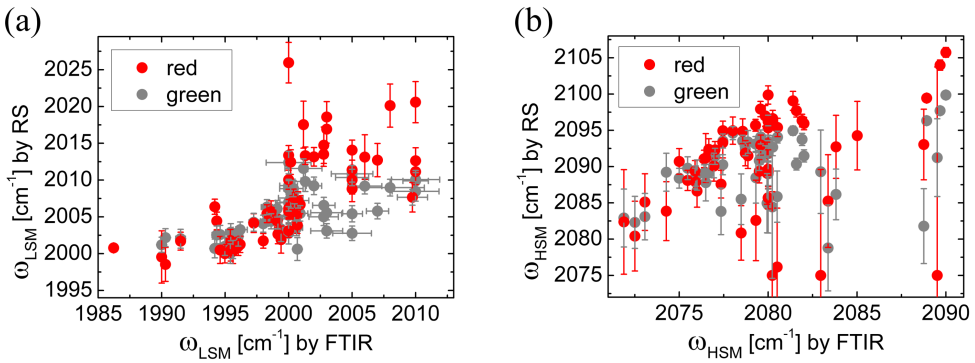


Figure 3.4. (a) Centre of the LSM Raman shift distribution, ω_{LSM}, from RS spectra as a function of the LSM absorption frequency, ω_{LSM}, measured by FTIR. (b) Centre of the HSM Raman shift distribution, ω_{HSM}, as a function of the frequency position, ω_{HSM}, measured by FTIR.

The Raman shifts and the frequency positions of the LSM (ω_{LSM}) and HSM (ω_{HSM}) in the RS and FTIR spectra are shown in figure 3.4. The spread in range of the ω_{LSM} is larger for the red than the green laser Raman shift. The RS values are approximately 10 cm^{-1} higher than those of FTIR. With increasing values of ω_{LSM} by FTIR, the ω_{LSM} by RS increases non-linearly. For values of ω_{LSM} (FTIR) larger than 2000 cm^{-1} the increase is stronger for the red laser ω_{LSM} than for the green laser values.

The ω_{HSM} values of the RS spectra are also approximately 10 cm^{-1} higher than the ω_{HSM} from the FTIR measurements. The bulk of the ω_{HSM} measurements by RS follow a (nearly) linear relation with the FTIR data. The FTIR measurements show a gap in the ω_{HSM} data around 2087 cm^{-1}, prompting an investigation of the existence of a middle stretching mode (MSM) [97]. Multiple samples have been evaluated, and the MSM is absent in these samples.

Both the ω_{LSM} and ω_{HSM} data have been fitted as linear relations. These relations are quantified using equation 3.5, where the ω_{SM} is the FTIR value, and $\omega_{\mathrm{SM,\ RS}}$ is the RS value:

$$\omega_{\mathrm{SM}} = \omega_0 + C \times \omega_{\mathrm{SM,\ RS}} \tag{3.5}$$

The equation constants ω_0 and C for the $\omega_{\mathrm{SM,\ FTIR}}$ are presented in table 3.2.

Table 3.2. Overview of parameter values for the $\omega_{\mathrm{SM's}}$ relations between FTIR and RS, for values below 2000 cm^{-1} (ω_{LSM} by FTIR) and below 2079.5 cm^{-1} (ω_{HSM} by FTIR) for green and red laser RS measurements.

	$\omega_{LSM,0}$	C_{LSM}	$\omega_{HSM,0}$	C_{HSM}
RS green	-94 ± 579	1.04 ± 0.29	1227 ± 186	0.406 ± 0.089
RS red	448 ± 645	0.77 ± 0.32	1576 ± 167	0.239 ± 0.080

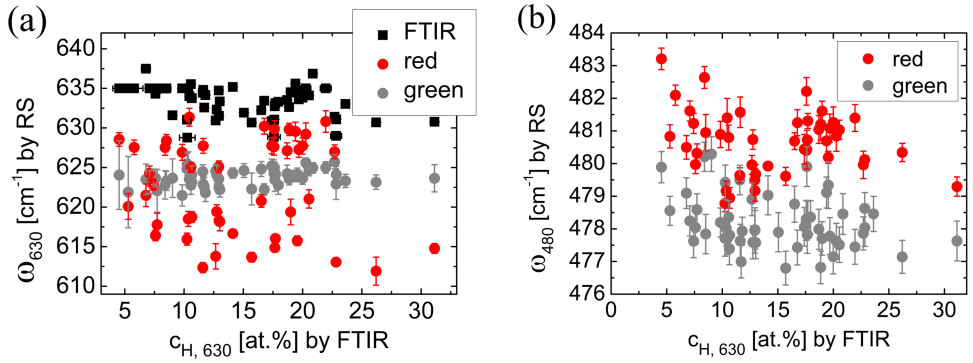


Figure 3.5. (a) Raman shift and FTIR absorption frequency ω_{630} as a function of the $c_{\mathrm{H,\ 630}}$ measured by FTIR. (b) Raman shift ω_{480} as a function of the $c_{\mathrm{H,\ 630}}$ measured by FTIR.

To compare the 630 cm^{-1} mode detection by RS with FTIR, figure 3.5 (a) shows the ω_{630} with respect to the $c_{\mathrm{H,\ 630}}$. A slight decrease in ω_{630} is observed in the FTIR measurements with increasing $c_{\mathrm{H,\ 630}}$. This decrease is not present for the green laser RS measurement of ω_{630}. The scattering between the data points from the red laser RS

measurements is much larger than on the other measurements. As this could be a result of the a-Si:H structure in the bulk of the films, the transverse optical mode of the Si-Si bonds at 480 cm^1 was examined (see figure 3.5 (b)). No difference, other than an offset in ω_{480} between the red and green laser measurements is observed. This observation does confirm, nor exclude the influence of the a-Si:H structure in the bulk of the films on the red laser ω_{630} values.

3.4 Discussion on characterization of a-Si:H

The previous section shows the results concerning three topics (i) the comparison of Si-H_x absorptions measured by FTIR with the detection of the Si-H_x related modes by RS (ii) the comparison of R^* values determined from FTIR and RS measurements and (iii) a comparison between the frequency positions of Raman shift and the FTIR absorption wave number of the Si-H_x related features. These comparisons were made to determine to what extent the RS measurements are supplementary to the FTIR measurements and in which cases they are redundant. The determination of the microstructure R^*, and the frequency positions requires the following:

- relations between the RS and FTIR results concerning the I_{630}, I_{LSM}, I_{HSM},
- the R^* ratio itself,
- the $\omega_{\mathrm{SM's}}$ and ω_{630}.

This section will first discuss the determination of the $c_{\mathrm{H,\ 630}}$ by RS with respect to FTIR, followed by the comparison of the R^* values from RS and FTIR and finally the relation between Raman shifts and the absorption wave number is evaluated.

Evaluation of the Si-H_x stretching modes and R^* by RS

The results of the Si-H_x stretching modes are presented in figures 3.1 and 3.2. The RS determined I_{LMS} and I_{HMS} are presented with respect to the RS determined Si-H_x wagging mode I_{630}. The relation between the $I_{\mathrm{SM's}}$ and the I_{630} measured with the green laser is strong. The FTIR measurement does not show a clear increase in I_{LSM} with I_{630}, but it does for I_{HSM} and $I_{\mathrm{LSM}} + I_{\mathrm{HSM}}$ with the I_{630}. The FTIR measurements probe both the top and the bulk of the films. The differences between the red and green laser RS data can both be seen in the FTIR measurements. The most likely explanation is that the green laser RS is more sensitive to the film surface and the red laser to the bulk of the films, although a direct evaluation of the influence of film thickness was inconclusive. The measurement results of the red laser RS and the FTIR show film structure closer to the substrate. In addition some influence of the glass substrate itself may be present in the red laser RS spectra in addition to the a-Si:H structure at the glass interface.

The difference in RCD between the two stretching modes, LSM and HSM, themselves is limited. As such the determination of R^* by RS is possible and the use of the green and red laser allows for more detailed studies of the film structure perpendicular to the film surface. This is reflected in the figure 3.3 and table 3.1. From the relation described by equation 3.4 it is clear that the RS values of R^* yield slightly different results. This is most likely due some difference to the sensitivity to Raman scattering of the LSM and HSM. This means that the R^* determined by RS is indeed a figure of merit for the microstructure of a-Si:H but the value is not interchangeable with the R^* determined by FTIR.

Relation of the wave number ω in FTIR with the wave shift ω in RS

As explained in the introduction of this chapter, information about the structure a-Si:H can be deduced from FTIR measurements. The wave numbers at which the absorption of Si-H_x vibrations are observed

by FTIR depend on the dielectric screening of these bonds by the surrounding matrix material [34]. The wave numbers ω_{LSM} and ω_{HSM} combined with the c_{H} are used to determine the nano structure parameter K. As explained the c_{H} is not accurately determined from RS measurements. However, the values of the hydrogen related wave numbers ω and the Raman shifts ω can still give insight into the material structure, especially if variations in structure perpendicular to the film surface can be detected.

The wave number of the rocking wagging Si-H_x mode ω_{630} of the green laser RS and the FTIR measurements are approximately constant with c_{H}. The FTIR value of ω_{630} is approximately 10 cm^{-1} higher, which is likely due TO phonon mode detected by RS, which influences the ω_{630} value in RS. The effect is not observed for the red laser RS measurements. The scattering on the ω_{630} values is quite large. This effect could be related to the influence of the substrate.

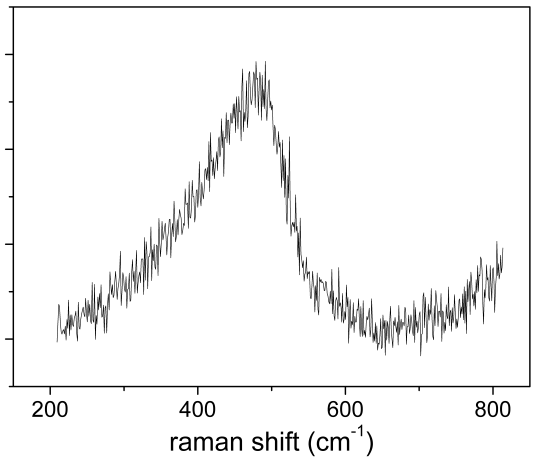


Figure 3.6. Raman spectrum of bare corning glass substrate.

Figure 3.6 shows the red laser RS spectrum for the glass substrate. A strong asymmetric feature near 500 cm^{-1} with a slight shoulder at 600 cm^{-1} is present. When examining the spread in both the ω_{630} and ω_{LSM} of the red laser RS measurements: both are larger than for the green laser measurements. In addition the red laser TO (ω_{480}) does not

differ in spread from the green laser measurements. This observation makes it likely that the spread in the red laser ω_{630} is due to the material structure in the bulk of the films.

The ω_{LSM} and ω_{HSM} for values up to 2000 cm^{-1} and 2080 cm^{-1} are rather similar. For higher ω_{LSM} the green and red laser measurements deviate. Like the determination of R^*, the values of ω_{LSM} and ω_{HSM} can be determined by RS. It should be noted that the values measured by RS are somewhat higher than those measured by FTIR. This difference could be due to differences in screening of the dipole for RS scattering compared to IR absorption.

3.5 Conclusions

This chapter compares the detection of hydrogen and hydrogen bonding configurations by Raman Spectroscopy with this detection by Fourier Transform InfraRed spectroscopy. Due to variation in collection depth of the RS signals, the determination of the c_{H} cannot accurately be achieved using RS for these films. The Si-H_x wagging and stretching modes can be detected by both techniques and is strongly related to the rocking-wagging mode detected by RS for both lasers. The wavenumber of wagging mode is well defined for the green laser RS spectra, but less so for the red laser spectra. This effect is also observed for the ω_{LSM} measurement by red laser RS and is likely due to the material structure in the bulk of the films. The RS measurements of the Si-H_x related features can be used to evaluate the ω_{LSM} and ω_{HSM} as well as the microstructure parameter R^*. The sensitivity to the low and high stretching modes are not the same for the FTIR and RS measurements so the R^* and $\omega_{\text{LSM,HSM}}$ must be rescaled for a comparison between both techniques.

Chapter 4

Deposition of B doped a-Si(:H) films by ETPCVD

4.1 Introduction

Producing solar cells from amorphous Si through SPC requires doped films with a thickness of up to 10 micrometer. We use Expanding Thermal Plasma Chemical Vapour Deposition (ETPCVD) as a deposition method for the high deposition rates that can be achieved by this technique, as is discussed in section 2.1.2. Solar cells require doped layers and ideally doping atoms are incorporated during the deposition of the Si films to minimise the number of production steps. Prior to this study, ETPCVD was used only for intrinsic a-Si:H and other materials such as SiN_x [39, 71, 70]. In this chapter we discuss the first boron doped hydrogenated amorphous silicon films (B-doped a-Si:H) produced by ETPCVD.

In order to investigate the B-doped a-Si:H films made by ETPCVD, a comparison of these films is made with B-doped a-Si:H films deposited by Plasma Enhanced Chemical Vapour Deposition (PECVD).

The application of a-Si:H films in semiconductor devices such as solar cells require n-type and p-type doping. Doped a-Si:H were first reported by Chittick et al. [107]. Müller [108] generalized the doping mechanism theories of both Street [109] and Robertson [110] in 1986. The generalization follows the concept that the position of the Fermi level and the constraints imposed by the $8 - N$ rule determine the defect structure (where N is the number of valence electrons). An increase in the relative concentration of microvoids was observed with the increase of doping by B_2H_6 [111] for PECVD deposited films. This relates the doping to the defect structure in the material. As ETPCVD allows for a broad range of microstructures and has different film surface conditions during growth than PECVD depositions this chapter makes a comparison between the B-doped a-Si:H films produced by both techniques.

In this chapter the results of a study are presented on the properties of boron doped a-Si:H deposited by ETPCVD. Particular focus is dedicated to the boron concentration, determined by measuring the carrier concentration of crystallized boron doped a-Si:H films.

4.2 Experimental details

4.2.1 Deposition techniques

As mentioned in the introduction, two techniques are used to deposit the samples studied in this chapter. The depositions made by Radio Frequency Plasma Enhanced Chemical Vapour Deposition (RF-PECVD, or PECVD) are used as reference material, because PECVD is an established deposition technique for B-doped a-Si:H films both in laboratories and industry. PECVD is a direct plasma technique

commonly used for laboratory and industrial deposition of a-Si:H. The PECVD setup used in this chapter is a parallel plate rf configuration. The substrates are placed top down between the electrodes and preheated using an electric heater. The grounded electrode has an area of 12 cm × 12 cm and the distance between the electrodes is 10 mm for depositions of intrinsic a-Si:H and 11 mm for doped a-Si:H. Doped films are made in the chamber designated for p-type depositions. All precursor gasses (SiH_4 and 2% B_2H_6 diluted in H_2) are injected and dissociated with the aid of a plasma. The plasma is created using an RF generator. The substrate is placed on the grounded electrode and thereby exposed to ion bombardment. The deposition temperature is set to either 180 °C or 325 °C for the different sample series. The B_2H_6-to-SiH_4 ratio has been varied from 0.2 to 1.0 × 10^{-3} within each series.

The second deposition technique for this chapter is the ETPCVD. It is important to note here that ETPCVD in contrast to PECVD is a remote plasma technique. This technique is explained in chapter 3 for the deposition of intrinsic a-Si:H films. To deposit B-doped a-Si:H films the setup has been altered by injecting a mixture of 2% B_2H_6 in H_2 at the exit of the channel into the plasma. During deposition of intrinsic films, only H_2 is added to the plasma. The deposition temperature was set to 180 °C, 325 °C and for some samples to 350 °C. The chamber pressure varied from 8.1 to 8.5 Pa. The B_2H_6-to-SiH_4 ratio has been varied from 0.0 to 0.8 × 10^{-3} within each series.

4.2.2 Sample preparation and characterisation techniques

The samples have been deposited on two types of substrates: glass and Al_2O_3. Before deposition the glass (Corning glass type GX) is cleaned by etching in a solution of HF, HNO_3, CH_3COOH, and H_2O. The layers deposited on Al_2O_3 substrate have been used specifically for the Neutron Depth Profiling (NDP) measurements, and is required

in order to exclude (or quantify) the influence of the B in the glass on the measurement results. The NDP measurement is used to determine the B concentration of specific samples. The as-deposited samples on glass are measured with Raman spectroscopy (RS) to evaluate the a-Si:H microstructure R^*. The optical transmission and reflection are measured to determine the optical bandgap (E_g) and the film thickness. I-V measurements were made to determine the dark conductivity and activation energy of the films. The concentration of B atoms is determined by crystallising the a-Si:H films on glass by annealing them for 16 h at 600 °C in an Ar atmosphere. Subsequently, Hall measurements have been carried out on the poly Si films to determine the carrier concentration. The carrier concentration is used as a measure for the B concentration. More details on the determination of the B content from the carrier concentration can be found at the end of this section.

Raman Spectroscopy
The microstructure parameter R^* is determined from the low and high Si-H_x stretching mode, as described in chapter 3. For the R^* determination the range from 1700-2300 cm^{-1} is used. After annealing of the a-Si:H films on glass, the RS spectra are determined to confirm that the films are fully crystalline. For the evaluation of crystalline fraction, the range from 300-600 cm^{-1} is used; the absence of the a-Si:H transverse optical (TO) mode at 480 cm^{-1} is used to determine that the films are fully crystalline. Details on the determination of the crystalline fraction can be found in section 2.2.2.

Optical transmission and reflection
The transmission and reflection of the films on glass substrates are measured using a Theiss RT setup for wavelengths ranging from 375 nm to 1060 nm. From these measurements the complex refractive index ($\tilde{n} = n + ik$) obtained. The cubic bandgap is determined from the optical constants according to Klazes method [96]. Details can be found in section 2.3.1.

Neutron Depth Profiling and validation of the measurement of the B concentration

The atomic B concentration of several films is determined by Neutron Depth Profiling (NDP) [112]. NDP is a quantitative determination of composition. The sample volume is uniformly exposed to low energy neutrons. Upon the absorption of a neutron certain nuclides react by isotropic emission of alpha particles or protons and the diametrically emitted recoil nucleus. The $^{10}B(n,\alpha)^{7}Li$ reaction can produce one of two possible particle pairs: a 1776-keV alpha and its 1014-keV recoil ^{7}Li nucleus, or a 1472-keV alpha and its 840-keV recoil ^{7}Li nucleus [113]. All four of these particles are visible in the NDP spectrum. Each particle generates an independent and redundant profile of the B distribution in the film. The 1472-keV particle has the highest yield and is used to identify the B content of the films. For this measurement films were deposited both on glass and on Al_2O_3. There are two reasons for this. First, the measurement sensitivity to the B in the glass, which can obscure the NDP measurement. The second reason is the evaluation of the effects of substrate on the measurement, such as enhanced doping of the films by the glass substrates.

The principle of the B content determination in this chapter is based on the assumption that all B atom become active dopants in the crystallized Si films. Using Hall measurements the number of active dopants can be evaluated through the carrier concentration (section 2.3.3). Multiple assumptions are made in this method of B content evaluation. To qualitatively establish this method NDP measurements are made to validate the underlying assumptions.

The relationship between the carrier concentration and the B content in the as-deposited films is established by measuring the B content of the as-deposited films on glass by NDP and comparing these results to the carrier concentration calculated from the Hall measurements. As the glass substrate contains boron, additional films are made on B free substrates, Al_2O_3, to ensure that the NDP measurements are not influenced by the B content of the substrate material. It was not possible to make suitable poly-Si samples from the films on Al_2O_3 for the Hall measurements. The samples on Al_2O_3 have been deposited as part of a specific deposition series. The results of the NDP measurements on

Al_2O_3 samples (that will be presented in section 4.3) have been compared to carrier concentration data obtained from Hall measurements on poly-Si samples on glass produced in the same deposition series.

4.3 Results

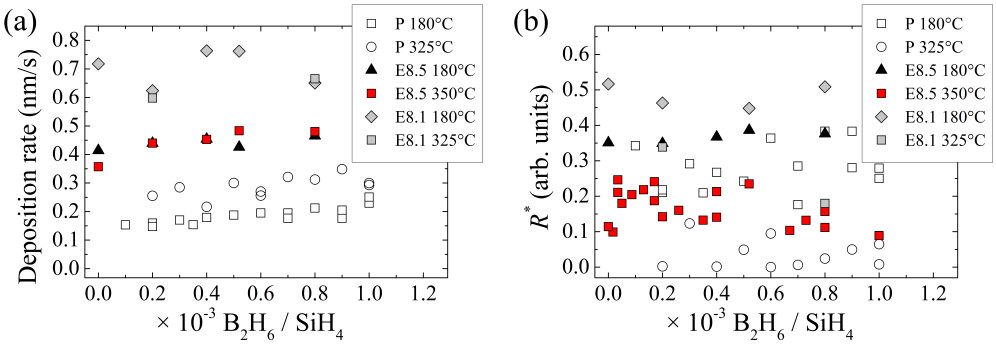


Figure 4.1. The (a) deposition rate and (b) R^* of the boron doped a-Si:H films as a function of the B_2H_6-to-SiH_4 ratio, deposited by PECVD (P) and ETPCVD (E) at different deposition pressures (8.1 and 8.5 Pa) and temperatures.

In figure 4.1 (a) the deposition rates are shown as a function of the B_2H_6 / SiH_4 gas-flow ratio. The deposition rate of PECVD material deposited at 180 °C increases from about 0.15 nm/s to 0.25 nm/s with increasing B_2H_6 flow, whereas at 325 °C this rate increases from 0.25 to 0.35 nm/s. For samples deposited using ETPCVD we observe more scattering, although the data suggest some increase of the deposition rate with increasing B_2H_6 fraction. The deposition temperature does not seem to influence the deposition rate very strongly. A small increase of the deposition pressure results in a reduction of the deposition rate, in contrast to what has been reported for ETPCVD of intrinsic a-Si:H [69]. Figure 4.1 (b) shows the variation of R^* obtained from the RS spectra as a function of the B_2H_6 / SiH_4 ratio. The results show that the low temperature depositions by both ETPCVD and PECVD result in high R^* values (see figure 4.1 (b)). The low temperature depositions

show a large difference in R^* between the two deposition techniques, with a larger R^* for low temperature ETPCVD depositions. A larger R^* was also observed for intrinsic ETPCVD films compared to PECVD films [73].

The cubic bandgap, E_g, (determined from RT measurements) and the activation energy, E_a, of the dark conductivity are presented as a function of the B_2H_6 / SiH_4 gas-flow ratio in figure 4.2 (a) and (b), respectively. A direct comparison of the E_a and E_g (see figure 4.2 (c)) shows a strong relation between the E_a and E_g. This indicates that the difference between the deposition series observed in 4.2 (a) and (b) are due to differences in the (active) B content of the films and possibly the hydrogen content.

As explained in the experimental section, the B content is determined directly by NDP and indirectly from the carrier concentration of the poly-Si films. The carrier concentration of the poly-Si films as a function of the B_2H_6-to-SiH_4 ratio is shown in figure 4.3 (b). All but one deposition sets show an increase of the B content determined by NDP with increasing B_2H_6-to-SiH_4 ratio. Both measurement procedures show that the B content of the PECVD films, deposited at 180 °C, for a given B_2H_6-to-SiH_4 ratio is higher than of the other deposition series.

The NDP measurements were made to validate the carrier concentration in the poly-Si films as a measure for the B content in the as-deposited films. Figure 4.4 shows the relation between the B content determined by both methods. As explained earlier, two different substrates were used. The B content obtained from the carrier concentration, shows lower absolute values than when determined by NDP. The two methods show a linear relation for the B content. The differences due to the use of different substrates seem negligible. This results in the following empirical equation to determine the B-content (C_B) from the carrier concentration (C_C):

$$C_B = 2.474 \times C_C \tag{4.1}$$

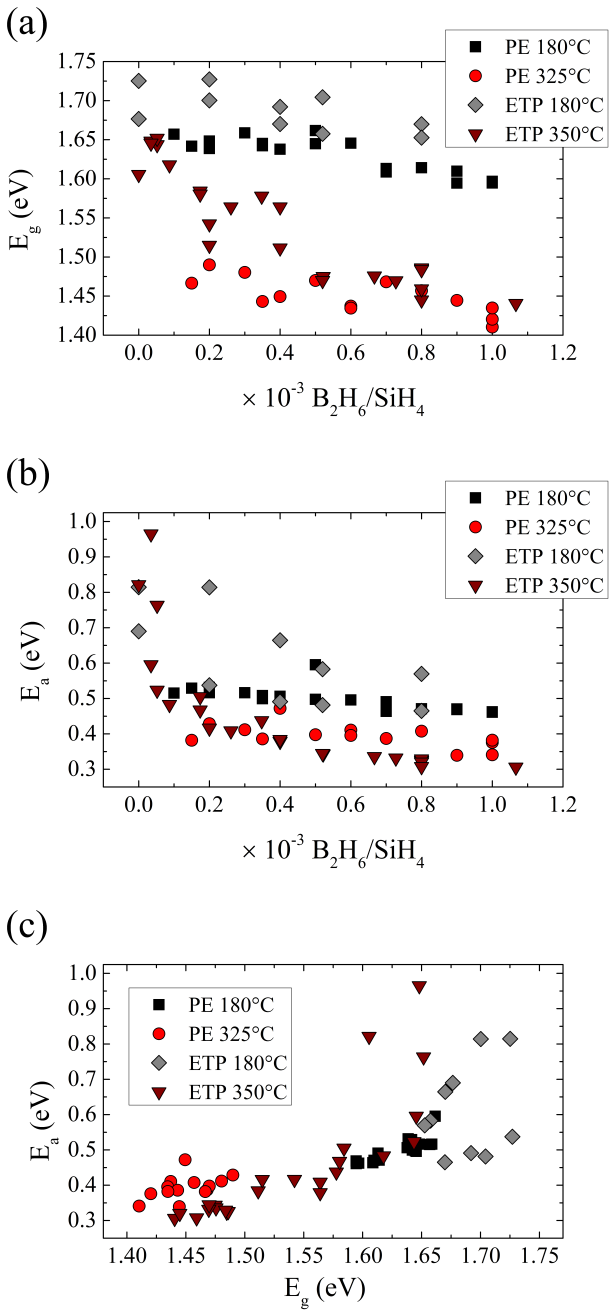


Figure 4.2. The (a) E_g, (b) E_a for boron doped films as a function of the B_2H_6-to-SiH_4 ratio, deposited by PECVD and ETPCVD. (c) The E_g as function of the E_a, which appears to be linear up to an activation energy of approximately 0.55 eV.

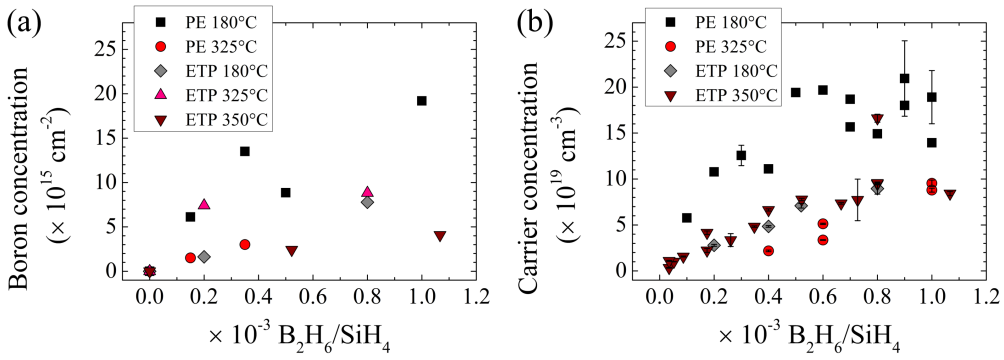


Figure 4.3. (a) The B content determined by NDP as a function of the B_2H_6-to-SiH_4 ratio, deposited by PECVD and ETPCVD. All but one deposition sets show an increase with B content with increasing B_2H_6-to-SiH_4 ratio. (b) The carrier concentration of the poly-Si films as a function of the B_2H_6-to-SiH_4 ratio, deposited by PECVD and ETPCVD. All but one deposition sets show an increase with B content with increasing B_2H_6-to-SiH_4 ratio.

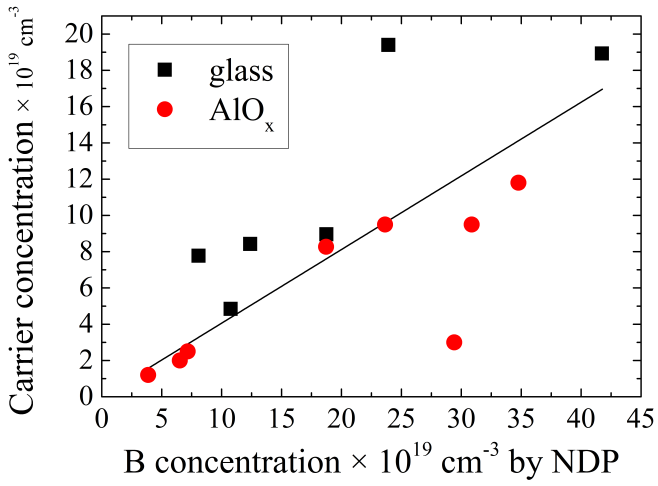


Figure 4.4. The carrier concentration of the poly-Si films as a function of the B content determined by NDP. The black line indicates the linear fit result of the carrier concentration as a function of the B density content.

After establishing that the carrier concentration in the poly-Si films is a reasonable measure for the B content of the as-deposited films the E_a and E_g are presented as a function of the B content as determined from the carrier concentration of crystallized films.

Figure 4.5 shows the deposition rate (a) and the R^* (b) as a function of the B content of the films. The deposition rate shows no dependence on the B content. The R^* values of the ETPCVD350 °C series decrease with increasing B content, in the other series this trend is absent.

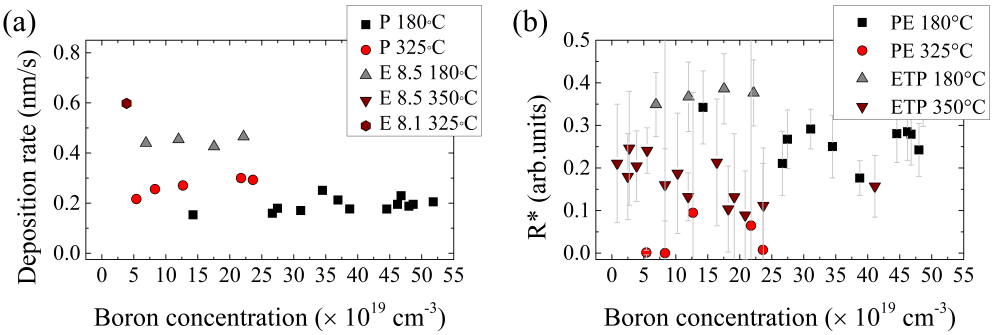


Figure 4.5. The (a) deposition rate and (b) R^* of the B doped a-Si:H films on glass as a function of the B content (determined from the carrier concentration in the poly-Si films).

The E_a values of all deposition series show a decrease with increasing B content, see figure 4.6 (b). The B-content in the PECVD films deposited at 180 °C is higher than the other series. The decrease of E_a with B content is less pronounced in this deposition series. This could indicate that the doping efficiency of these films is lower, or that the doping is approaching saturation. Other depositions series show similar values and dependence on the B content. The E_g values decrease with increasing B content. The low temperature depositions have larger E_g's than the high temperature depositions. The difference between the E_g values of deposition series are most likely due to the hydrogen content of the films, as lower deposition temperature result in higher hydrogen contents. ETPCVD films deposited at high temperature typically

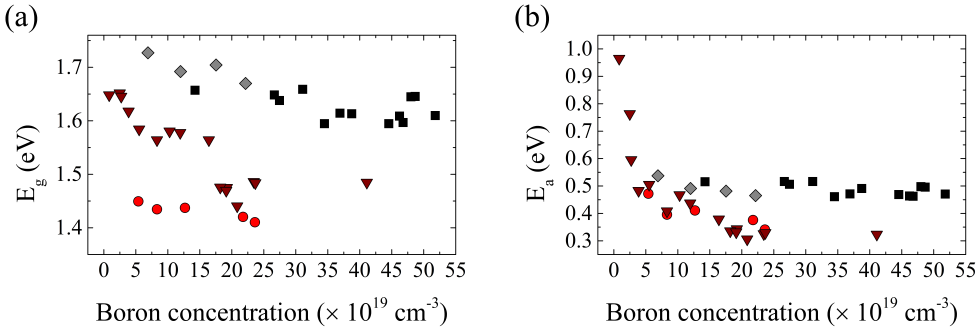


Figure 4.6. The (a) cubic bandgap and (b) the activation energy of conductivity of the B doped a-Si:H films on glass as a function of the B content (determined from the carrier concentration in the poly-Si films).

have higher hydrogen content that PECVD films deposited at the same temperature.

4.4 Discussion

A comparison is made between the B content of a-Si:H films produced by ETPCVD and by PECVD, using neutron depth profiling and the carrier concentration of the crystallised films. We found a strong correlation between the B concentration obtained from the NDP measurements and that derived from measurement of the carrier concentration on poly-Si. The B content for both deposition techniques increases with increasing B_2H_6-to-SiH_4 ratio. By comparing the NDP and carrier concentration measurements (see figure 4.4) we have determined that approximately 40% of the B atoms are active as dopants in the crystallised films. Based on the measurements by NDP and of the carrier concentration, the carrier concentration can be used to evaluate the B content of the as deposited films.

The results, figure 4.3, show that the PECVD samples deposited at lower temperatures (180 °C) have the highest B content: 19×10^{15} cm^{-2} for a B_2H_6-to-SiH_4 ratio of 1×10^{-3} (figure 4.3 (a)). This is approximately twice the B content of the PECVD films deposited at 325 °C

with a similar gas flow ratio. The B content for the films deposited by ETPCVD at 180 °C and at 325 °C is approximately 8.5×10^{15} cm^{-2} for a B_2H_6-to-SiH_4 ratio of 0.8×10^{-3}. The important difference between ETPCVD and PECVD films is the temperature dependence of the B content. The B content of the PECVD deposited films reduces with increasing deposition temperature, while the B content of the ETPCVD deposited films is not affected by the substrate temperature. A possible explanation is that the indirect plasma of the ETPCVD depositions is not affected, while the PECVD plasma chemistry is affected by the substrate temperature. The decomposition of B_2H_6 is temperature dependent [114]. B_2H_6 is exposed to the direct plasma during PECVD, and this plasma is in direct contact with the substrate. It appears that the high temperature PECVD plasma results in a similar decomposition of B_2H_6 as the remote expanding thermal plasma used in ETPCVD.

The opto-electrical properties of the films show a dependence on the B_2H_6-to-SiH_4 ratio. This dependence is directly linked to the density of B atoms incorporated into the films. The B content can be determined from the carrier concenration of the crystallised films according to equation 4.1 (figure 4.2). The E_g as well as the E_a decrease with increasing B content (figure 4.5). The slope (c_{Eg}) of the E_g, as a function of B content is similar for the PECVD180 °C and PECVD325 °C series. The ETPCVD series show a stronger decrease in E_g with increasing B content, in particular the ETPCVD350 °C series. The influence of the B content on the E_g can be quantified by:

$$E_g = E_{g0} - c_{E_g} \times C_B \tag{4.2}$$

with E_{g0}, the E_g for intrinsic films, we find the values for c_{E_g}. The data are presented in figure 4.4(b) and in table 4.1.

The ETPCVD350 °C series shows a decrease in R^* with increasing B content. Nasu et al. [111] only observed an increase in void density in B-doped films when compared to intrinsic films, but did not detect an increase in void density with increasing B content. Our finding indicates that the incorporation of H in the ETPCVD350 °C series is likely to change with the B content. Hydrogen is known to influence the E_g of a-

Table 4.1. Values of $R^*_{average}$ (determined from RS spectra), E_{g_0}, and c_{E_g} determined from figure 4.4(a) and (b).

	$T_{deposition}$	$R^*_{RS_{average}}$	E_{g_0} [eV]	c_{E_g} [eV·10^{-19} cm^3]
PE	180 °C	0.289 ± 0.064	1.6682 ± 0.0225	0.0011 ± 0.0006
PE	325 °C	0.034 ± 0.034	1.4561 ± 0.0054	0.0018 ± 0.0003
ETP	180 °C	0.370 ± 0.016	1.7430 ± 0.0214	0.0030 ± 0.0014
ETP	350 °C	0.167 ± 0.051	1.6273 ± 0.0018	0.0056 ± 0.0010

Table 4.2. Values of $C_{H,HSM}$ estimated from E_{g_0} and figure 4.7, $R^*_{0,RS}$ assumed to be $R^*_{R_{average}}$ for PECVD180 °C, PECVD325 °C, and ETPCVD180 °C and extrapolated for ETPCVD350 °C, $R^*_{0,FTIR}$ determined from $R^*_{0,RS}$ and equation 3.4.

	$T_{deposition}$	$C_{H,HSM}$	$R^*_{0,RS}$	$R^*_{0,FTIR}$
PE	180 °C	11 at.%	0.289	0.371
PE	325 °C	$<$ 5 at.%	0.034	0.239
ETP	180 °C	16 at.%	0.370	0.414
ETP	350 °C	8 at.%	0.205	0.327

Si:H films deposited by ETPCVD and PECVD. Smets et al. [48] showed that the E_g depends on the HSM bonded hydrogen content determined from FTIR measurements ($C_{H,HSM}$), see figure 4.7 (a). We use this bandgap dependence to find the hydrogen content in our layers.

From the E_{g_0} values the $C_{H,HSM}$ are estimated and presented in table 4.2. Considering the values of $R^*_{0,FTIR}$, the $C_{H,HSM}$ estimates are high, but reasonable for these deposition techniques and deposition temperatures.

If we assume that the $C_{H,HSM}$ of the PECVD series is not influenced by the B content (as the R^* is not affected by the B content), and that the influence of the B content on the E_g is similar for ETPCVD and PECVD material, we can reconstruct the change in E_g due to the $C_{H,HSM}$ for the ETPCVD series. For the ETPCVD350 °C series this would mean that samples with a B content around 25 × 10^{19} cm^{-3} would have a E_{g_0} of approximately 1.6 eV and an $C_{H,HSM}$ of $<$ 6%. These values are reasonable for ETPCVD films deposited at 350 °C.

If we assume that the total hydrogen content is not affected by the B-content, the reduction of $C_{H,HSM}$ would result in an R^*_{FTIR} of 0.267, or an R^*_{RS} of 0.090, this matches the results in figure 4.5 reasonably well.

Clearly, the influence of H in combination with B in a-Si:H films deposited by ETPCVD requires additional investigation. In particular the influence of the total hydrogen content and $C_{H,HSM}$ on the E_g for doped films should be examined. Based on the finding presented in this chapter it is clear that both B and H influence the E_g of the ETPCVD deposited films. The E_g increases with increasing $C_{H,HSM}$ and decreases with increasing B-content, see figure 4.7 (b). Based on the E_{g_0} and R^* values, the PECVD325 °C film structure is divacancy dominated while the other films are void dominated. As the R^* values for the ETPCVD350 °C decrease with increasing B-content, the film structure might be increasingly divacancy dominated. This is well explained when taking into account that B decreases the activation energy for H effusion, thus allowing effusion to occur at lower temperatures [4].

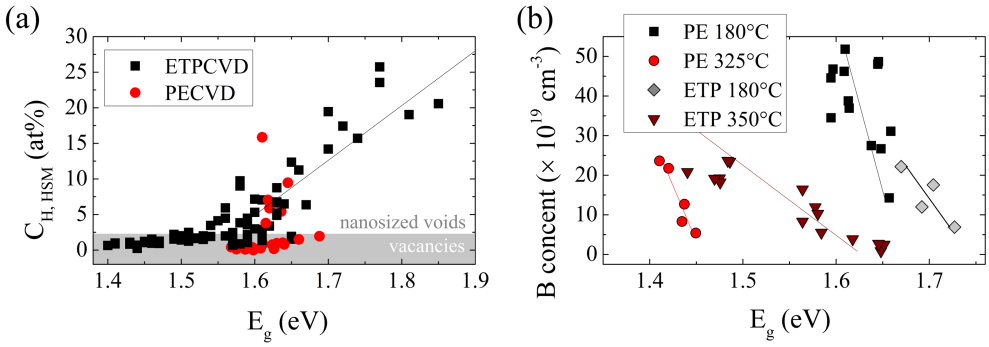


Figure 4.7. (a) The HSM related H content $C_{H,HSM}$ as function of E_g for ETPCVD and PECVD deposited films, as reported by Smets et al. [48]. (b) The B content depicted with respect to the E_g to show the influence B and H on the E_g.

The influence of the B content on the E_a values is similar for PECVD and ETPCVD deposited films. The E_a reduces with an increase in B content. The influence of the deposition temperature on the E_a is also similar for both techniques. A higher deposition temperature

results in a lower E_a, indicating that the amount of active dopants in the as-deposited films depends strongly on the deposition temperature (figure 4.6(b)).

4.5 Conclusion

In this chapter the results of characterization measurements on B-doped ETPCVD a-Si:H films have been presented for the first time. The B-doped ETPCVD deposited a-Si:H films have a B content of approximately 8.5×10^{15} cm^{-2} for a B_2H_6-to-SiH_4 ratio of 0.8×10^{-3}. This B content is similar to PECVD films deposited at 325 °C with a similar B_2H_6-to-SiH_4 ratio. The B content increases with increasing B_2H_6-to-SiH_4 ratio for both deposition techniques. The B content is independent of the deposition temperature for ETPCVD films but decreases with increasing deposition temperature for PECVD films. Crystallisation of the films leads to a doping efficiency of approximately 40%. For the ETPCVD films deposited at 350 °C it is shown that the E_g depends both on the B concentration as well as the H content and configuration. Although additional research into the precise H content is required, the influence is evident from the microstructure parameter R^*.

Chapter 5

Formation of poly-Si on glass observed by in-situ XRD

5.1 Introduction

Several methods can be used to obtain a thin poly-Si film from amorphous silicon (a-Si) deposited on glass, like aluminium induced crystallization, laser induced crystallization and solid phase crystallization (SPC) [115, 116]. The a-Si films can be deposited by techniques such as plasma-enhanced chemical vapour deposition (PECVD) and e-beam evaporation [117]. For the SPC approach to become a viable technology, both the deposition conditions and the annealing treatment should be optimized in order to minimize the energy consumption during production and achieve a high solar cell performance. The maximum temperature of the annealing treatments for industrial solar cell production should be limited to about 650 °C, which is the glass softening temperature.

Additionally, an advantage of lower temperatures for processing is that it reduces the thermal budget and the thermal stress induced by the annealing treatment.

In this chapter intrinsic poly-Si films were obtained by annealing hydrogenated amorphous silicon (a-Si:H) films, deposited by expanding thermal plasma chemical vapour deposition (ETPCVD). We studied the influence of the annealing temperature on the rate of phase transition for temperatures in the range between 500 and 700 °C. We also investigated the effect of the hydrogen content and the hydrogen bonding configuration on the phase transition from a-Si:H to poly-Si. We will demonstrate that a temperature of at least 600 °C is needed to achieve crystallization. In addition we will show that the grain size decreases with microstructure factor, R^*, suggesting that the nucleation density is dependent on the microstructure of the material.
This chapter is organized as follows: sections 2.1.2, 2.2, and 5.2 describe the details of the deposition technique, the measurement techniques employed and the annealing procedures. Section 5.2 is followed by the presentation and discussion of the results of the crystallization for the different annealing profiles (section 5.3 and 5.4). The average crystallite sizes of the poly-Si films are discussed in section 5.4.

5.2 Experimental details

The a-Si:H films were deposited by the ETPCVD method, which has been discussed in detail in section 2.1.2. The a-Si:H films were deposited on Eagle 2000 Corning glass and on c-Si boron doped prime CZ wafer with ⟨100⟩ orientation. The depositions were made under the same conditions except for the substrate temperature. The gas flows were: 690 sccm Ar, 340 sccm H_2 and 230 sccm SiH_4. The arc current was 40 A. The arc pressure was approximately 45×10^3 Pa. The pressure in the deposition chamber was approximately 20 Pa. The film thicknesses were approximately 850, 1000 and 1700 nm. Fourier Transform Infrared (FTIR) spectroscopy (see section 2.2.1) was used to evaluate the hydrogen content and bonding configuration in the a-Si:H

films. The integrated absorption of the vibration mode at 640 cm^{-1} was used to determine the hydrogen content in the film. The modes centered at $\sim$ 1980-2010 cm^{-1} and 2070-2100 cm^{-1} are designated the low stretching mode (LSM) and high stretching mode (HSM), respectively, and were used to determine the microstructure parameter, R^*. An R^* value below 0.1 is generally found for device quality a-Si:H [75, 31]. The hydrogen content and bonding configuration can be manipulated by the plasma conditions and the substrate temperature during deposition. The deposition temperatures were 200, 300 and 400 °C, resulting in hydrogen contents varying from 5.6 to 11.5 at.%, and R^* ranging from 0.01 to 0.45. Raman spectroscopy (RS) (see section 2.2.2) was used to investigate the presence of the crystalline phase in the layers. From measurements on as-deposited a-Si:H layers we did not detect any crystalline fraction.

The phase transformation of a-Si:H films on glass into poly-Si film was monitored by in-situ x-ray diffraction (XRD). In-situ XRD experiments were carried out in an Anton Paar high-temperature chamber HTK 1200. During the experiments the high-temperature chamber was pumped down to 2×10^{-1} Pa. Futher measurement details and processing methods can be found in section 2.2.3.

Two annealing treatments have been used in the in-situ experiments, the profiles of which are shown in figure 5.1.

- Profile A_F: is a simple plateau (figure 5.1a).
- Profile A_{8h}: is similar in to A_F in ramp up, but has a duration of 8 hours (figure 5.1b).

The first annealing profile (A_F) is used to evaluate the crystalline fraction that develops within 2 hours of annealing. The A_F profile was carried out on four similar samples using four different plateau temperatures: 500, 600, 650, and 700 °C, to evaluate the influence of temperature on the crystallization process. Profile A_{8h} was carried out at 600, 610 and 620 °C; during these treatments in-situ XRD

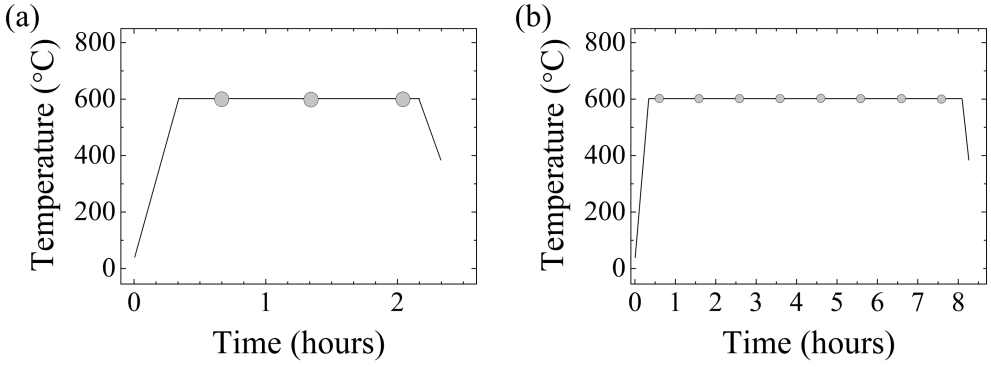


Figure 5.1. Sketches of the temperature profiles used for the annealing profiles. The circles indicate the time at which the in-situ XRD measurements are made: (a) Ramp up to constant temperature and annealing for two hours. This profile, each time with the same ramp up, is also used for temperatures from 500 to 700 °C; (b) ramp up to constant temperature and annealing for eight hours. This profile is used for temperatures of 600 to 620 °C.

measurements were carried out each half hour. The samples used for in-situ measurement during profile A_F had thicknesses of around 1700 nm and a hydrogen content of approximately 6 at.%; for the A_{8h} profile, samples with a thickness of approximately 1000 nm and hydrogen content around 8 at.% were used.

Ex-situ XRD measurements were carried out on samples deposited at different temperatures to obtain variation in the hydrogen content and bonding configuration in the films. The samples were annealed for 2 hours using profile A_F. The plateau temperatures for this annealing treatment were, at 600, 612 and 625 °C for samples with a thickness of 1700 ± 50 nm and 600 °C only for samples with a thickness of 1000 ± 50 nm and 850 ± 50 nm. An overview of the samples, annealing profiles and temperatures can be found in table 5.1. After the annealing treatment the samples were cooled down and measured ex-situ using XRD, the results of which are shown in figure 5.5.

Table 5.1. Overview of XRD experiments for different annealing profiles, A_F in-situ, A_{8h} in-situ and A_F ex-situ. The profiles are described in section 5.2 and figure 5.1.

	A_F (in-situ)	A_{8h} (in-situ)	A_F (ex-situ)
Annealing time (h)	2	8	2
Measurements per sample	4	16	1
Sample thickness (nm)	1700 ± 50	1000 ± 50	850 ± 50 1000 ± 50 1700 ± 50
Plateau temperature (°C)	500/600/650/700	600/610/620	600/612/625
Deposition temperature (°C)	400	300	200/300/400

5.3 Results

Figure 5.2 shows the results of the measurements made during annealing profile A_F at 500, 600, 650 and 700 °C. Each plot shows measurements carried out after the same annealing time at different temperatures. For the sample annealed at 500 °C no {111} line is observed during the two hours of annealing. The sample annealed at 600 °C shows almost no peak after 85 minutes (A_{F2}), but this peak is clearly present after 125 minutes as can be seen in figure 5.2(c) (A_{F3}). For samples annealed at 650 and 700 °C the {111} integrated intensity saturates before the first measurement. After the annealing by profile A_F, RS was carried out on these four samples. The four XRD diffraction patterns are shown in figure 5.2, the RS spectra in figure 5.3. The sample annealed at 500 °C shows no crystalline TO peak, located at 520 cm^{-1}. The detail in figure 5.3 shows all spectra scaled to the sample annealed at 600 °C. This sample has both amorphous and crystalline material: the TO peak of the amorphous material (at 480 cm^{-1}) is present, as is the crystalline TO peak (located at 520 cm^{-1}). The samples annealed at 650 and 700 °C a strong TO peak is present. These films show no TO peak (at 480 cm^{-1}).

Figure 5.4 shows the measurements made during the A_{8h} annealing profile at three different temperatures: 600, 610, and 620 °C. In this figure the integrated intensities of the {111} diffraction line are

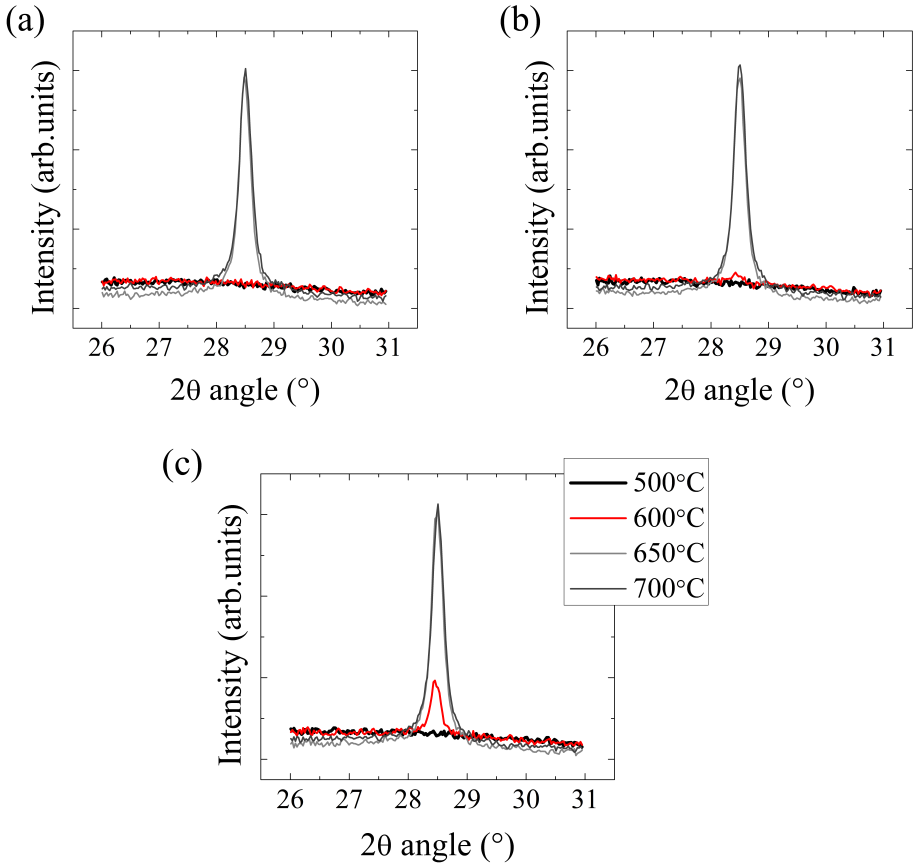


Figure 5.2. XRD scans of the $\{111\}$ line for samples annealed using profile A_F at temperatures varying from 500 to 700 °C: (a) after 45 minutes, A_{F1} (b) after 85 minutes, A_{F2} and (c) after 125 minutes, A_{F3}.

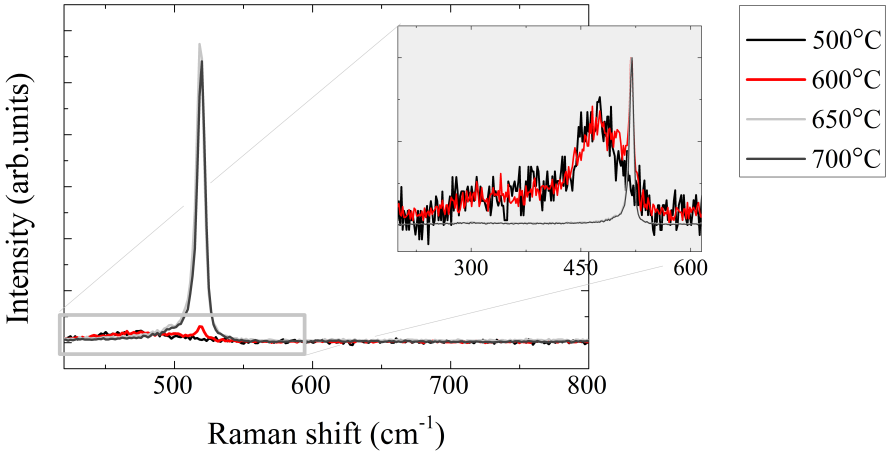


Figure 5.3. The RS spectra made after the XRD experiments shown in figure 5.2 are shown in this figure. The RS spectra in the inset have been scaled to the transverse optical modes of the sample annealed at 600 °C.

plotted, which indicate to what extent the transition from amorphous to the crystalline phase is completed. The films are assumed to be fully crystallized when reaching this level (as was confirmed by RS). The time in which full crystallization is reached, is shortened with increasing annealing temperature.

Ex-situ measurements were performed after annealing treatments with profile A_F at a temperature of 600, 612 and 625 °C. The samples used for these experiments had different hydrogen contents and bonding configuration before SPC (induced by deposition at temperatures of 200, 300, and 400 °C).The {111} line intensities were somewhat lower for material with hydrogen contents lower than 9 at% and R^* values lower than 0.3 [118]. These results were not conclusive as observations are within the error margins of these measurements. A small series of ETPCVD deposited a-Si:H with a full range of hydrogen content and R^* values was annealed at 600 °C for two hours (A_F). The integrated intensities of the {111} lines, scaled to the film thickness, are shown

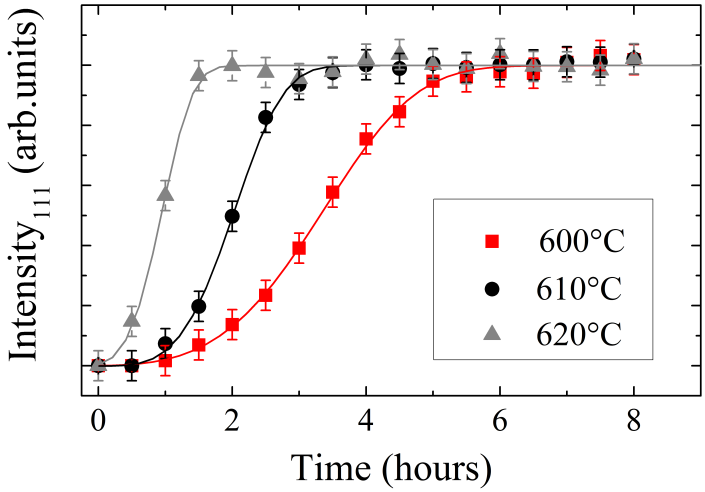


Figure 5.4. Plots of the integrated intensity of the $\{111\}$ line as measured by XRD as a function of annealing time during annealing profile A_{8h}, executed at three different temperatures: $600\ ^{\circ}\mathrm{C}$ (squares), $610\ ^{\circ}\mathrm{C}$ (circles), and $620\ ^{\circ}\mathrm{C}$ (triangles). The integrated intensities are normalised to the saturation values of the fitted lines. The lines are the result of the AJM analysis.

in 5.5. Despite the error margin of the measurement a decrease in crystallinity is observed for hydrogen contents exceeding 9 at%. A clear trend can be observed for the decrease in crystallinity as a function of the R^* over the full range of R^* values.

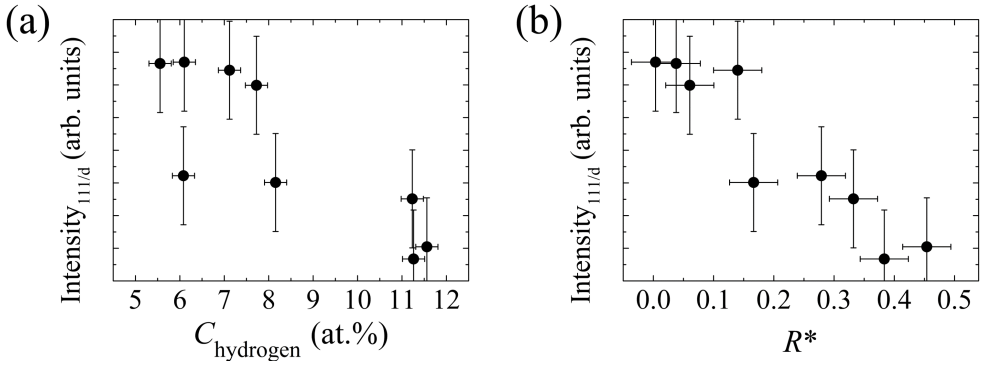


Figure 5.5. The integrated intensity of the XRD {111} line as a function of (a) the hydrogen content and (b) the microstructure parameter, R^*, for samples annealed at 600 °C for two hours. All measurement results have been normalized to the fully crystalline integrated intensity, and compensated for the sample volumes.

Figure 5.6 shows the crystallite size estimated from the {111} XRD line. All samples presented were deposited at 300 °C. The general trend shows a reduction of crystallite size with annealing temperature. The crystallite size shows no dependence on the film thickness. However, the error margins are too large for this data to be conclusive.

5.4 Discussion

The initial experimental results by XRD of the SPC process, figure 5.2, show that crystallization is observed at annealing temperatures of 600 °C. The complete crystallisation curves, shown in figure 5.4, have been analysed using the AJM model, as explained in section 2.2.3. The AJM model parameters found for the SPC process are listed in 5.2 for

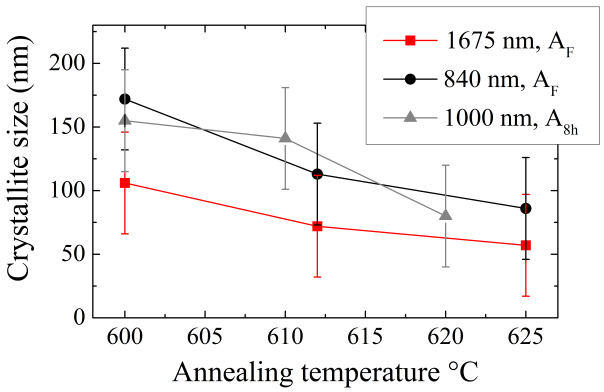


Figure 5.6. The crystallite size as a function of the annealing temperature during SPC. The crystallite size is obtained from the XRD pattern. The red square and black circle markers show the results from the A_F profile. The grey triangles show the results from the A_{8h} profile.

steady state nucleation we found that $\theta < 0$ h. This value indicates the presence small crystallites or nucleation sites in the a-Si:H film prior to annealing. θ does not appear to be temperature dependent in this series, confirming the concept of pre-existing nuclei. The presence of crystallites is not confirmed by the RS measurements of the as-deposited films, most likely a result of the fact that the crystallites cannot be detected by RS due to location and size. The crystallisation time (τ_c) from the AJM model strongly depends on the annealing temperature, as can be concluded from table 5.2. As the τ_c depends on the nucleation rate and the grain growth (related to the jump rate of atoms at the surface of a grain) this temperature dependence is expected.

Table 5.2. Overview of AJM model parameters of the crystallisation curve (figure 5.4).

Annealing temperature	600 °C	610 °C	620 °C
Start time nucleation θ (h)	-0.69 ± 0.27	-0.11 ± 0.17	-0.39 ± 0.22
Crystallisation time τ_c (h)	4.37 ± 0.30	2.31 ± 0.19	1.45 ± 0.23

The influence of hydrogen content and bonding configuration on the crystallisation process is shown in figure 5.5. The degree of crystallisation after two hours annealing decreases with R^* (and hydrogen content). Hydrogen effusion from a-Si:H films occurs around 300 °C [99]. Effusion must be occurring during the annealing treatment, as the solubility of hydrogen in silicon is lower for the crystalline phase than in the amorphous phase [119]. The lower XRD integrated intensity could be due to a lower density of the material, which in turn may be caused by hydrogen entrapment. However, we observe differences too large to support this explanation (see figure 5.5). Up to about 8 at.% hydrogen concentration no difference in crystallisation is observed. The influence of the R^* appears more prominent than the influence of the actual hydrogen content. It should be noted that R^* increases with increasing hydrogen content for ETPCVD films; a high R^* value is indicative of void rich material. From figure 5.5 (b) we conclude that for dense material (low R^*) more crystalline material is formed during the annealing treatment. Grain growth becomes easier when sufficient neighbouring atoms are available for repositioning at the grain boundary or the crystallite surface (this influences the jump rate). For this reason it is likely that high R^* values and high hydrogen content limit the grain growth.

From crystallisation experiments estimates of the average crystallite size has been calculated. Although the error margins are substantial, all three series show a decrease in crystallite size with increasing annealing temperature, figure 5.6. This observation suggests that apart from the influence of temperature on the grain growth, the temperature also influences the nucleation rate. The trend visible in figure 5.6 can be explained by assuming that the rate at which stable nuclei are formed, increases with increasing temperature. As these nuclei grow into crystallites, the distance between two neighbouring nuclei (nuclei density) can be the limiting factor for the crystallites to grow. This cannot explain why the thinner film has a larger crystallite size. It is possible that hydrogen effusion paths [99] influence the nucleation rate, and that the film thickness influences the hydrogen effusion. Comparing the series from figure 5.6 it should be noted that results of the A_F profile are not

always completely crystalline: the films annealed for 2 hours, annealed at 600 °C still hold an amorphous fraction. The average crystallite size from both annealing treatments is similar, despite the difference in crystallinity.

5.5 Conclusion

We have observed that after annealing at temperatures of 650 °C and above the {111} integrated intensity saturates before the first measurements (A_{F1}). Annealing at 500 °C does not induce any crystallization at all during the flat profile, as is confirmed by RS. In addition, RS indicates that films still contain an a-Si:H fraction after annealing at 600 °C for two hours. In the samples annealed at 650 °C and above no a-Si:H contribution is detected by RS.

A-Si:H films of approximately 850 nm to 1700 nm, deposited by ETPCVD, can be fully crystallized within 2 hours at temperatures in the range of 620 to 650 °C. The crystallization rate increases with annealing temperature. Additionally the results demonstrate that the annealing temperature has a large influence on the rate of phase transition. Hydrogen content and bonding has been shown to influence the crystallization process, specifically an increase in R^* decreases the crystallisation rate. The average crystallite sizes for fully crystallized and mixed phase films are both in the order of 60 to 170 nm.

Chapter 6

Influence of B doping and R^* on the crystallisation of a-Si:H

In this chapter the SPC of B-doped a-Si:H, deposited using plasma enhanced or expanding thermal plasma CVD, is examined. By varying the deposition conditions the B doping level and the microstructure of the material is altered. This chapter shows that the microstructure of the as-deposited material is hardly affected by incorporating B in the material, whereas the SPC kinetics become much faster. This chapter is organized as follows. In the next section we will discuss (i) the experimental procedures for making the a-Si:H layers, (ii) the determination of the microstructure parameter R^*, and (iii) the XRD setups and methods used during the experiments. In the Results section the in-situ XRD data on doped a-Si:H layers having varying dopant concentration and microstructure is shown. This section is followed by the discussion of the in-situ XRD results using the Avrami-Johnson-Mehl (AJM) model for phase transition [88, 89, 90, 91].

6.1 Introduction to Solid Phase Crystallisation of doped a-Si:H

Thin layers of c-Si can been obtained using several methods. The most direct way of making thin c-Si layers is by cleaving or sawing crystalline silicon from ingots [120]. Alternatively, other methods use the crystallization of amorphous silicon (a-Si) or a-Si:H, in particular laser-induced crystallization (LIC) [25] and solid-phase crystallization (SPC) [25, 117] resulting in polycrystalline silicon (poly-Si). Using LIC Dore et al. [121] made c-Si grains with a size of 1 mm wide and 10 mm long for 10 μm thick films, and solar cells were made having a conversion efficiency of 8.4% [121]. Problems using LIC are associated with the control of the heat transfer of the laser light to the silicon layer, in particular for films with thickness of more than 300 nm [122]. Another method for the production of thin-film poly-Si is SPC of a-Si(:H) films. In this method a thin layer of a-Si(:H) is annealed at temperatures in excess of 560 °C [123], leading to the formation of c-Si regions. The annealing temperature can be reduced when the crystallization process is catalysed using a metal, most notably Al. This Al-induced crystallization of a-Si(:H) leads to layers having grain sizes of up to 18 μm [124] and as Al is a dopant in Si, the material is always p-type doped. Gall et al. [124] demonstrated this method making solar cells with an efficiency of 2.7%, but higher efficiencies have been reached for other SPC solar cells. A major drawback of the SPC methods is the low open-circuit voltage, V_{OC}, resulting from a high intragrain defect densities [125].

The defect densities in cast c-Si are often associated with the B-content. However, studies on the crystallization process by SPC have mostly been carried out on intrinsic a-Si(:H) layers or on complete solar-cell stacks. Sharma et al. [126] showed that the crystallization kinetics of intrinsic a-Si:H depends strongly on the hydrogen concentration and the microstructure of the material, expressed in the microstructure parameter, R^*, obtained from the stretching modes in the infrared absorption spectra of as-deposited films. Faster crystallisation was observed for lower values of R^*. The largest average grain size was obtained

for material having an R^* value of about 0.3. The faster crystallisation was induced by a faster onset of crystallisation, the onset changes in two ways: (i) the crystallisation onset time increases with decreasing the medium range order (MRO) for low R^* values; (ii) for layers with increased disorder (i.e., R^*>0.3) the onset decreases with a further decrease in the MRO of the a-Si:H. This is could be induced by nano-sized voids collapsing upon hydrogen out-diffusion, leading to a more compact structure during SPC. Technologies based on chemical vapour deposition (CVD) allow for doping of a-Si:H films during the deposition process. The great benefit of doping during the deposition is that (depending on the cell design) post crystallization doping is no longer necessary. Olson and Roth [46] described the crystallization process of doped a-Si(:H) and found that both B and P doping increase the crystallization velocity in epitaxial growth experiments [46, 127]. For amorphized compensated intrinsic a-Si Suni [128, 129] showed that the crystallization velocity is dependent on the doping level and not on the dopant atom. Additionally, B doping greatly enhances the diffusion of hydrogen in a-Si:H . Therefore it is expected that the SPC of a-Si:H is influenced by the B doping. The solubility of H in c-Si is in the order of 10^{16} cm^{-3} [99] while up to 25% H can be present in a-Si:H and therefore full crystallisation requires effusion of H. The H effusion characteristics of a-Si:H are very dependent on the microstructure of the material.

6.2 Experimental details

Samples have been deposited using two different techniques: Radio-Frequency Plasma Enhanced Chemical Vapour Deposition (PECVD) at 13.56 MHz and Expanding Thermal Plasma Chemical Vapour Deposition (ETPCVD). The PECVD setup has a conventional parallel plate configuration with an electrode distance of 10 mm for the intrinsic deposition chamber and 11 mm for the B-doped deposition chamber. The precursor gases were SiH_4 and H_2. For B-doped a-Si:H, B_2H_6 (2% in H_2) was added to the gas mixture. The layers were deposited using an RF power of 28 mW/cm^2 and a deposition pressure of 70 Pa. The deposition temperature of the PECVD samples was 180 °C and the layers

were deposited at a rate of approximately 0.15 nm/s. For ETPCVD of a-Si:H, a DC Ar-H_2 plasma is created in a narrow channel of a cascaded arc at a pressure of approximately 45 $\times$ 10^3 Pa. The current in the arc is 40 A. The plasma expands through a nozzle into the deposition chamber and at this point H_2 is injected. B-doped films are made by adding B_2H_6 to the H_2 injected at the end of the nozzle. In the deposition chamber, about 8 cm below the nozzle, SiH_4 is injected into the plasma beam and the a-Si:H film is deposited on a temperature controlled glass substrate approximately 40 cm downstream. The pressure in the deposition chamber is about 20 Pa. The deposition temperature is 350 °C and deposition rates used for these samples are between 0.35 and 0.5 nm/s. The films have a thickness of approximately 300 nm. The temperature difference between the PECVD and the ETPCVD deposition was chosen to correspond to the solar grade material from both techniques.

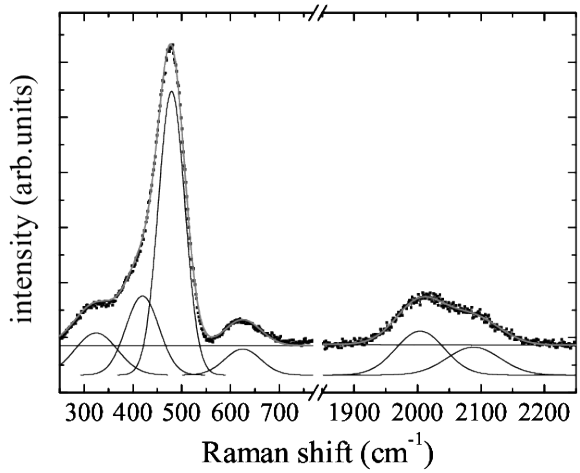


Figure 6.1. Two parts of a typical Raman spectrum of a-Si:H are shown. The 250 to 850 cm^{-1} range shows the phonon modes related to the Si-Si bonds of a-Si:H, the 2000-2100 cm^{-1} region shows the Si-H_x related low and high stretching modes.

The as-deposited (doped) a-Si:H layers were examined by Raman spectroscopy (RS) using a Renishaw InVia Raman spectrometer with a

resolution of 2 cm^{-1}. More specifically attention was paid to the Raman active stretching modes of Si-H vibrations at about 2000 to 2100 cm^{-1} [130], see figure 6.1. By determining the relative contributions of the low and high stretching mode, the microstructure parameter, R^*, is obtained, as is explained in detail in chapter 3. It has been shown that the HSM contribution is associated Si-H_x bonding configurations indicative of void-rich material, whereas the LSM contribution is linked to Si-H bonds in divacancies [73]. This makes the R^* a figure of merit for the microstructure. In this chapter R^*_{R} will be used to indicate that the R^* is determined from the RS spectra. The a-Si:H films were monitored during the crystallization process by in-situ XRD in two sets of experiments. The first experiment consisted of annealing at two temperatures: 580 and 600 °C, in an Anton Paar high temperature chamber HTK 1200 under Ar atmosphere. The samples used in this experiment were intrinsic (PE i and ETP i) or deposited using a B_2H_6-to-SiH_4 ratios of 2×10^{-4} (PE B and ETP B). The second experiment was carried out at 580 °C and 590 °C, in a similar Anton Paar HTK setup. In this second experiment the high-temperature chamber was pumped down to 2×10^{-1} Pa, thereby creating a more controlled atmosphere. The B concentration in a-Si:H influences the H-effusion. For this reason the films with varying doping levels are annealed in a more controlled environment. In this experiment two B-doped PECVD films were annealed at 580 °C and two B-doped ETPCVD films were annealed at 590 °C. The B_2H_6-to-SiH_4 ratios of the PECVD samples were 2×10^{-4} and 7×10^{-4} for PECVD 2B and PECVD 7B, respectively. The ETPCVD films for the second experiment were made with B_2H_6-to-SiH_4 ratios 1.7×10^{-4} and 7.3×10^{-4} (ETP 1.7B and ETP 7.3B, respectively).

In both cases XRD patterns were collected by an automatic powder diffractometer in symmetric geometry, using Copper K_α characteristic radiation ($\lambda = 0.154$ nm). The irradiated area of each sample was up to 10 mm × 10 mm. The XRD pattern was measured in 4 minutes for θ varying from 26 to 31 degrees, where the strongest silicon line of the (111) planes is located. A typical measurement is shown in figure 6.2. As a measure for crystallization, the crystalline fraction, χ, was deter-

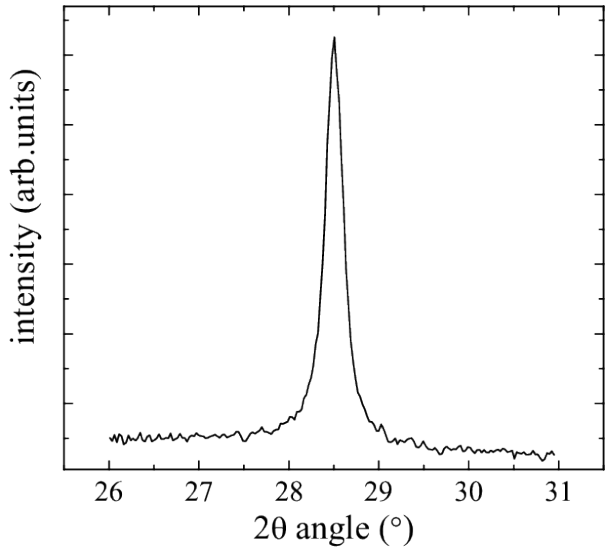


Figure 6.2. Example of an XRD pattern showing the (111) line of silicon as measured during the annealing procedure.

mined by normalizing the integrated intensity of the (111) line during crystallization with respect to the average integrated intensity of the (111) line of the film after saturation of crystallisation occurred. This fully crystallized film will be referred to as the material with crystalline fraction χ=1. After annealing RS was used to confirm that the films were indeed completely crystallized.

6.3 Results

Before the crystallization experiments, the as-deposited (B-doped) a-Si:H layers were first characterized using RS (specifically focusing on the Si-H_x stretching modes). RS was used to detect the presence of any crystalline phase in the as-deposited films and we found that all as-deposited films were amorphous. A typical Raman spectrum is shown in figure 6.1. For layers deposited using ETPCVD no strong relation between B_2H_6-to-SiH_4 ratio and R^*_R was observed. We found that R^*_R is to a large extent determined by the deposition tempera-

ture: at low deposition temperatures the R^*_R of the PECVD samples showed a slight increase with increasing B_2H_6-to-SiH_4 ratio. The R^*_R of the ETPCVD samples deposited at low temperatures is highest, followed by the low temperature PECVD samples, high temperature ETPCVD samples, and the lowest R^*_R values were observed for the high temperature PECVD samples. We conclude from these results that the microstructure is therefore strongly related to the deposition technique and temperature. For annealing experiments and in-situ XRD analysis we selected samples with varying R^*_R deposited at different B_2H_6-to-SiH_4 ratios.

In figure 6.3 examples of the time evolution of the crystalline fraction, χ, are shown for intrinsic and B-doped a-Si:H films deposited with ETPCVD and annealed at 580 °C, and deposited with PECVD and annealed at 600 °C. For all films χ follows the typical S-shape that characterizes the crystallization of a-Si:H. Intrinsic films deposited by ETPCVD and PECVD show similar crystallisation kinetics for annealing at 600 °C. The onset of crystallisation of the PECVD sample, which has a larger R^*_R, is slightly later than for the ETPCVD and the slope of the S-curve is smaller. The slight differences between the PECVD and ETPCVD crystallization curves are amplified in the SPC treatment at 580 °C, for which we observe that the crystallisation of the ETPCVD film is now much quicker than of the PECVD film. Sharma et al. [6] showed that the total crystallization time was shorter for intrinsic ETPCVD a-Si:H films with smaller R^*. The reduction of the total crystallisation time was largely due to a reduction of the onset time to crystallisation, θ, with a decrease of R^*. This R^* dependence of the crystallization behaviour is observed when we compare the crystallization of our intrinsic ETPCVD sample with an intrinsic PECVD sample. This indicates that the influence of R^*_R on the crystallisation of intrinsic a-Si:H films deposited by PECVD is similar to that of films deposited by ETPCVD.

The R^*_R of the as-deposited intrinsic PECVD samples is higher than of the intrinsic ETPCVD samples. The samples deposited with a B_2H_6-to-SiH_4 ratio of 2×10^{-4} have a lower R^*_R than the intrinsic

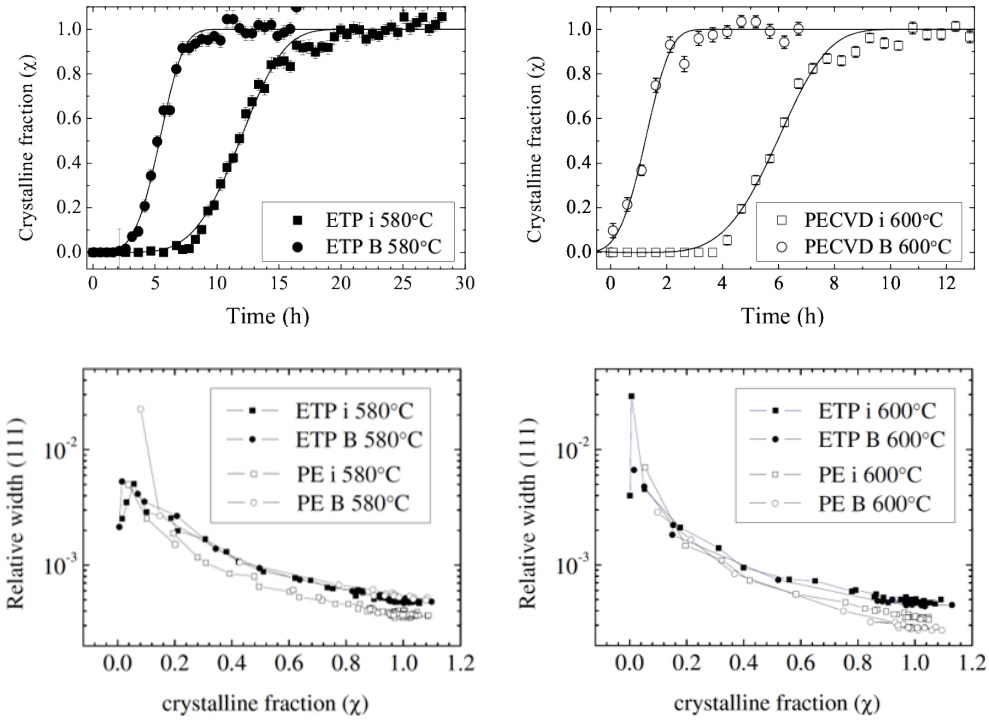


Figure 6.3. (a,b) Show the results of the in-situ XRD measurements of the (111) diffraction line. The markers show the crystalline fraction χ as a function of annealing time. The lines show the AJM model fitted to the $\chi(t)$. (c,d) Show the width-per-integrated intensity of the (111) diffraction line as a function of the crystalline fraction χ. The connecting lines are guides to the eye.

samples deposited by the same technique. The most important observation from figure 6.3 is that the onset time for crystallization is reduced when B is incorporated into the film. In addition, the slopes of the crystallization curves become steeper when B_2H_6 is added to the gas mixture. From the XRD measurement results it turns out that the onset of crystallization for the PECVD sample annealed at 600 °C occurs before the annealing temperature has been reached. Although the slope of the ETPCVD sample is slightly steeper than that of the PECVD sample, the overall crystallization time is smaller for the PECVD sample due to the short crystallization onset time. The experiment conducted at 580 °C shows a faster onset of crystallisation, like at 600 °C, but in this case the slope is also steeper for the PECVD sample crystallisation curve compared to that of the ETPCVD sample. We conclude that the crystallization is faster when the samples are B doped and that the effect of B doping on the crystallization time is stronger for PECVD samples than for ETPCVD samples.

In the second experiment the S-shape results of the χ are similar to the results of the first experiment, but the time scale is slightly different. The difference is most likely caused by differences between the setups. Increasing the B_2H_6-to-SiH_4 ratio leads to a faster onset of crystallisation, more strongly for the ETPCVD samples than for the PECVD samples. The slope of the crystallisation process increases with increasing B_2H_6-to-SiH_4 ratio. The effect is more pronounced for the PECVD samples. A strong reduction in the time to crystallisation saturation is observed for both techniques.

6.4 Discussion

In the S-shaped crystallization curves we distinguish two separate parts: (i) the period until the onset of crystallization, and (ii) the curve from the onset of crystallization until crystallization saturation (full crystallisation). The time to full crystallization is affected by the onset or retardation time and the slopes of the crystallization curves. In order to quantify these aspects the measured crystalline fractions are fitted using

the Avrami, Johnson and Mehl (AJM) model [88, 89, 90, 91]. Avrami, Johnson and Mehl [88, 89, 90, 91] used a phenomenological approach to develop an expression for the crystalline fraction. The AJM description can be applied to many kinds of nucleation. In fact the same equations can be constructed from a classical model for nucleation of a solid from a liquid or gas phase [33]. The basic assumption of this model is that no nucleation or growth occurs during the retardation or effective lag time, θ, and that any misfit strain is negligible. Experimentally, θ is related to the minimum detectable grain size or crystalline material volume and is therefore dependent on the measurement technique. In the model, the nucleation rate is defined as the increase of grain density per unit time and is assumed to reach steady-state value (I_s) when t = θ [91]. The grain growth rate, ν_g, is assumed to be time independent. With this assumption the crystallized volume fraction, χ, as function of annealing time can be expressed as:

$$\chi(t) = 1 - \exp(-(\tfrac{t-\theta}{\tau_c})^4) \tag{6.1}$$

In here τ_c is the crystallization time, defined as:

$$\tau_c = (3/\pi d I_s {\nu_g}^3)^{\frac{1}{4}} \tag{6.2}$$

with d the film thickness. The grain growth rate ν_g is directly related to the jump rate of atoms at the surface of a grain [92, 47]. I_s and the ν_g are typically described by Arrhenius type equations. However, often ν_g is simplified with a single Arrhenius equation with an associated activation energy of SPC ($E_{a,SPC}$) [93]. In a similar fashion an Arrhenius equation is often used to evaluate the activation energy of the onset time to nucleation, θ. The results of this analysis are presented in table 6.1.

As XRD is only sensitive to the crystalline phase, the assumptions of steady-state nucleation and time-independent grain growth rate cannot be confirmed directly. From literature reports B is known to increase ν_g by a factor of 10 to 25 for epitaxial growth of silicon films [127, 46, 5]. If we assume such a large increase in ν_g and no change in

Table 6.1. List of samples, sample properties and AJM results. The first column shows the R^*_{R} from the Raman measurements for the as-deposited films. The annealing temperature used during the in-situ XRD experiments I and II is included. Experiment I was carried out under Ar atmosphere, whereas experiment II was carried out in vacuum. Results of the AJM-analysis of the XRD measurements are included: θ indicates the AJM onset of crystallisation and τ_c the total time to crystallisation. The final column shows the activation energy for SPC (E_{aSPC}), determined from the AJM results.

	R^*_{R}	T_{anneal} (°C)	θ_{580} (h)	θ_{590} (h)	θ_{600} (h)	$\tau_{c,580}$ (h)	$\tau_{c,590}$ (h)	$\tau_{c,600}$ (h)	$E_{a,SPC}$
PECVD i	0.380 ± 0.163	I580	3.541			13.89			3
		I600			0.9446			5.495	
PECVD (2)B	0.211 ± 0.076	I580	0.7137			3.344			0.6
		I600			-1.261			2.737	
		II580	0.0707			2.422			
PECVD 7B	0.383 ± 0.062	II580	0.4081			1.179			
ETP i	0.222 ± 0.102	I580	2.005			10.78			1.6
		I600			-0.222			6.457	
ETP (2)B	0.142 ± 0.099	I580	0.0057			5.873			2.6
		I600			0.2086			2.591	
ETP 1.7B	0.241 ± 0.053	II590		0.7798			1.834		
ETP 7.3B	0.132 ± 0.148	II590		-0.2395			1.478		

I_s, then according to the AJM model τ_c should decrease by 82 to 91%. The decrease observed for our doped films is in between 45 and 76%, implying that I_s of the B-doped films is lower if the assumption of a large increase in ν_g is correct. A difference in I_s between the B-doped and intrinsic samples should result in a difference of the width of the (111) diffraction line, as described by Langford and Wilson [131]. For an infinite crystal the number of reflection planes is infinite and therefore the diffraction line is in fact a line. For small crystallites the number of reflection planes is restricted, resulting in a broadening of the (111) diffraction line. This width is expected to be smaller for lower I_s values. In figure 6.3 we show the development of the (111) relative width, defined as the width-to-integrated intensity ratio, as a function of crystalline fraction χ. From this figure we can see that for all samples the relative width of the (111) initially increases ($\chi < 0.1$) and then decreases with χ. According to Sharma et al. [6] annealing of intrinsic ETPCVD samples with a larger R^* results in films with a larger grain size. As the R^*_{R} of the intrinsic PECVD samples is larger than those of the intrinsic ETPCVD samples it is reasonable to expect a lower nucleation rate and therefore smaller width of the (111) diffraction line, as we observe in figure 6.3. This observation supports the idea that the crystallization of intrinsic a-Si:H films deposited by PECVD are affected by R^*_{R} in a similar way as ETPCVD films. The observation indicates that the grain density in the intrinsic PECVD samples is smaller than in the ETPCVD samples.

Because of the difference between the expected and determined τ_c due to an increase in ν_g we think that the I_s values of the B-doped samples are smaller than the intrinsic samples. These smaller I_s values result in a decrease of the diffraction line width of the B-doped samples. For a given annealing temperature the absolute diffraction line width of the B-doped ETPCVD films is equal to that of the intrinsic ETPCVD films. The ETPCVD samples annealed at 600 °C have slightly smaller absolute and relative width than those annealed at 580 °C, implying a lower grain density. No difference between the B-doped and intrinsic ETPCVD results is observed. This indicates that the grain density of the B-doped samples is similar to that of the intrinsic samples made by

ETPCVD. The only detected difference is a dependence of the grain density on the annealing temperature.

Comparing B-doped to the intrinsic PECVD films, is more complex. The B-doped PECVD sample annealed at 580 °C shows a larger relative width than the intrinsic PECVD sample, in contrast to our expectations outlined above. The reverse is observed for the B-doped PECVD sample annealed at 600 °C, this shows a smaller relative width than the intrinsic PECVD sample. Only one set of samples showed a decrease in the relative width with B-doping, the PECVD sample annealed at 600 °C. This leads us to conclude that the differences in τ_c of the intrinsic and B-doped samples, deposited by both techniques, are not caused by a decrease in I_s. The difference in τ_c of the intrinsic and B-doped samples is the result of a increase in ν_g, which is smaller than the increase expected from our literature study. The observed decrease in τ_c could be related to the degree of B-doping. The differences between the crystallisation of the B-doped ETPCVD and B-doped PECVD films can be influenced by I_s and/or τ_c. We therefore conclude that the variation of I_s is not the main factor for the difference in crystallisation behaviour of the intrinsic and doped samples.

In order to study the observed differences between the B-doped ETPCVD and PECVD films in more detail, a second experiment was carried out in which the effect of increasing B-doping is investigated. With this experiment we attempt to shed more light on the differences between the values of ν_g described in literature reports and our findings. Olson and Roth [46] described that at very high B concentrations the increase of the grain growth rate, ν_g, was diminished by B precipitates or B-Si complexes. The crystallisation curves of four additional samples are measured and analysed using the AJM model and the results are presented in figure 6.4 and table 6.1. By increasing the B_2H_6-to-SiH_4 ratio to 7×10^{-4} and higher we obtained lower τ_c values, indicating a further increase of ν_g. The PECVD film 7B shows a decrease of τ_c with respect to 2B of 51% (for annealing at 580 °C) and the ETPCVD film 7.3B a 19% decrease with respect to 1.7B (for annealing at 590 °C).

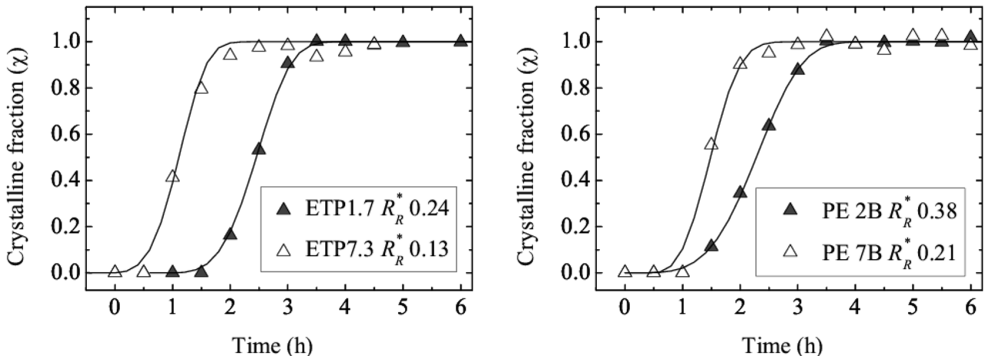


Figure 6.4. The results of the in-situ XRD measurements of the (111) diffraction line, measured using the second XRD setup. The markers show the crystalline fraction χ as a function of annealing time. The lines show the AJM model fitted to the $\chi(t)$.

The second experiment also provides information on the influence of R^*_{R} on τ_c and θ. Two samples were selected having similar R^*_{R} but different deposition techniques. These samples were annealed at 580 °C and 590 °C. Notably the crystallisation curves of the PECVD 2B sample annealed at 580 °C and the ETP 1.7B annealed at 590 °C look very similar. These two curves are used as a reference to observe changes in the crystallisation curves when: (i) the B_2H_6-to-SiH_4 ratio is increased from $1.7{\times}10^{-4}$ and $2{\times}10^{-4}$ to $7{\times}10^{-4}$ and $7.3{\times}10^{-4}$, and (ii) the R^*_{R} of the PECVD sample is increased and the R^*_{R} of the ETPCVD sample is reduced. The results show that increasing the B_2H_6-to-SiH_4 ratio shortens θ and τ_c. A decrease in R^*_{R} should lead to reduction of the incubation time θ according to Sharma et al. [6]. The θ of PECVD 7B and the ETP 7.3B samples is reduced in both cases, showing the influence of B. The degree to which θ is reduced is affected by the R^*_{R} of the samples. The reduction in θ is smaller for the PECVD sample for which the R^*_{R} increases, and larger for the ETPCVD samples for which R^*_{R} decreases.

6.5 Conclusion

We have shown that B doping reduces the onset of crystallization of a-Si:H and the crystallization time. From the analysis of the XRD results we conclude that B enhances the grain growth rate of the B-doped a-Si:H films, but that the effect of the B on the nucleation rate is limited. The extent of the enhanced grain growth rate due to B doping is controlled by the B_2H_6-to-SiH_4 gas flow ratio, for both PECVD deposited films and ETPCVD deposited films. In addition to the influence of B, we conclude that also R^*_R influences the crystallisation process. For both intrinsic PECVD and ETPCVD samples increasing R^*_R increases the onset time to crystallization [6]. The influence of R^*_R is also present in the crystallisation process of the B-doped a-Si:H films deposited by ETPCVD and PECVD.

Chapter 7

Conclusions

This dissertation is part of a study into the development of thin film crystalline silicon solar cells. Such solar cells would require a thickness of approximately 10 μm to ensure sufficient light absorption [3]. The deposition of films with such a thickness requires high deposition rates, in this case Expanding Thermal Plasma Chemical Vapour Deposition (ETPCVD). This dissertation will discuss the crystallisation of a-Si:H films deposited by ETPCVD.

Different from the crystallisation process of a molten material, the mobility of atoms during the solid-phase crystallisation process is limited. For this reason the configuration of atoms prior to the crystallisation process can strongly influence the onset and time required for crystallisation. In the case of a-Si:H, not only a reconfiguration of the Si atoms is needed. The solubility of hydrogen atoms in c-Si is much lower than in a-Si:H [4] and for this reason hydrogen atoms must diffuse out of the film during annealing. Therefore information on the structure of the amorphous films prior to crystallisation is essential. In this thesis the silicon microstructure and the hydrogen bonding configuration of

as-deposited films are studied, and in particular their influence on the crystallisation process.

Fourier Transform Infrared (FTIR) spectroscopy is frequently used to detect the Si-H_x stretching modes to determine the microstructure parameter R^* of a-Si:H films. The stretching modes can also be detected by Raman Spectroscopy (RS). In contrast to FTIR, RS can make substrate independent measurements. In this dissertation the detection of hydrogen and hydrogen bonding configurations by RS is compared to the detection by FTIR. The Si-H_x wagging and stretching modes can be detected by both techniques and is strongly related to the rocking-wagging mode detected by RS. The RS measurements of the Si-H_x related features can be used to evaluate the peak positions of the low stretching mode (LSM), ω_{LSM}, and high stretching mode (HSM), ω_{HSM}, as well as the microstructure parameter R^*. The sensitivity to the low and high stretching modes is not the same for the FTIR and RS measurements and therefore the R^* and $\omega_{\text{LSM,HSM}}$ need to be scaled for comparison. In conclusion the RS measurements can be used to determine the bonding configuration in a-Si:H instead of FTIR, but the hydrogen content cannot be determined.

For thin film polycrystalline Si to be used in solar cell applications, the material must be doped. This can be achieved by doping after crystallisation, but also by crystallising films which already contain the dopant atoms. The main benefit of in-situ doping of the a-Si:H film is a reduction in processing steps. Until this work, no doped a-Si:H films were produced using ETPCVD. This dissertation discusses the deposition of boron doped a-Si:H films by ETPCVD. As dopants can influence the crystallisation process for a-Si films [5], the crystallisation of intrinsic and boron-doped films is studied by in-situ x-ray diffraction during the crystallisation process.

The first boron doped a-Si:H films deposited by ETPCVD are presented in this work. The films are compared to B-doped a-Si:H films deposited by Plasma Enhanced CVD (PECVD). The B-doped ETPCVD deposited a-Si:H films have a B content of approximately 8.5×10^{15} cm^{-2} for a B_2H_6-to-SiH_4 gas-flow ratio of 0.8×10^{-3}. This B content is similar to films deposited by PECVD with a similar B_2H_6-to-SiH_4

ratio. The B content increases with increasing B_2H_6-to-SiH_4 ratio for both deposition techniques. The B content is independent of the deposition temperature for ETPCVD films, but decreases with increasing deposition temperature for PECVD films. Crystallisation of the films leads to a doping efficiency of approximately 40%. For the ETPCVD films deposited at 350 °C it is shown that the bandgap, E_g, depends both on the B concentration as well as the H content and configuration. Although additional research into the influence of the H content on the crystallisation process is required, we conclude that this influence on the crystallization process is evident from the microstructure parameter R^*.

The crystallisation of ETPCVD deposited a-Si:H films by solid-phase crystallisation is studied in-situ using x-ray diffraction (XRD). Annealing at 500 °C does not induce any crystallization at all. Films annealed at 600 °C for two hours still contain an a-Si:H fraction. We have observed that after annealing at temperatures of 650 °C and above the observed crystallinity saturates within half an hour. In these samples no a-Si:H contribution is detected by RS. The hydrogen content and bonding configuration in the as deposited films is shown to affect the crystallization process, specifically an increase in R^* decreases the crystallisation rate.

Both the R^* and the boron content influence the solid phase crystallisation of a-Si:H. We have shown that B doping reduces the onset time for crystallization of a-Si:H and the crystallization time. From the analysis of the XRD results we conclude that B enhances the grain growth rate of the B-doped a-Si:H films, but that the effect of the B on the nucleation rate is limited. The extent of the enhanced grain growth rate due to B doping is controlled by the B_2H_6-to-SiH_4 gas-flow ratio, for both PECVD deposited films and ETPCVD deposited films. For both intrinsic PECVD and ETPCVD samples increasing R^* increases the onset time to crystallization [6]. We find that also in this case R^* influences the crystallisation process of the B-doped a-Si:H films deposited by ETPCVD and PECVD.

Bibliography

[1] C. Nunez. How green are those solar panels, really? *National Geographic*, 2014.

[2] T.D. Lee and A.U. Ebong. A review of thin film solar cell technologies and challenges. *Renewable and Sustainable Energy Reviews*, 70:1286 – 1297, 2017.

[3] S. Gall, J. Schneider, J. Klein, K. Hübener, M. Muske, B. Rau, E. Conrad, I. Sieber, K. Petter, K. Lips, M. Stöger-Pollach, P. Schattschneider, and W. Fuhs. Large-grained polycrystalline silicon on glass for thin-film solar cells. *Thin Solid Films*, 511(Supplement C):7–14, 2006.

[4] W. Beyer. Diffusion and solubility of hydrogen in amorphous and microcrystalline si:h films. *MRS Proceedings*, 664, 2001.

[5] C. Spinella, S. Lombardo, and F. Priolo. Crystal grain nucleation in amorphous silicon. *Journal of Applied Physics*, 84(10):5383–5414, 1998.

[6] K. Sharma, M. A. Verheijen, M. C. M. van de Sanden, and M. Creatore. In situ crystallization kinetics studies of plasma-deposited, hydrogenated amorphous silicon layers. *Journal of Applied Physics*, 111(3):033508, 2012.

[7] BBC-news. First coal-free day in britain since 1880s, 2017. http://www.bbc.co.uk/news/uk-39675418.

[8] C. Podewils. Ein sonntag fast ohne kohlestrom, 2017. https://www.agora-energiewende.de/de/presse/agoranews/news-detail/news/ein-sonntag-fast-ohne-kohlestrom-1/News/detail/.

[9] Eurostat. Complete energy balances - annual data, 2017. http://ec.europa.eu/eurostat/web/products-datasets/-/nrg110a.

[10] A.C. Menezes, A. Cripps, R.A. Buswell, J. Wright, and D. Bouchlaghem. Estimating the energy consumption and power demand of small power equipment in office buildings. *Energy and Buildings*, 75:199 – 209, 2014.

[11] B.P. Jelle. Building integrated photovoltaics: A concise description of the current state of the art and possible research pathways. *Energies*, 9(1):21, 2016.

[12] A.G. Hestnes. Building integration of solar energy systems. *Solar Energy*, 67(4):181–187, 1999.

[13] B. P. Jelle, C. Breivik, and H. D. Røkenes. Building integrated photovoltaic products: A state-of-the-art review and future research opportunities. *Solar Energy Materials and Solar Cells*, 100:69 – 96, 2012.

[14] M. A. Green. The path to 25% silicon solar cell efficiency: History of silicon cell evolution. *Progress in Photovoltaics: Research and Applications*, 17(3):183–189, 2009.

[15] A. Chodos. This month in physics history. *APS NEWS*, 18(4), 2009.

[16] K. Yoshikawa, H. Kawasaki, W. Yoshida, T. Irie, K. Konishi, K. Nakano, T. Uto, D. Adachi, M. Kanematsu, H. Uzu, and K. Yamamoto. Silicon heterojunction solar cell with interdigitated back contacts for a photoconversion eciency over 26%. *Nature Energy*, 2(17032), 2017.

[17] Fraunhofer-Institute. Photovoltaics-report, 2016. https://www.ise.fraunhofer.de/content/dam/ise/de/documents/publications/studies/Photovoltaics-Report.pdf.

[18] NREL. Nrel efficiency chart, 2017. https://www.nrel.gov/pv/assets/ images/efficiency-chart.png.

[19] A.R. Barron and C. Smith. Crystal structure. https://cnx.org/contents/6Q1RYWaw@10/Crystal-Structure.

[20] P.A. Basore. Defining terms for crystalline silicon solar cells. *Progress in Photovoltaics: Research and Applications*, 2(2):177–179, 1994.

[21] M. A. Green and M. J. Keevers. Optical properties of intrinsic silicon at 300 k. *Progress in Photovoltaics: Research and Applications*, 3(3):189–192, 1995.

[22] NREL. Reference air mass 1.5 spectra, 2018.

[23] C. Honsberg and S. Bowden. http://www.pveducaction.org, 2017.

[24] A. B. Sproul and M. A. Green. Improved value for the silicon intrinsic carrier concentration from 275 to 375 k. *Journal of Applied Physics*, 70:846–854, 1991.

[25] G. Andrä, J. Bergmann, F. Falk, E. Ose, and H. Stafast. Laser induced crystallization of amorphous silicon films on glass for thin film solar cells. *physica status solidi (a)*, 166(2):629–634, 1998.

[26] H.-C. Cheng, C.-Y. Huang, F.-S. Wang, K.-H. Lin, and F.-G. Tarntair. Thin-film transistors with polycrystalline silicon films prepared by two-step rapid thermal annealing. *Japanese Journal of Applied Physics*, 39(2, 1A/B):19–21, 2000.

[27] D. L. Young, P. Stradins, Y. Xu, L. Gedvilas, B. Reedy, A. H. Mahan, H. M. Branz, Q. Wang, and D. L. Williamson. Rapid solid-phase crystallization of high-rate, hot-wire chemical-vapor-deposited hydrogenated amorphous silicon. *Applied Physics Letters*, 89(16):161910, 2006.

[28] O. Nast, T. Puzzer, L. M. Koschier, A. B. Sproul, and S. R. Wenham. Aluminum-induced crystallization of amorphous silicon on glass substrates above and below the eutectic temperature. *Applied Physics Letters*, 73(22):3214–3216, 1998.

[29] R. Hull. *Properties of Crystalline Silicon*. EMIS Datareviews Series. INSPEC, The Institution of Electrical Engineers, 1999.

[30] M. Stutzmann. The defect density in amorphous silicon. *Philosophical Magazine Part B*, 60(4):531–546, 1989.

[31] R.E.I. Schropp and M. Zeman. *Amorphous and microcrystalline silicon solar cells: modeling, materials, and device technology*. Springer, 1998.

[32] M. Stutzmann, D. K. Biegelsen, and R. A. Street. Detailed investigation of doping in hydrogenated amorphous silicon and germanium. *Physical Review B*, 35:5666–5701, 4 1987.

[33] R.A. Street. *Hydrogenated Amorphous Silicon*. Cambridge solid state science series. Cambridge University Press, Cambridge, August 1991.

[34] A. H. M. Smets and M. C. M. van de Sanden. Relation of the $Si-H$ stretching frequency to the nanostructural $Si-H$ bulk environment. *Physical Review B*, 76:073202, 8 2007.

[35] P. Roca i Cabarrocas. Plasma enhanced chemical vapor deposition of amorphous, polymorphous and microcrystalline silicon films. *Journal of Non-Crystalline Solids*, 266269, Part 1(0):31–37, 2000.

[36] R. E. I. Schropp, K. F. Feenstra, E. C. Molenbroek, H. Meiling, and J. K. Rath. Device-quality polycrystalline and amorphous silicon films by hot-wire chemical vapour deposition. *Philosophical Magazine Part B*, 76(3):309–321, 1997.

[37] J. Melskens, A. H. M. Smets, S. W. H. Eijt, H. Schut, E. Brück, and M. Zeman. The nanostructural analysis of hydrogenated silicon films based on positron annihilation studies. *Journal of Non-Crystalline Solids*, 2012.

[38] A. H. M. Smets, M. A. Wank, B. Vet, M. Fischer, R. A. C. M. M. van Swaaij, M. Zeman, D. C. Bobela, C. R. Wronski, and M. C. M. van de Sanden. The relation between the bandgap and the anisotropic nature of hydrogenated amorphous silicon. *Photovoltaics, IEEE Journal of*, 2(2):94–98, 2012.

[39] W. M. M. Kessels, R. J. Severens, A. H. M. Smets, B. A. Korevaar, G. J. Adriaenssens, D. C. Schram, and M. C. M. van de Sanden. Hydrogenated amorphous silicon deposited at very high growth rates by an expanding ar-h_2-sih_4 plasma. *Journal of Applied Physics*, 89(4):2404–2413, 2001.

[40] K. Winer, R. A. Street, N. M. Johnson, and J. Walker. Impurity incorporation and doping efficiency in *a* -si:h. *Physical Review B*, 42:3120–3128, 8 1990.

[41] R. A. Street. Model for growth of *a* -si:h and its alloys. *Physical Review B*, 44:10610–10616, 11 1991.

[42] R. A. Street. Hydrogen chemical potential and structure of *a* -si:h. *Physical Review B*, 43:2454–2457, 1 1991.

[43] A. Matsuda and K. Tanaka. Investigation of the growth kinetics of glow-discharge hydrogenated amorphous silicon using a radical separation technique. *Journal of Applied Physics*, 60(7):2351–2356, 1986.

[44] A. Matsuda, K. Nomoto, Y. Takeuchi, A. Suzuki, A. Yuuki, and J. Perrin. Temperature dependence of the sticking and loss probabilities of silyl radicals on hydrogenated amorphous silicon. *Surface Science*, 227(1-2):50 – 56, 1990.

[45] D.A. Porter and K.E. Easterling. *Phase transformations in metals and alloys*. Nelson Thornes LTD, 2 edition, 2001.

[46] G.L. Olson and J.A. Roth. Kinetics of solid phase crystallization in amorphous silicon. *Materials Science Reports*, 3(1):1 – 77, 1988.

[47] M. Volmer and A. Weber. Keimbildung in bersttigten gebilden. *Zeitschrift fuer physikalische Chemie*, 119:227, 1926.

[48] A. H. M. Smets, M. Wank, B. Vet, M. Fischer, R. A. C. M. M. van Swaaij, M. Zeman, D. Bobela, C. R. Wronski, and M. C. M. van de Sanden. The relation between the bandgap and the anisotropic nature of hydrogenated amorphous silicon. *IEEE Journal of Photovoltaics*, 2(2):94–98, 2012.

[49] A. H. M. Smets, W. M. M. Kessels, and M. C. M. van de Sanden. Surface-diffusion-controlled incorporation of nanosized voids during hydrogenated amorphous silicon film growth. *Applied Physics Letters*, 86(4):041909, 2005.

[50] M. Tanaka, M. Taguchi, T. Matsuyama, T. Sawada, S. Tsuda, S. Nakano, H. Hanafusa, and Y. Kuwano. Development of new a-si/c-si heterojunction solar cells: Acj-hit (artificially constructed junction-heterojunction with intrinsic thin-layer). *Japanese Journal of Applied Physics*, 31(11R):3518, 1992.

[51] M. Tanaka M. Isomura S. Tsuda S. Nakano T. Matsuyama, T. Baba and Y. Kuwano. Development of thin-film polycrystalline silicon solar cells by a solid-phase crystallization (spc) method. *Proc.SPIE*, 2017:2017 – 2017 – 12, 1993.

[52] R. Brendel and D. Scholten. Modeling light trapping and electronic transport of waffle-shaped crystalline thin-film si solar cells. *Applied Physics A*, 69:201–213, 08 1999.

[53] P. A. Basore. Large-area deposition for crystalline silicon on glass modules. In *3rd World Conference onPhotovoltaic Energy Conversion, 2003. Proceedings of*, volume 1, pages 935–938 Vol.1, May 2003.

[54] M. A. Green, P. A. Basore, N. Chang, D. Clugston, R. Egan, R. Evans, D. Hogg, S. Jarnason, M. Keevers, P. Lasswell, J. O'Sullivan, U. Schubert, A. Turner, S. R. Wenham, and T. Young. Crystalline silicon on glass (csg) thin-film solar cell modules. *Solar Energy*, 77(6):857 – 863, 2004.

[55] B. Rau, T. Weber, B. Gorka, P. Dogan, F. Fenske, K. Y. Lee, S. Gall, and B. Rech. Development of a rapid thermal annealing process for polycrystalline silicon thin-film solar cells on glass. *Materials Science and Engineering: B*, 159-160:329–332, 2009.

[56] A.G. Aberle. Thin-film solar cells. *Thin Solid Films*, 517(17):4706 – 4710, 2009.

[57] M. J. Keevers, T. L. Young, U. Schubert, and M. A. Green. 10% efficient csg minimodules. In *22nd European Photovoltaic Solar Energy Conference*, volume 3, pages 1783–1790, 2007.

[58] T. Sontheimer, S. Scherf, C. Klimm, C. Becker, and B. Rech. Characterization and control of crystal nucleation in amorphous electron beam evaporated silicon for thin film solar cells. *Journal of Applied Physics*, 110(6):063530, 2011.

[59] S. Gall, M. Muske, I. Sieber, O. Nast, and W. Fuhs. Aluminum-induced crystallization of amorphous silicon. *Journal of Non-Crystalline Solids*, 299-302:741–745, 2002. 19th International Conference on Amorphous and Microcrystalline Semiconductors.

[60] M. Tanaka. Recent progress in crystalline silicon solar cells. *IEICE Electronics Express*, 10(16):20132006–20132006, 2013.

[61] K. Yoshikawa, H. Kawasaki, W. Yoshida, T. Irie, K. Konishi, K. Nakano, T. Uto, D. Adachi, M. Kanematsu, H. Uzu, and K. Yamamoto. Silicon heterojunction solar cell with interdigitated back contacts for a photoconversion efficiency over 26%. *Nature Energy*, 2:17032, March 2017.

[62] D. van Gestel, I. Gordon, and J. Poortmans. Aluminum-induced crystallization for thin-film polycrystalline silicon solar cells: Achievements and perspective. *Solar Energy Materials and Solar Cells*, 119:261–270, 2013.

[63] J. Dore, D. Ong, S. Varlamov, R. Egan, and M. A. Green. Progress in laser-crystallized thin-film polycrystalline silicon solar cells: Intermediate layers, light trapping, and metallization. *IEEE Journal of Photovoltaics*, 4(1):33–39, Jan 2014.

[64] J. Haschke, D. Amkreutz, and B. Rech. Liquid phase crystallized silicon on glass: Technology, material quality and back contacted heterojunction solar cells. *Japanese Journal of Applied Physics*, 55(4S):04EA04, 2016.

[65] C. T. Trinh, R. Schlatmann, B. Rech, and D. Amkreutz. Progress in and potential of liquid phase crystallized silicon solar cells. *Solar Energy*, 2018.

[66] C.T. Trinh, N. Preissler, P. Sonntag, M. Muske, K. Jäger, M. Trahms, R. Schlatmann, B. Rech, and D. Amkreutz. Potential of interdigitated back-contact silicon heterojunction solar cells for liquid phase crystallized silicon on glass with efficiency above 14 *Solar Energy Materials and Solar Cells*, 174:187 – 195, 2018.

[67] M. A. Green, Y. Hishikawa, W. Warta, E. D. Dunlop, D. H. Levi, J. Hohl-Ebinger, and A. W. H. Ho-Baillie. Solar cell efficiency tables (version 50). *Progress in Photovoltaics: Research and Applications*, 25(7):668–676.

[68] A. Matsuda, M. Takai, T. Nishimoto, and M. Kondo. Control of plasma chemistry for preparing highly stabilized amorphous silicon at high growth rate. *Solar Energy Materials and Solar Cells*, 78:3–26, 07 2003.

[69] A. M. H. N. Petit, R. A. C. M. M. van Swaaij, and M. C. M. van de Sanden. Hydrogen injection in etp plasma jet for fast-deposition of high-quality a-si:h. In *2004 MRS Spring Meeting*, volume 808, pages 359–364, San Fransisco, CA; USA, 2004.

[70] J. W. A. M. Gielen, W. M. M. Kessels, M. C. M. van de Sanden, and D. C. Schram. Effect of substrate conditions on the plasma beam deposition of amorphous hydrogenated carbon. *Journal of applied physics*, 82(5):2643–2654, 1997.

[71] F. J. H. van Assche, W. M. M. Kessels, R. Vangheluwe, W. S. Mischke, M. Evers, and M. C. M. van de Sanden. High rate (3 nm/s) deposition of dense silicon nitride films at low substrate temperatures (¡ 150 c) using the expanding thermal plasma and substrate biasing. *Thin Solid Films*, 484(1):46–53, 2005.

[72] B. A. Korevaar, C. Smit, A. M. H. N. Petit, R. A. C. M. M. van Swaaij, and M. C. M. van de Sanden. Integration of expanding

thermal plasma deposited hydrogenated amorphous silicon in solar cells. In *MRS Proceedings*, volume 715, pages A6–5. Cambridge Univ Press, 2002.

[73] A. H. M. Smets, W. M. M. Kessels, and M. C. M. van de Sanden. Vacancies and voids in hydrogenated amorphous silicon. *Applied Physics Letters*, 82(10):1547–1549, 2003.

[74] A. A. Langford, M. L. Fleet, B. P. Nelson, W. A. Lanford, and N. Maley. Infrared absorption strength and hydrogen content of hydrogenated amorphous silicon. *Physical Review B*, 45:13367–13377, 6 1992.

[75] G. Lucovsky, R. J. Nemanich, and J. C. Knights. Structural interpretation of the vibrational spectra of *a*-si: H alloys. *Phys. Rev. B*, 19:2064–2073, 2 1979.

[76] W. M. M. Kessels, M. C. M. Sanden, van de, R. J. Severens, L. J. IJzendoorn, van, and D. C. Schram. Hydrogen in a-si:h deposited by an expanding thermal plasma : a temperature, growth rate and isotope study. In R. Schropp, editor, *Amorphous and microcrystalline silicon technology - 1998 : symposium held April 14 - 17, 1998, San Francisco, California, U.S.A.*, Materials Research Society Symposium Proceedings, pages 529–534, 1998.

[77] C.V. Raman and K.S. Krishnan. A new type of secondary radiation. *Nature*, 121:501–502, March 1928.

[78] S. C. Shen and M. Cardona. Infrared and far-infrared absorption of b- and p-doped amorphous si. *Physical Review B*, 23(10):5322, 1981.

[79] P. Danesh, B. Pantchev, K. Antonova, E. Liarokapis, B. Schmidt, D. Grambole, and J. Baran. Hydrogen bonding and structural order in hydrogenated amorphous silicon prepared with hydrogen-diluted silane. *Journal of Physics D: Applied Physics*, 37(2):249, 2004.

[80] D. Beeman, R. Tsu, and M. F. Thorpe. Structural information from the raman spectrum of amorphous silicon. *Phys. Rev. B*, 32:874–878, 7 1985.

[81] S. Gupta, R. S. Katiyar, G. Morell, S. Z. Weisz, and I. Balberg. The effect of hydrogen on the network disorder in hydrogenated amorphous silicon. *Applied Physics Letters*, 75(18):2803–2805, 1999.

[82] M. Cardona. Vibrational spectra of hydrogen in silicon and germanium. *physica status solidi (b)*, 118(2):463–481, 1983.

[83] N.B. Colthup, L.H. Daly, and S.E. Wiberley. *Introduction to infrared and Raman spectroscopy*. Academic Press, 1990.

[84] W. H. Bragg and W. L. Bragg. The reflection of x-rays by crystals. *Proceedings of the Royal Society of London A: Mathematical, Physical and Engineering Sciences*, 88(605):428–438, 1913.

[85] WikiCommons. Bragg plane diffraction, 2009.

[86] W.H. Miller. *A Treatise on Crystallography*. For J. & J. J. Deighton, 1839.

[87] COD. Crystallography open database. data retrieved using DIFFRAC.EVA software, 2010.

[88] M. Avrami. Granulation, phase change, and microstructure kinetics of phase change. iii. *The Journal of Chemical Physics*, 9(2):177–184, 1941.

[89] M. Avrami. Kinetics of phase change. ii transformation-time relations for random distribution of nuclei. *The Journal of Chemical Physics*, 8(2):212–224, 1940.

[90] M. Avrami. Kinetics of phase change. i general theory. *The Journal of Chemical Physics*, 7(12):1103–1112, 1939.

[91] W.A. Johnson and R.F. Mehl. Reaction kinetics in process of nucleation and growth. *Transactions of the American Institure of Mining, Metallurgical and Petroleum Engineers*, 135:416, 1939.

[92] D. Turnbull and J.C. Fischer. Rate of nucleation in condensed systems. *Journal of Chemical Physics*, 17:71–73, 1949.

[93] F. Law, B. Hoex, J. Wang, J. Luther, K. Sharma, M. Creatore, and M. C. M. van de Sanden. Kinetic study of solid phase crystallisation of expanding thermal plasma deposited a-si:h. *Thin Solid Films*, 520(17):5820 – 5825, 2012.

[94] J. I. Langford. A rapid method for analysing the breadths of diffraction and spectral lines using the voigt function. *Journal of Applied Crystallography*, 11(1):10–14, 2 1978.

[95] W. Theiss. Scout - optical model.

[96] R. H. Klazes, M. H. L. M. van den Broek, J. Bezemer, and S. Radelaar. Determination of the optical bandgap of amorphous silicon. *Philosophical Magazine Part B*, 45(4):377–383, 1982.

[97] M. Fischer, H. Tan, J. Melskens, R. Vasudevan, M. Zeman, and A. H. M. Smets. High pressure processing of hydrogenated amorphous silicon solar cells: Relation between nanostructure and high open-circuit voltage. *Applied Physics Letters*, 106(4), 2015.

[98] J. Melskens, A. H. M. Smets, M. Schouten, S. W. H. Eijt, H. Schut, and M. Zeman. New insights in the nanostructure and defect states of hydrogenated amorphous silicon obtained by annealing. In *Photovoltaic Specialists Conference (PVSC), Volume 2, 2012 IEEE 38th*, pages 1–8. IEEE, 2012.

[99] W. Beyer and H. Wagner. Determination of the hydrogen diffusion coefficient in hydrogenated amorphous silicon from hydrogen effusion experiments. *Journal of Applied Physics*, 53(12):8745–8750, 1982.

[100] M. H. Brodsky, Manuel Cardona, and J. J. Cuomo. Infrared and raman spectra of the silicon-hydrogen bonds in amorphous silicon prepared by glow discharge and sputtering. *Physical Review B*, 16:3556–3571, 8 1977.

[101] R. J. Severens, G. J. H. Brussaard, M. C. M. van de Sanden, and D. C. Schram. Characterization of plasma beam deposited amorphous hydrogenated silicon. *Applied Physics Letters*, 67(4):491–493, 1995.

[102] A. H. Mahan, P. Menna, and R. Tsu. Influence of microstructure on the urbach edge of amorphous sic:h and amorphous sige:h alloys. *Applied Physics Letters*, 51(15):1167–1169, 1987.

[103] V. A. Volodin and D. I. Koshelev. Quantitative analysis of hydrogen in amorphous silicon using raman scattering spectroscopy. *Journal of Raman Spectroscopy*, 44(12):1760–1764, 2013.

[104] D. Bermejo and M. Cardona. Raman scattering in pure and hydrogenated amorphous germanium and silicon. *Journal of Non-Crystalline Solids*, 32(1):405 – 419, 1979.

[105] M. Ledinsky, A. Vetushka, J. Stuchlík, T. Mates, A. Fejfar, J. Kočka, and J. Štěpánek. Crystallinity of the mixed phase silicon thin films by raman spectroscopy. *Journal of Non-Crystalline Solids*, 354(19-25):2253 – 2257, 2008.

[106] N. Beck, J. Meier, J. Fric, Z. Remeš, A. Poruba, R. Flckiger, J. Pohl, A. Shah, and M. Vaněček. Enhanced optical absorption in microcrystalline silicon. *Journal of Non-Crystalline Solids*, 198200, Part 2(0):903–906, 1996.

[107] R. C. Chittick, J. H. Alexander, and H. F. Sterling. The preparation and properties of amorphous silicon. *Journal of The Electrochemical Society*, 116(1):77–81, 1969.

[108] G. Müller, S. Kalbitzer, and H. Mannsperger. A chemical-bond approach to doping, compensation and photo-induced degradation in amorphous silicon. *Applied Physics A: Materials Science & Processing*, 39(4):243–250, 1986.

[109] R. A. Street. Doping and the fermi energy in amorphous silicon. *Physical Review Letters*, 49(16):1187–1190, 1982. PRL.

[110] J. Robertson. Doping and gap states in amorphous silicon. *Journal of Physics C: Solid State Physics*, 17(13):L349, 1984.

[111] H. Nasu, M. Watanabe, K. Shizuma, S. Makida, M. Ueda, T. Imura, Y. Osaka, and H. Hasai. Structure changes by annealing and doping of a-si:h prepared at high deposition rate studied by means of positron annihilation. *Journal of Non-Crystalline Solids*, 95-96, Part 1(0):563–570, 1987.

[112] R. Downing, J. Maki, and R. Fleming. Analytical applications of neutron depth profiling. *Journal of Radioanalytical and Nuclear Chemistry*, 112(1):33–46, 1987.

[113] R. G. Downing and G. P. Lamaze. Near-surface profiling of semiconductor-materials using neutron depth profiling. *Semiconductor Science and Technology*, 10(11):1423–1431, 1995.

[114] L.H. Long. The mechanisms of thermal decomposition of diborane and of interconversion of the boranes. *Journal of Inorganic and Nuclear Chemistry*, 32(4):1097–1115, 1970.

[115] D. Song, D. Inns, A. Straub, M.L. Terry, P. Campbell, and A.G. Aberle. Solid phase crystallized polycrystalline thin-films on glass from evaporated silicon for photovoltaic applications. *Thin Solid Films*, 513(12):356 – 363, 2006.

[116] R.B. Bergmann, G. Oswald, M. Albrecht, and V. Gross. Solid-phase crystallized si films on glass substrates for thin film solar cells. *Solar Energy Materials and Solar Cells*, 46(2):147–155, 1997.

[117] S. Gall, C. Becker, E. Conrad, P. Dogan, F. Fenske, B. Gorka, K. Y. Lee, B. Rau, F. Ruske, and B. Rech. Polycrystalline silicon thin-film solar cells on glass. *Solar Energy Materials and Solar Cells*, 93(67):1004–1008, 2009.

[118] J. M. Westra, V. Vavruňková, P. Šutta, R. A. C. M. M. van Swaaij, and M. Zeman. Formation of thin-film crystalline silicon on glass observed by in-situ xrd. *Energy Procedia*, 2(1):235 – 241, 2010.

[119] M. Wank, R. A. C. M. M. van Swaaij, and M. C. M. van de Sanden. Manipulating the hydrogen-bonding configuration in etp-cvd a-si: H. *MRS Online Proceeding Library Archive*, 989:523–528, 2007.

[120] R. Brendel and A. Goetzberger. *Thin-Film Crystalline Silicon Solar Cells: Physics and Technology*. Wiley, 2003.

[121] J. Dore, R. Evans, U. Schubert, B. D. Eggleston, D. Ong, K. Kim, J. Huang, O. Kunz, M. Keevers, R. Egan, S. Varlamov, and M. A. Green. Thin-film polycrystalline silicon solar cells formed by diode laser crystallisation. *Progress in Photovoltaics: Research and Applications*, 21(6):1377–1383, 2013.

[122] A. A. D. T. Adikaari and S. R. P. Silva. Thickness dependence of properties of excimer laser crystallized nano-polycrystalline silicon. *Journal of Applied Physics*, 97:114305–114307, 2005.

[123] P. Stradins, D. L. Young, Y. Yan, E. Iwaniczko, Y. Xu, R. C. Reedy, H. M. Branz, and Q. Wang. Real-time optical spectroscopy study of solid-phase crystallization in hydrogenated amorphous silicon. *Applied Physics Letters*, 89(12):121921–121921–3, 9 2006.

[124] S. Gall, K.Y. Lee, P. Dogan, B. Gorka, C. Becker, F. Fenske, B. Rau, E. Conrad, and B. Rech. Large-grained polycrystalline silicon thin-film solar cells on glass. In *Proc. 22nd European Photovoltaic Solar Energy Conference, Milan, Italy*, 2007.

[125] S. Gall and B. Rech. Technological status of polycrystalline silicon thin-film solar cells on glass. *Solar Energy Materials and Solar Cells*, 119(0):306 – 308, 2013.

[126] K. Sharma, M. V. Ponomarev, M. A. Verheijen, O. Kunz, F. D. Tichelaar, M. C. M. van de Sanden, and M. Creatore. Solid-phase crystallization of ultra high growth rate amorphous silicon films. *Journal of Applied Physics*, 111(10):103510, 2012.

[127] L. Csepregi, E. F. Kennedy, T. J. Gallagher, J. W. Mayer, and T. W. Sigmon. Reordering of amorphous layers of si implanted with 31p, 75as, and 11b ions. *Journal of Applied Physics*, 48(10):4234–4240, 1977.

[128] I. Suni, G. Gltz, M.-A. Nicolet, and S.S. Lau. Effects of electrically active impurities on the epitaxial regrowth rate of amorphized silicon and germanium. *Thin Solid Films*, 93(12):171 – 178, 1982.

[129] I. Suni, G. Gltz, M. G. Grimaldi, M-A. Nicolet, and S. S. Lau. Compensating impurity effect on epitaxial regrowth rate of amorphized si. *Applied Physics Letters*, 40(3):269–271, 1982.

[130] M. Fischer, R. Santbergen, A. H. M. Smets, and M. Zeman. Raman spectroscopy on thin film silicon on non-transparent substrates and in solar cell devices. In *Photovoltaic Specialists Conference (PVSC), 2011 37th IEEE*, 2011.

[131] J. I. Langford and A. J. C. Wilson. Scherrer after sixty years: A survey and some new results in the determination of crystallite size. *Journal of Applied Crystallography*, 11(2):102–113, Apr 1978.

Acknowledgements

A PhD thesis is considered a personal achievement by many, but I have learned that it cannot be done without the help and support of many incredible people. First of all I would like to thank prof. Miro Zeman for giving me the opportunity to work in his group and being my promotor. Many thanks to the committee members: Prof.dr. R. Schlatmann, Prof.dr.ir. S. van der Zwaag, Prof.dr. R. Ross, Dr. S. W. H. Eijt and especially Dr. Amarante J. Böttger.

My sincerest gratitude goes to my daily supervisor and co-promotor, René van Swaaij, for not giving up on me and showing me how to do research, and especially how to write it down.

This dissertation would not be possible without the help and cooperation of (i) TU Delft groups: DIMES, Materials Science and Engineering, Laboratory of Inorganic Chemistry and of course the PVMD group, (ii) TU Eindhoven Plasma and Materials Processing group, (iii) New Technologies Research Centre (University of West Bohemia) in Plzen, and (iv) Helmholtz Institute Berlin. Thank you for your efforts in material analysis and uncovering the crystallisation process of those pesky Si and H atoms: Kashish Sharma, Adriana Creatore, Pavol Šutta, Lucie Prušáková, Tobias Sontheimer, Stefan Gall, Albert Goossens, Frans Tichelaar, Kees Kwakenaak, Vera Popovich, Brano Grančič.

The research would not be possible without the wonderful support of the technical staff, department secretaries, HR staff and coaches: Laura Buns, Iris de Jel, Suzy Sirks-Bong, Marysia Lagendijk-Korzeniewski, Marian Roozenburg-de Bree, Jamilla Eddini, Sharmilla Rattansingh, Claudia de Kooter, Ilona van der Wenden, Martijn Tijssen, Stefaan Heirman, Kasper Zwetsloot, Jan Chris Staalenburg, Stefan Luxembourg (apparatuur uitleg), Koos Huijsen (voor het helpen latexen). Zonder jullie was het nooit gelukt!

I would like to thank all the PVMD group members (technical staff, students, PhD's, postdocs, and professors) and a lot of DIMES people for making my office and evening hours lively and fun and for being a great help with the research. My thanks in particular for all the cakes, beers, office craziness and more to: Agata, Cassan (for keys left at home), Sergiy, Serge, Janez, Dong, Hairen, Lihao, Rudi, Marinus, Karol, Ravi, Andrea, Olindo, Bas, Michael, Pavel, Gijs, Solomon, Tristan, Jimmy, Klaus, Dimitris, Marilena, Pieter and Natalie.

Of course I have forgotten to thank many people, my apologies, please know that I am grateful for all the help I have received. Thank you all.

Aan het eind van mijn onderzoek ben ik voltijd in dienst gegaan bij de Hogeschool van Arnhem en Nijmegen. Werken en 'nog even een paar zaken af maken' bleek moeilijker dan ik had gedacht. Gelukkig heeft de HAN mij de ruimte gegeven om de laatste stappen toch te zetten. Zonder de support van het lectoraat Duurzame Energie, kamergenoten Jan en Eigbert, SEECE en het lectoraat Meet- en Regeltechniek was het niet gelukt. Dank voor de tijd en vooral de aanmoedigingen.

Er is een gezegde: *als de voorspoed faalt falen de vrienden*, mensen die dit verzonnen waren geen vrienden van jullie. Ik ben ontzettend dankbaar voor alle steun, inzicht, perspectief en liefde: Jildou, Heleen en Dirk, Yvonne en Floris, Arienne, Eva en Willemijn jullie zijn geweldige vrienden.

Lieve familie, dankzij jullie heb ik heel mijn leven liefde gekend, warmte, eerlijkheid en steun. Harmen en Carla, jullie hebben mij aangemoedigd, mijn keuzes gesteund, mij uitgedaagd mezelf te ontwikkelen en plezier te hebben in het leven. Mieke, vooral met het laatste heb jij me ontzettend geholpen, jouw vrolijkheid is besmettelijk, jouw zorg verkwikkend. Lukas, slim, warm en eerlijk, ik kan me geen betere broer wensen. Zonder jouw goede raad was dit boekje er niet geweest! Dankjewel!

Lieve Mischa, ik heb langer met dit proefschrift geleefd dan met jou. De weg naar dit moment was interessant, hobbelig, prachtig en wispelturig. Ik ben blij dat ik het laatste stuk van dit proces met jou mag delen. Dank voor jouw steun, aanmoediging, correcties en geduld. Ik hoop dat wij nog heel lang samen op weg mogen zijn, avonturen mogen beleven en mogen genieten. Jij bent geweldig. Ik hou van jou!

In de vorige versie van dit dankwoord heette jij nog kleintje, maar je bent al 10 maanden! Lieve Chris, met grote interesse keek jij de afgelopen maanden naar mijn scherm en trommelde vrolijk mee op het toetsenbord. Jij hebt mijn hart voor altijd gestolen ♡.

About the author

Joke Westra was born in Hoorn, The Netherlands on April 11, 1983. In 2001 she finished her pre-university education (VWO) at Werenfridus, Scholengemeenschap Tabor in Hoorn. She earned her BSc degree in Industrial Design Engineering at the Delft University of Technology, Delft, the Netherlands in 2005. After this Joke proceeded with her MSc degree in Materials Science and Engineering at the Delft University of Technology. She earned her MSc degree in 2008 in Materials Science and Engineering: Metals Science and Technology. The MSc thesis concerned the interconnection technology for polycrystalline silicon PV. It was conducted in a joint cooperation between Energieonderzoek Centrum Nederland (ECN) in Petten, the Netherlands and the Joining and Mechanical Behaviour group of the Faculty of Mechanical, Maritime and Materials Engineering at Delft University of Technology. In 2008 she started her PhD under the supervision of prof. dr. M. Zeman and dr. R.A.C.M.M. van Swaaij in the Photovoltaic Materials and Devices group. The results of the PhD research are described in the thesis before you. Since 2013 she is employed as lecturer and (senior) researcher at HAN University of Applied Sciences in Arnhem, the Netherlands.

Publications

- J.M. Westra, R.A.C.M.M. van Swaaij, P. Šutta, K. Sharma, M. Creatore, M. Zeman, *Study of the effect of boron doping on the solid phase crystallisation of hydrogenated amorphous silicon films*, Thin Solid Films, vol 568, p. 38, (2014)

- V. Popovich, J.M. Westra, R.A.C.M.M. van Swaaij, M. Janssen, I.J. Bennett, I.M. Richardson, *Raman spectroscopy characterization of residual stress in multicrystalline silicon solar wafers and solar cells: relation to microstructure, defects and processing conditions*, In s.n. (Ed.), Proceedings 37th IEEE Photovoltaic Specialists Conference (pp. 1668 1673) (2011)

- J.M. Westra, V. Vavruňková, P. Šutta, R.A.C.M.M. van Swaaij, M. Zeman, *Formation of thin-film crystalline silicon on glass observed by in-situ XRD*, Energy Procedia, vol. 2, i. 1, p235 (2010)

- J.M. Westra, P. Šutta, T. Sontheimer, V. Vavruňková, S. Gall, R.A.C.M.M. van Swaaij and M. Zeman, *Crystallization process of amorphous silicon films on glass monitored by in-situ XRD*, In s.n. (Ed.), Proceedings 24th European photovoltaic solar energy conference and exhibition (pp. 2490-2493). Hamburg: WIP-Renewable Energies (2009)

- B. Grančič, J.M. Westra, M. Zeman, *Effect of c-Si base layer thickness on efficiency limits of thin - film c-Si solar cells on glass*, In s.n. (Ed.), Proceedings 24th European photovoltaic solar energy conference and exhibition (pp. 2596-2600). Hamburg: WIP-Renewable Energies (2009)

- J.M. Westra, P. Šutta, R.A.C.M.M. van Swaaij and M. Zeman, *Influence of the hydrogen content and layer thickness on crystallization of a-Si:H thin films on glass*, In s.n. (Ed.), Proceedings SAFE ProRISC (pp. 129-132). Utrecht: Technology Foundation (2009)

- J.M. Westra and M. Zeman, Thin-film crystalline silicon on glass, In s.n. (Ed.), The annual workshop on semiconductor advances for future electronics and sensors (pp. 522-525). Veldhoven, the Netherlands: STW (2008)